Title
Development of Antibody Tools to Interrogate and Modulate Cellular Signaling in Cancer

Author
Martinko, Alexander

Publication Date
2018

Peer reviewed|Thesis/dissertation

Development of Antibody Tools to Interrogate and Modulate

Cellular Signaling in Cancer

by

Alexander John Martinko

DISSERTATION

Submitted in partial satisfaction of the requirements for the degree of

DOCTOR OF PHILOSOPHY

in

Chemistry and Chemical Biology

in the

GRADUATE DIVISION

of the

UNIVERSITY OF CALIFORNIA, SAN FRANCISCO

Acknowledgments

Firstly, I would like to acknowledge my thesis advisor Jim Wells for providing the resources, guidance, and support that enabled and motivated me to develop as a scientist in his lab. Jim leads his lab by example, bringing a mentality of enthusiastic curiosity with him every day. This attitude is infectious, and it challenged and inspired me to approach my research with passion and creativity. While completing a PhD is filled with many late nights and unexpected challenges, the approach to research I learned from Jim made it so that I sincerely looked forward to every day in the lab. I am also grateful to Jim for the amazing work culture that he created during my time in his lab, including the amazing ski trips and holiday parties. I will forever remember my experience working for Jim with fondness and I will do my best to carry forward the lessons he taught me as I continue forward in my career.

I am incredibly thankful to the members of the Wells lab that I have had the honor of overlapping with over the past six years. I learned so much from this group of scientists and have made friendships I am sure will last a lifetime. I would especially like to acknowledge Juan Diaz, Zach Hill, Olivier Julien, Brian Lee, Kevin Leung, Tet Matsuguchi, Kurt Mou, Duy Nguyen, Sam Pollock, Justin Rettenmaier, Hai Tran, and Amy Weeks for going above and beyond to offer invaluable mentorship that helped guide me through my PhD. I also want to thank my thesis committee, Charles Craik and Sourav Bandyopadhyay for valuable advice about both research and career development.

I also want to acknowledge my parents Pam and John for supporting me through this journey. They encouraged me from a young age to be curious and to value education. They continue to inspire me through example by living lives filled with a balance of fun and accomplishment. I am grateful for the many calls home during graduate school where they eagerly asked about the progress of my research, and provided support that helped me to stay motivated and passionate.

Lastly, I want to thank my loving Fiancé Victoria. I am tremendously grateful for her unconditional support during my graduate career. On the days where big experiments crashed and burned, I often doubted myself and my ability to keep persevering through failures. Victoria never doubted me, and her undying encouragement during these tough times gave me the strength I needed to keep going. I am so thankful to have had such an amazing cheerleader and best friend in my life while completing my degree. I am excited to enter the next stage of our lives together, and I am determined to reciprocate all of the love and support that Victoria offers me.

Contributions

Chapters 1 and 2 of this thesis are reprints of the material as it appears in:

Martinko A.J., Truillet C., Julien O., Diaz J.E., Horlbeck, M.A., Whiteley G., Blonder J., Weissman J.S., Bandyopadhyay S., Evans M.J., Wells J.A. (2018) "Targeting RAS Driven Human Cancer Cells with Antibodies to Upregulated and Essential Cell-Surface Proteins." **eLife.** 2018;7:e31098

*Hill Z.B., *Martinko A.J., Nguyen D.P., Wells J.A. (2018) "Human Antibody-Based Chemically Induced Dimerizers for Cell Therapeutic Applications." **Nat. Chem. Biol.** 14:112-117

*Denotes equal contribution

Abstract

Over the last two decades, a major focus in the biomedical research community has been placed on understanding the interaction between the human immune system and cancer. This focus has led to a considerably improved understanding of how cancer can evade immune detection, and as a consequence, the emergence of a novel class of cancer therapeutics that can trigger the immune system to recognize and eliminate previously undetected cancers. These new therapies, known as cancer immunotherapies, have resulted in unprecedented and remarkably durable outcomes in the clinic. However, there are key limitations that continue to hinder how broadly immunotherapies can be applied to treat human cancers. The research in this thesis describes efforts to apply antibody engineering as a tool to address some of these limitations.

Antibodies that recognize tumor specific antigens can serve as guides to target the immune system directly to cancer cells. However, for many cancer types, there are currently no known tumor specific antigens. This paucity of available targets continues to present a major challenge in the immunotherapy field. Chapter 1 describes the development of a technological pipeline that coupled proteomics to antibody discovery in order to discover and begin to validate novel tumor specific antigens on the cell surface proteome of Ras driven cancers. Ras driven cancers represent nearly a third of all human malignancies. The work in this chapter presents a new series of molecular targets that

could potentially be leveraged to target the immune system to this large class of difficult to target cancers.

Another major challenge in the immunotherapy space is that the treatments often work too well. The result is rapid hyperactivation of the immune system, often leading to horrible side effects faced by patients including severe fevers, neurotoxicity, and sometimes death. A prevailing thought in the community is that a more gradual activation of this immune response might ameliorate side effects while maintaining efficacy. Chapter 2 describes the development of a new class of molecular switches called Antibody-based Chemically Inducible Dimerizers that enable immune cell activation to be precisely regulated by administration of small molecule drugs.

Table of Contents

List of Figures

Page

Chapter 1

Targeting RAS Driven Human Cancer Cells with Antibodies to Upregulated and Essential Cell-Surface Proteins

Alexander J Martinko, Charles Truillet, Olivier Julien, Juan Diaz, Max Horlbeck, Gordon Whiteley, Josip Blonder, Jonathan Weissman, Sourav Bandyopadhyay, Michael Evans, James A Wells

Abstract:

While there have been tremendous efforts to target oncogenic RAS signaling from inside the cell, little effort has focused on the cell-surface. Here, we used quantitative surface proteomics to reveal a signature of proteins that are upregulated on cells transformed with $KRAS^{G12V}$, and driven by MAPK pathway signaling. We next generated a toolkit of recombinant antibodies to seven of these RAS-induced proteins. We found that five of these proteins are broadly distributed on cancer cell lines harboring RAS mutations. In parallel, a cell-surface CRISPRi screen identified integrin and Wnt signaling proteins as critical to RAS-transformed cells. We show that antibodies targeting CDCP1, a protein common to our proteomics and CRISPRi datasets, can be leveraged to deliver cytotoxic and immunotherapeutic payloads to RAS-transformed cancer cells and report for RAS signaling status in vivo. Taken together, this work presents a technological platform for attacking RAS from outside the cell.

Introduction:

RAS is a family of three ubiquitously expressed small GTPases found in all animal cell types. RAS is localized to the intracellular leaflet of the cell membrane where it serves as a major communication hub that relays extracellular growth factor-dependent signaling to as many as a dozen different intracellular signaling pathways, including the classically studied MAPK and PI3K pathways [1]. Collectively, these pathways induce dramatic changes to cells including transcriptional reprogramming, promotion of cell survival, suppression of apoptosis, metabolic rewiring, promotion of proliferation, and increased cell invasiveness [2]. Many of these phenotypes are well-known hallmarks of cancer survival [3]. Thus, it is not surprising that nearly one third of all human malignancies have been found to be driven by mutational activation of one of the three RAS isoforms: KRAS, NRAS and HRAS [4]. Hence oncogenic RAS has been an important focus of the cancer biology and drug discovery communities for several decades [5,6]. In efforts to identify tractable drug targets in RAS driven cancers, tremendous research emphasis has been placed on understanding oncogenic RAS and its role in the dysregulation of intracellular signaling pathways [7]. Despite these intense efforts to target intracellular pathways, little is understood about how RAS signaling can regulate the cell surface proteome, the surfaceome.

The surfaceome represents the dominant means by which cells communicate, interact, obtain nutrients, and engage the immune system. Overexpression of oncogenic RAS in model cell lines contributes to loss of adhesion, increased invasive properties, and evasion of immune responses, phenotypes that depend on the function of membrane

proteins [2]. This suggests that RAS driven transcriptional reprogramming coordinately regulates the expression of cell surface proteins in order to exert malignant phenotypes. We believe systematic efforts are needed to identify the influence of oncogenic on surface protein expression. Such studies would aid in progressing our fundamental understanding of how RAS drives malignancy. Additionally, they may lead to the identification of novel targets for next generation antibody and cellular therapy based intervention in RAS driven cancers.

Here, we applied quantitative mass spectrometry (MS)-based proteomics on an isogenic diploid epithelial cell model, MCF10A [8], to measure the influence of oncogenic KRAS signaling on the expression of proteins in the surfaceome. We find that KRAS dramatically alters the expression of membrane proteins and coordinately regulates groups of proteins critical for managing cell adhesion and migration. Using pharmacological inhibitors to interrogate the contribution of individual effector pathways, we find that the oncogenic KRAS-induced changes in the surfaceome are driven predominantly through the MAPK effector pathway. From these discovery efforts, we derived a panel of recombinant antibodies to half a dozen of these differentially expressed targets, and applied the antibodies to confirm their surface expression patterns in a panel of mutant KRAS driven cancer cell lines.

To further focus our efforts on those upregulated surface targets that are most critical for KRAS driven cell growth, we conducted a CRISPRi screen to assess the relative functional importance of more than 1600 proteins in the oncogenic KRAS surfaceome as

compared to control cells. We discovered KRAS transformed cells have a selective dependence on the surfaceome to maintain both Integrin and Wnt signaling, pathways critical for regulation of adhesion and cell migration, respectively. One of these targets, CUB Domain Containing Protein 1 (CDCP1), a protein known to drive loss of adhesion through integrin signaling, was a common hit in both our MS and CRISPRi screens [9,10]. We focused on this example and showed that recombinant antibodies to CDCP1 can be used to selectively deliver therapeutic cytotoxic payloads or recruit and activate T-cells to pancreatic cancer cells while sparing normal control cells. We further show in mouse xenograft models for pancreatic cancer that CDCP1 expression level is an abundant biomarker for RAS signaling through the MAPK signaling pathway. Our studies provide a mechanism for how oncogenic KRAS can influence the expression and function of membrane proteins and how this knowledge can be leveraged to identify potential targets to attack RAS from outside the cell.

Results:

Characterization of the oncogenic KRAS surfaceome

The three major cancer types in which RAS mutations are the most prevalent (pancreatic, lung, and colorectal) all arise from epithelial tissue [5]. To begin to isolate the effects of KRAS transformation on the cell surfaceome, we chose a well-characterized, non-tumorigenic immortalized epithelial cell line, MCF10A, to generate an isogenic model for KRAS transformation [11,12]. The diploid MCF10A cell line is often used for oncogenic transformation studies because it is non-maligant and harbors only small genetic modifications typical of a culture adapted cell line. In addition, MCF10As are readily

transduced with lentivirus, which enabled the rapid generation of the isogenic model as well as the possibility to engineer these cells further for downstream validation studies. Importantly, MCF10A cells stably transduced with oncogenic $KRAS^{G12V}$ they undergo numerous phenotypic changes characteristic of malignant transformation, including increased proliferation and significant loss of cell adhesion [13]. While MCF10A cells are mammary in origin, and RAS is rarely implicated in breast cancer, we believe that the benefits of this model outweighs this caveat. Moreover, we hypothesized RAS signaling in any epithelial cell type would result in a common transcriptional program and signature of cell-surface protein expression. Recently, we showed using initial proteomics discovery experiments that the surfaceome does indeed change substantially in MCF10A cells expressing oncogenic KRAS [14]. However, to determine the therapeutic potential of exploiting differences in the surfaceome in RAS-driven cancers, we needed to quantitatively measure the extent to which these proteins change.

To measure changes in the cell surface proteome in an unbiased manner we applied the recently established glycoprotein capture and enrichment proteomic method. This is advantageous because greater than 90% of surface proteins contain Asn-linked glycosylation [15,16]. We adapted the method to quantitatively compare the surface protein levels on the two isogenic cell lines, MCF10A cells with or without oncogenic $KRAS^{G12V}$, using Stable Isotope Labeling with Amino Acids in Cell Culture (SILAC) (**Figure 1-1A**) [17]. Isotopically labeled cells were harvested and treated with sodium periodate to oxidize the vicinal diols on the cell surface glycans. Subsequently, cells were treated with biocytin-hydrizide to label the oxidized glycans with biotin for pull-down and enrichment. The

proteins were captured on streptavidin beads, trypsinized, washed, and N-glycosylated peptides were released from the beads by N-glycanase (PNGase) treatment. Released peptides were then analyzed by LC-MS/MS.

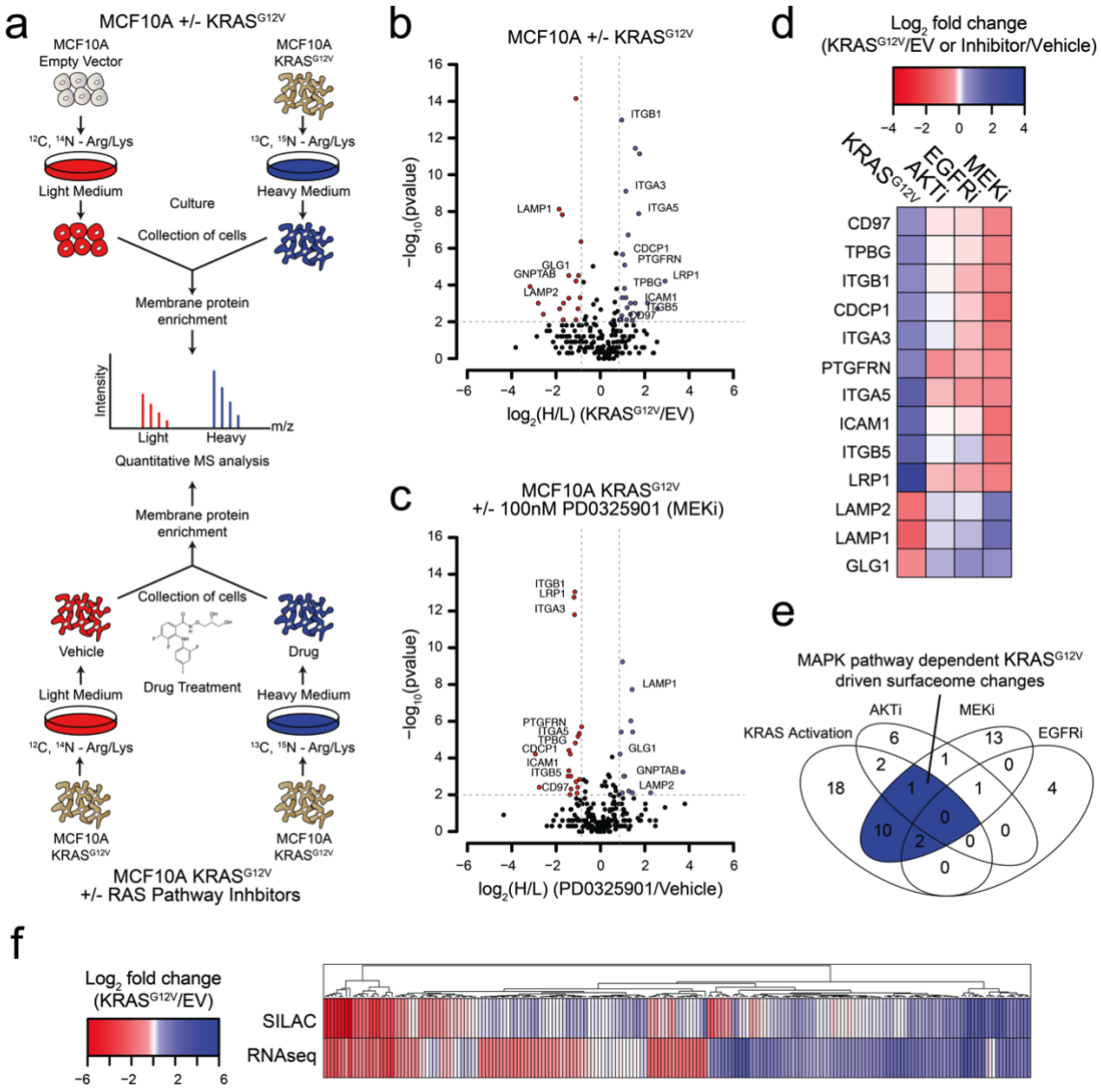

Figure 1-1. Oncogenic KRAS signaling coordinately regulates the expression of cell surface proteins in a model epithelial cell. (a) Experimental strategy for quantitative SILAC surface proteomics to compare surfaceomes of MCF10A empty vector cells to MCF10A KRAS^{G12V} cells (Top), or MCF10A KRAS^{G12V} cells treated with vehicle versus RAS pathway inhibitors (Bottom). Cells were cultured in either light or heavy SILAC media and then processed using N-linked cell surface glycoprotein enrichment and MS-based proteomic analysis. **(b)** Volcano plot of MCF10A empty vector versus

MCF10A KRAS^{G12V} cell-surface mass spectrometry experiment showing log_2 fold-changes in expression (X-axis) or $–log_{10}$(p-value)s (Y-axis). Proteins with a p-value less than 0.01 and a minimum of 1.75 fold increase (blue) or decrease (red) in SILAC ratio were considered significantly changed. Proteins labeled with text show expression patterns that were significantly altered by oncogenic KRAS signaling and inversely altered by MEKi. **(c)** Volcano plot representations of surface proteins in MCF10A KRAS^{G12V} cells with or without treatment with the MEK inhibitor (MEKi), PD0325901 (100nM). Proteins with a p-value less than 0.01 and a minimum of 1.75 fold increase (blue) or decrease (red) in SILAC ratio were considered significantly changed. Proteins labeled with text showed expression patterns that were significantly altered by oncogenic KRAS signaling and inversely altered by MEKi. **(d)** Heatmap representation of the SILAC mass spectrometry data for proteins that were significantly changed by both KRAS^{G12V} and MEKi. **(e)** Venn diagram showing overlap of targets founds in the SILAC mass spectrometry data for significantly altered proteins detected in all experiments. **(f)** Heatmap representation of a comparison between RNAseq and SILAC MS-based proteomics for all commonly identified genes. These data highlight the importance of quantifying cell-surface proteomes by mass spectrometry for higher confidence identification of candidate proteins for antibody generation.

We identified a total of 2943 tryptic peptides from ~500 proteins common in both the MCF10A cells with and without $KRAS^{G12V}$ (**Figure 1-2A).** Of 2943 tryptic peptides, 1460 contained the deamidated asparagine mass (0.984 Da) shift generated by N-glycanase treatment, providing high confidence it contained an asparagine-linked modification. Next, we eliminated proteins for which only a single peptide was identified, to distill to a higher confidence set. Lastly, the data was filtered bioinformatically to isolate proteins annotated in UniProt to be localized to the cell surface, resulting in 1257 high confidence peptides originating from 258 membrane associated proteins found in both light and heavy samples. Biological replicates showed 88% overlap in the common membrane proteins identified, and there was a good correlation between replicates in the up and downregulated proteins +/- $KRAS^{G12V}$ ($R^2 = 0.7676$) (**Figure 1-2B-C**). In total, we identified 17 proteins that were significantly upregulated, and 22 that were significantly downregulated (fold-change > +/- 1.75; p-value < 0.01) (**Figure 1-1B**). Gene ontology (GO) analysis of these significantly altered proteins in our datasets revealed significant enrichment for proteins involved in cell adhesion, cell motion, and cell-cell adhesion (**Figure 1-2D**).

We next wanted to understand how different signaling pathways emanating from RAS were contributing to the changes we observed in the surfaceome. We employed the same proteomics approach but instead examined the consequences of treatment with well-established pharmacological inhibitors, MEKi (PD0325901) and AKTi (MK2206) that block the two classic pathways downstream of RAS, MAPK and PI3K respectfully [18,19]. As a control, we also tested the effect of Gefitinib, which inhibits EGFR, a receptor

tyrosine kinase found upstream of RAS [20]. In each experiment, isotopically labeled MCF10A KRAS^{G12V} cells were treated with subtoxic concentrations of drug for 72 hours and compared to non-isotopically labeled vehicle treated MCF10A KRAS^{G12V} cells (**Figure 1-1A**). For the MEKi experiment, we were able to quantify the relative expression levels of 250 proteins (**Figure 1-1C**). Biological replicates showed similar overlap and

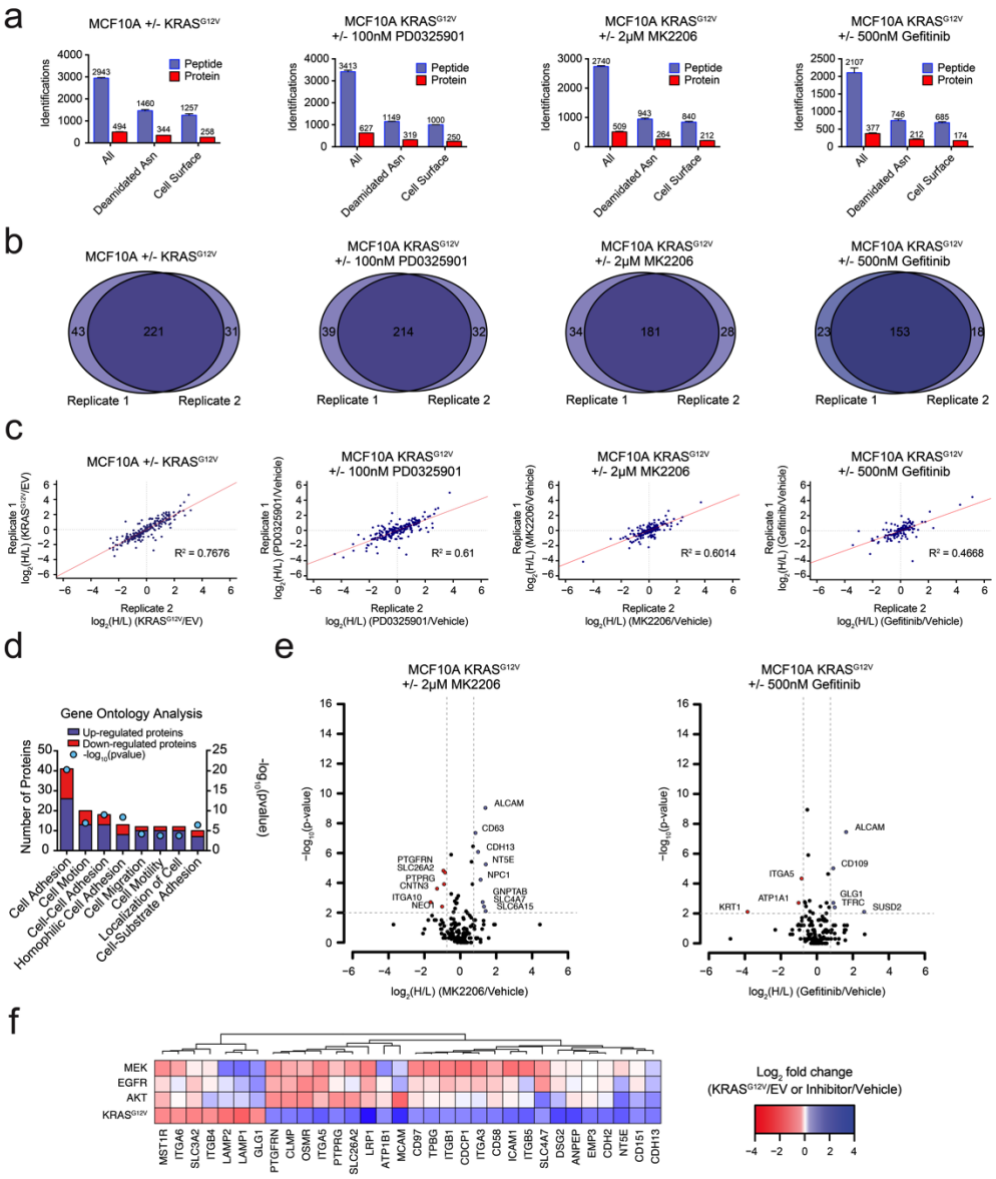

Figure 1-2. Oncogenic KRAS signaling coordinately regulates the expression of cell surface proteins in a model epithelial cell. (a) Bar graph representation of the total

number of unique peptides (blue) and proteins (red) identified by MS-based proteomics for each experiment. Data was bioinformatically triaged to remove peptides not containing the characteristic asparagine deamidation generated by PNGase digest and proteins not annotated as localized to the cell surface. **(b)** Venn diagram representation of the overlap of identified proteins between biological replicates demonstrates reproducibility for each experiment. **(c)** Scatter plots of SILAC ratios show reproducibility between biological replicates for each experiment. **(d)** Gene Ontology (GO) analysis of the cell-surface proteins significantly altered by expression of $KRAS^{G12V}$ **(e)** Volcano plot representations of the AKTi and EGFRi mass spectrometry experiments are shown. Proteins with a p-value less than 0.01 and a minimum of 1.75 fold increase (blue) or decrease (red) in SILAC ratio were considered significantly changed. **(f)** Heatmap representation of a comparison between proteins identified in all four proteomic experiments and significantly altered (fold-change > +/- 1.75; p-value < 0.01) in at least one dataset.

reasonable correlation in fold-changes in expression +/- MEKi (R^2 = 0.61), indicating biological and technical reproducibility (**Figure 1-2B-C**). Remarkably, 13 of the proteins that were significantly altered by $KRAS^{G12V}$ signaling were reversibly influenced by MEKi in the $KRAS^{G12V}$ cells (**Figure 1-1D**). By contrast, when the $KRAS^{G12V}$ cells were treated with AKTi or EGFRi, very few significant changes were observed (**Figure 1-1E and Figure 1-2E-F**). Others have shown the importance of the MAPK pathway for RAS-mediated transformation and tumerogenesis [4]. Consistent with previous reports, our findings indicate that the MAPK pathway is the dominant pathway by which RAS mediates influence on the surfaceome in the MCF10A model. Taken together with our unbiased GO analysis, these results suggest a model wherein RAS signaling through the MAPK pathway promotes the coordinate expression of proteins that may contribute to increased invasiveness, metastasis, and epithelial to mesenchymal transition.

To further characterize the influence of oncogenic KRAS on the surface proteome, we performed RNAseq on both the MCF10A empty vector control and $KRAS^{G12V}$ cells. The correlation between expression level changes observed in the SILAC proteomic data with those from RNAseq data (**Figure 1-1F**) was modest but significant (R^2 =0.422). This is not surprising as there are many possible points of regulation between synthesis of an mRNA and trafficking of a protein to the cell surface that can blur the connection between steady state RNA and protein levels. Others have reported similar levels of correlation between levels of cytosolic proteins and their mRNAs [21-23]. Nonetheless, the combination of the proteomic and transcriptomic data reinforces that KRAS transformation drives significant and coordinated changes in the cell surface. Additionally, we identified a large

cluster of genes found to be upregulated in both data sets; thus providing a set of high-confidence KRAS signaling surface markers for further validation.

Generation of recombinant antibodies that target the KRAS surfaceome

In order to orthogonally and rapidly validate these results in a variety of cellular settings, we needed robust molecular tools to detect and study KRAS regulated surfaceome proteins. Unfortunately, recombinant monoclonal antibodies are not commercially available for the vast majority of cell surface proteins [15]. Moreover, others have shown that up to half of all commercially available antibodies are unreliable [24]. Hence, we sought to generate and validate recombinant monoclonal antibodies for a set of the most interesting KRAS induced targets. Recombinant antibodies are particularly useful as they are renewable, thus creating a reliable resource. Furthermore, they can be bioengineered for many useful applications including therapeutic payload delivery and *in vivo* imaging. We leveraged the quantitative proteomic and RNAseq data to manually choose seven high-confidence KRAS-induced single-pass transmembrane receptors to advance to a recombinant antibody engineering campaign. We chose single-pass receptors as they are more amenable to antibody discovery using soluble extracellular domains (ECD) and were well-represented in our data. All candidates were at least 2-fold upregulated as observed by mass spectrometry in the $KRAS^{G12V}$ cells as compared to empty vector. In most cases, the candidates were also at least 2-fold upregulated in the same context as determined by RNAseq. The representative targets had a range of functions critical for tumor survival. For example, CDCP1, ICAM1, and ITGB5 all play a role in cell adhesion and migration [25,26]; NT5E is a nucleotidase that contributes to

immune cell evasion [27]; LTBR is a cytokine receptor involved in maintenance of lymphoid microenvrionments [28]; CD55 is a complement system inhibitor [29], and ANPEP is a protease thought important for metastasis [30].

To enable the rapid expression and purification of these target proteins for generation of antibodies by phage display, we expressed their ECDs as Fc-fusion proteins in mammalian cells (**Figure 1-3A**) [31]. We introduced a biotin-acceptor-tag at the C-terminus, and a TEV proteolysis site between the ECD and Fc-domain. These tags allowed for site-selective capture of the ECD-Fc fusion on magnetic streptavidin beads, and release of each ECD containing bound Fab-phage after TEV treatment. This 'catch-and-release' strategy ensured selective release of Fab-phage bound to each ECD, while avoiding enrichment of unwanted Fab-phage that either bound the Fc-domain or the streptavidin beads [32] **(Figure 1-3B)**. To facilitate production of the biotinylated construct, a stable HEK293T cell line was engineered to overexpress the bacterial biotin ligase, BirA, with an ER retention tag. This allowed for site-specific biotinylation to be performed in cells, thus eliminating the need for *in vitro* labeling. Western blots confirmed that these cells expressed and secreted quantitatively (typically >90%) biotinylated Fc-fusion proteins (**Figure 1-4A**). Each Fc-fusion protein was transiently expressed in the engineered HEK293T cells and purified by Protein A affinity purification from the media for use in phage-antibody selections. We conducted 4 rounds of "catch-and-release" selections with a well-validated synthetic Fab-phage library [33]. After each selection, we isolated 95 individual phage clones and screened them for target binding by phage ELISA followed by DNA sequencing (**Figure 1-3C and Figure 1-4B**). Selections resulted in the

identification of 116 unique antigen-binding sequences against the seven ECD-Fc fusion targets **(Figure 1-4D)**. None of these clones demonstrated appreciable binding to the Fc-domains fused to the antigen, a testimony to the efficiency of the catch-and-release strategy. For further characterization, each Fab was cloned into an *E. coli* secretion plasmid and expressed, typically in yields ranging from 1-10 mg/L. Fabs were purified from the periplasm by Protein A purification for further analysis.

To validate the antibodies, we adopted several of the tests recently recommended by the Working Group for Antibody Validation [34]. Firstly, we generated a stable cell line for each target that overexpressed the protein ECD fused to a fluorescent protein expression reporter and a generic single-pass transmembrane domain (**Figure 1-4C**). Selections to each of the seven targets produced multiple antibodies showing dramatically increased binding to cells over-expressing the target ECD as compared to control cells (**Figure 1-4D**). We further validated the specificity of the antibodies using CRISPRi knockdown of each target in the MCF10A $KRAS^{G12V}$ cells [35]. In each case, we identified at least one antibody that showed significant staining on the MCF10A $KRAS^{G12V}$ cells and little to no binding for the CRISPRi knockdown corresponding cell line (**Figure 1-3E**). Importantly, these data also corroborated the proteomics observation that these membrane proteins are highly expressed in the MCF10A $KRAS^{G12V}$ cells.

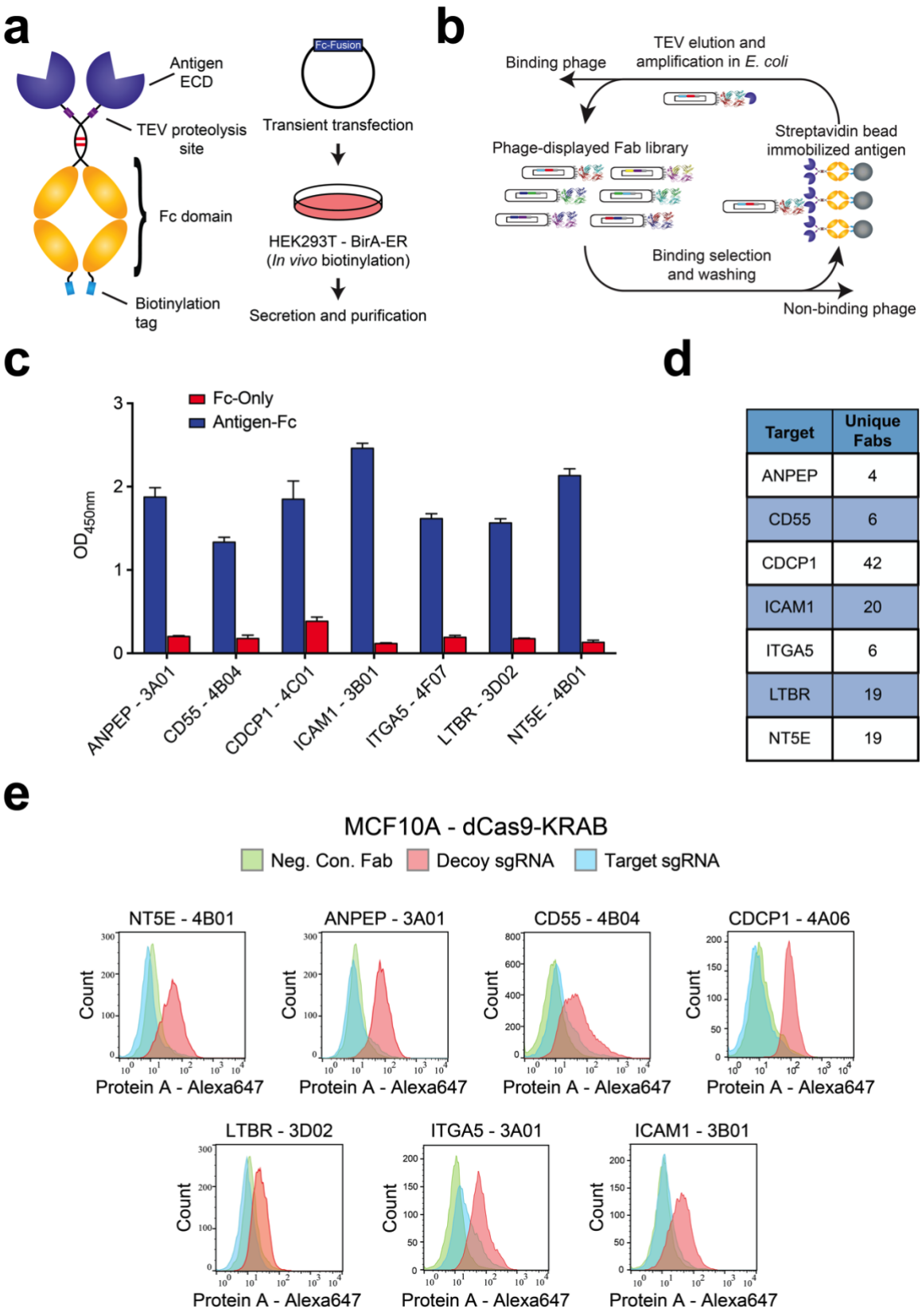

Figure 1-3. Generation and validation of antibodies to oncogenic KRAS upregulated surface proteins. (a) (Left) Schematic of the Fc-fusion construct developed for rapid expression of membrane protein extracellular domains. Each extracellular

domain was expressed as a TEV cleavable site-specifically biotinylated Fc-fusion. (Right) HEK293T cells stably expressing an ER-localized biotin ligase are transiently transfected with the Fc-fusion expression vector. Proteins are quantitatively biotinylated *in-vivo*, secreted into the cellular media, and purified by Protein A affinity purification. **(b)** Shown is the strategy for phage display generation of antibodies to each RAS induced protein ECD. Proteins were immobilized on streptavidin magnetic beads and mixed with a highly diverse phage-displayed Fab library. Non-binding phage were removed by washing and phage bound protein was released by enzymatic treatment with TEV protease. Eluted phage were propagated in *E. coli* and the selection process was iterated for 3-4 rounds to enrich the library for specific protein binders. **(c)** Representative phage ELISAs from selections against seven proteins seen elevated in expression level by oncogenic KRAS signaling in MCF10As. Phage clones show strong binding to cognate protein Fc-fusions but little detectable binding to the isolated Fc-domain suggesting binding to the targeted ECD. **(d)** Table of the number of unique antibody clones generated against each of the specified KRAS upregulated targets. **(e)** Representative flow cytometry histograms demonstrate specific cellular target engagement of Fab clones generated against seven KRAS driven surface proteins. MCF10A cells stably expressing dCas9-KRAB and a decoy sgRNA (red) or target sgRNA (blue and green) were labeled with either a negative control Fab (green) or a Fab of interest (red and blue). Fab binding to cells was detected by addition of a Protein A Alexa647 conjugate and quantification by immunofluorescence flow cytometry.

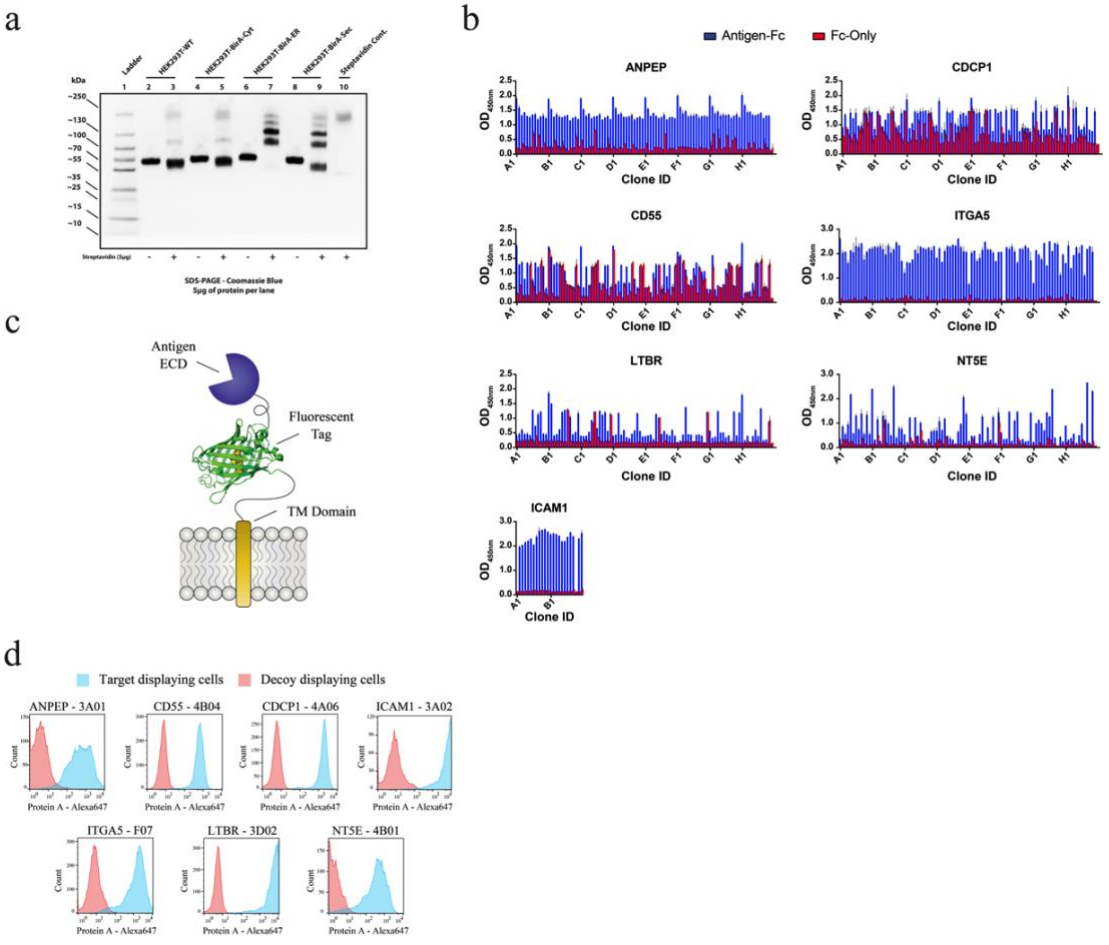

Figure 1-4. Generation and validation of antibodies to oncogenic KRAS upregulated surface proteins. (a) Western blot analysis of Fc-fusion protein endogenous biotinylation. Expression in WT HEK293T cells was compared to expression in HEK293T cells stably expressing BirA localized to the cytosol (Left), the endoplasmic reticulum (Middle), or secreted into the extracellular space (Right). The amount of biotinylation was estimated by assessment of band migration by SDS-PAGE after co-incubation of the purified Fc-fusion with streptavidin. Expression in cells expressing ER-localized BirA showed quantitative biotinylation (>98%). **(b)** Phage ELISAs from selections against seven proteins elevated in expression level by oncogenic KRAS signaling in MCF10As. Phage clones that showed strong binding to cognate protein Fc-fusions but little detectable binding to the isolated Fc-domain were advanced for further characterization. **(c)** Schematic of the construct used to display each protein on the surface of HEK293 (T-Rex-293) cells for validation of antibody specificity. **(d)** Representative flow cytometry histograms demonstrate specific cellular target engagement of Fab clones raised against seven RAS driven surface proteins.

Validation of oncogenic KRAS-induced membrane proteins

To orthogonally validate the observations made by MS-based proteomics and RNAseq analysis, we measured the relative cell-surface abundance of each protein by flow cytometry using our recombinant antibodies. Gratifyingly, all seven proteins showed elevated expression on the MCF10A $KRAS^{G12V}$ cells relative to the empty vector control (**Figure 1-5A**). Moreover, the flow cytometry data generated with the Fabs generally correlated with the proteomic measurements. These results were further confirmed by immunofluorescence (IF) for a subset of the targets, where we observed both differential expression and cell surface localization in each case (**Figure 1-5B**).

Next, we expanded beyond the isogenic MCF10A cell model to measure the relative expression of the target proteins on a panel of tumorigenic cells that included lung, colorectal, and pancreatic cancer cell lines known to harbor oncogenic RAS mutations (**Figure 1-5C**). These three cancer types have the highest occurrence of oncogenic KRAS. For five of the seven targets (CDCP1, CD55 NT5E, ICAM1 and LTBR) we observed high levels of expression in at least half of the eight cancer cell lines. Most strikingly we observed that one protein, CDCP1, was ubiquitously abundant in expression across the entire panel. In contrast, two of the proteins, ANPEP and ITGA5, showed little detectable expression in all cases. In general, variability of expression should not be surprising, as these cells vary in tissue origin and also harbor other cancer driving mutations beyond oncogenic RAS. While ANPEP and ITGA5 may be present if we were to screen a larger panel of cells, another possibility is that they are proteins specific to the

MCF10A cell surface. Importantly, a HEK293T control showed no expression of any of the targets.

If the pattern of protein expression we observed was due to RAS signaling then we hypothesized that it should be responsive to RAS pathway inhibitors. Indeed, several of these proteins (CD55, NT5E, CDCP1, and ICAM1) had expression that was modulated by KRAS pathway perturbation, while inhibition upstream of KRAS by EGFRi had little effect in most cases (**Figure 1-5D**). Interestingly, AKTi inhibition caused increased expression of CDCP1, NT5E, and CD55 in multiple cases. A potential explination is that MK-2206 inhibition resulted in feedback driven MAPK signaling as has been previously observed[36]. Also noteable was that MEK inhibition resulted in highly decreased CDCP1 expression levels in nearly every cell line tested. This is consistent with our observations in the MCF10A cells and with previous reports in mutant RAS non-small cell lung cancer cells[37]. We further validated this result by western blot, demonstrating that MAPK signaling drives both CDCP1 expression and cell-surface localization (**Figure 1-5E**). Taken together, our antibody profiling provides evidence suggesting oncogenic RAS can indeed influence the expression of membrane proteins at the cell surface. Moreover, we believe this collection of highly specific recombinant antibodies constitute an expandable and enriched tool kit that may be useful for interrogating RAS transformed cells and tissues.

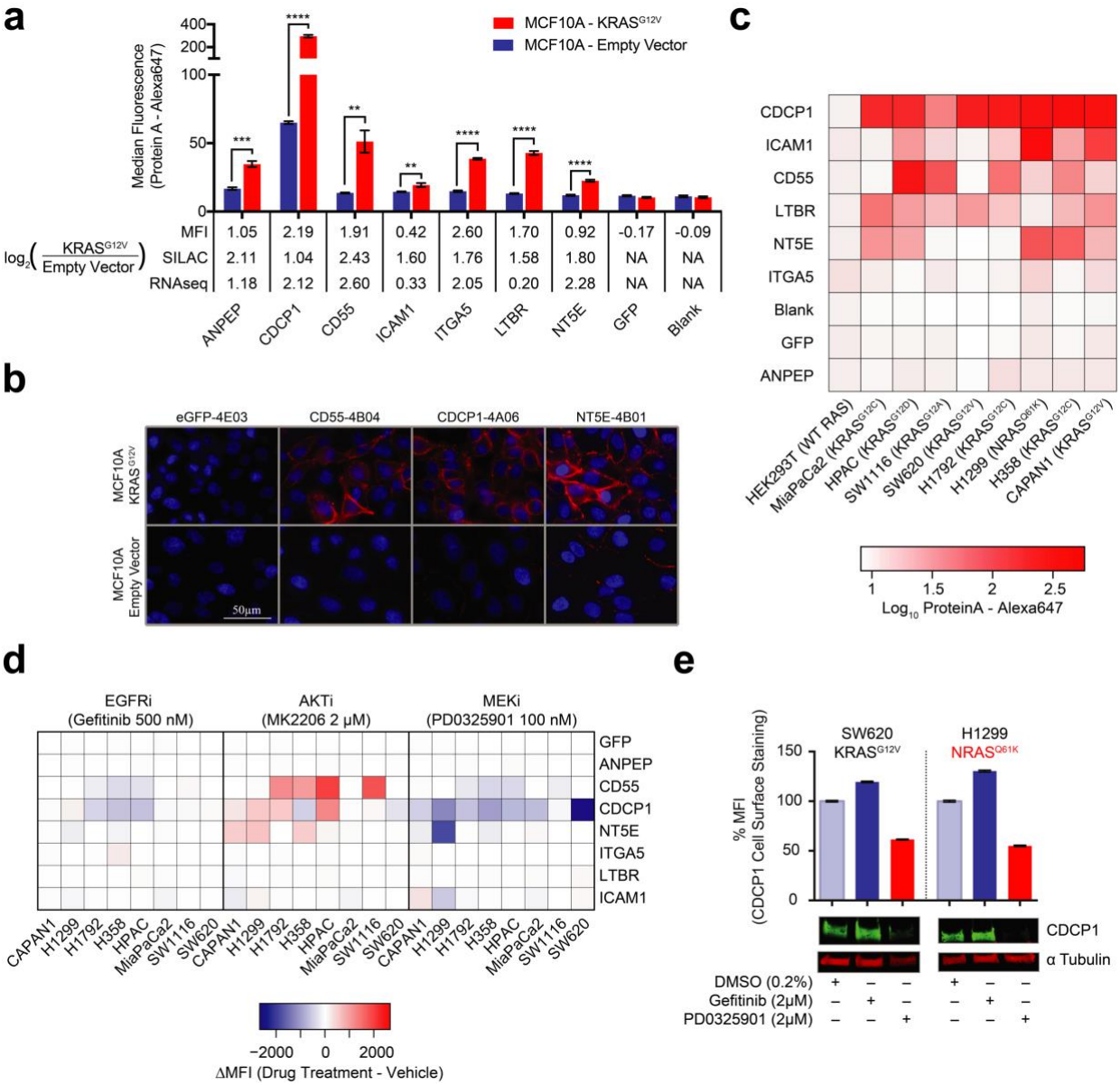

Figure 1-5. Validation of oncogenic KRAS-induced cell surface proteins with recombinant antibodies. (a) Seven proteins were confirmed to be upregulated on the MCF10A KRAS^{G12V} cells by flow cytometry using specific recombinant antibodies (n = 3, error bars represent s.d.). The table below compares $\log_2$ fold-changes as measured by flow cytometry, SILAC proteomics, and RNAseq. **(b)** Representative immunofluorescence images demonstrate orthogonal confirmation of KRAS driven differential expression and cell surface localization of target proteins. **(c)** Heatmap representation of flow cytometry median fluorescent intensity values for eight Fabs against nine tumorigenic cell lines. **(d)** Heatmap representation of flow cytometry median fluorescent intensity values for eight Fabs against nine tumorigenic cell lines treated with RAS pathway inhibitors. **(e)** Flow cytometry and western blot profiling of CDCP1 expression levels in response to RAS pathway inhibitors.

Functional characterization of the KRAS surfaceome in MCF10As using a CRISPRi screen

In addition to identifying proteins upregulated by expression of oncogenic KRAS, we explored how oncogenic KRAS signaling can influence the dependence of cells on surface proteins. We tested the impact on cell proliferation of selective knockdown of more than 1600 annotated membrane proteins using CRISPRi (**Figure 1-6A**). Importantly, these target proteins included nearly all of those found in our mass spectrometry screen. We introduced the stable expression of dCas9-KRAB into both the wild type and $KRAS^{G12V}$ MCF10A cells using well-established constructs and standard lentiviral transduction [38]. We transduced a surfaceome targeted lentiviral sgRNA library consisting of 5 sgRNAs per gene and 150 non-targeting controls into either the $KRAS^{G12V}$ MCF10A or the parental cell line. Cells were grown for 12 days, and at least 10 doublings. The MCF10A cells require the addition of growth factors (EGF, Insulin) to proliferate, whereas $KRAS^{G12V}$ MCF10A cells are growth factor independent. Thus, we screened the $KRAS^{G12V}$ MCF10A cells with and without growth factors in an attempt to maintain KRAS addiction while knocking down genes. After conducting the three screens, cells were harvested and genomic DNA was isolated. The sgRNA barcodes were PCR amplified and subjected to next generation sequencing (NGS) to quantify the effect of each sgRNA on growth rate. Genes were scored based on the average phenotype of the 3 strongest sgRNAs and p-values were calculated by a Mann-Whitney test against a non-targeting control set as previously described [38,39]. Remarkably, knock down of more than fifty genes caused a significant reduction (phenotype<-1 and p-value<0.05) in growth rate in the $KRAS^{G12V}$ cells grown without growth factor, while only four genes caused a significant

growth advantage when knocked down (**Figure 1-6B**). Interestingly, there were only 12 genes in the wild type MCF10A cells and 8 genes in the KRAS^{G12V} cells grown with growth

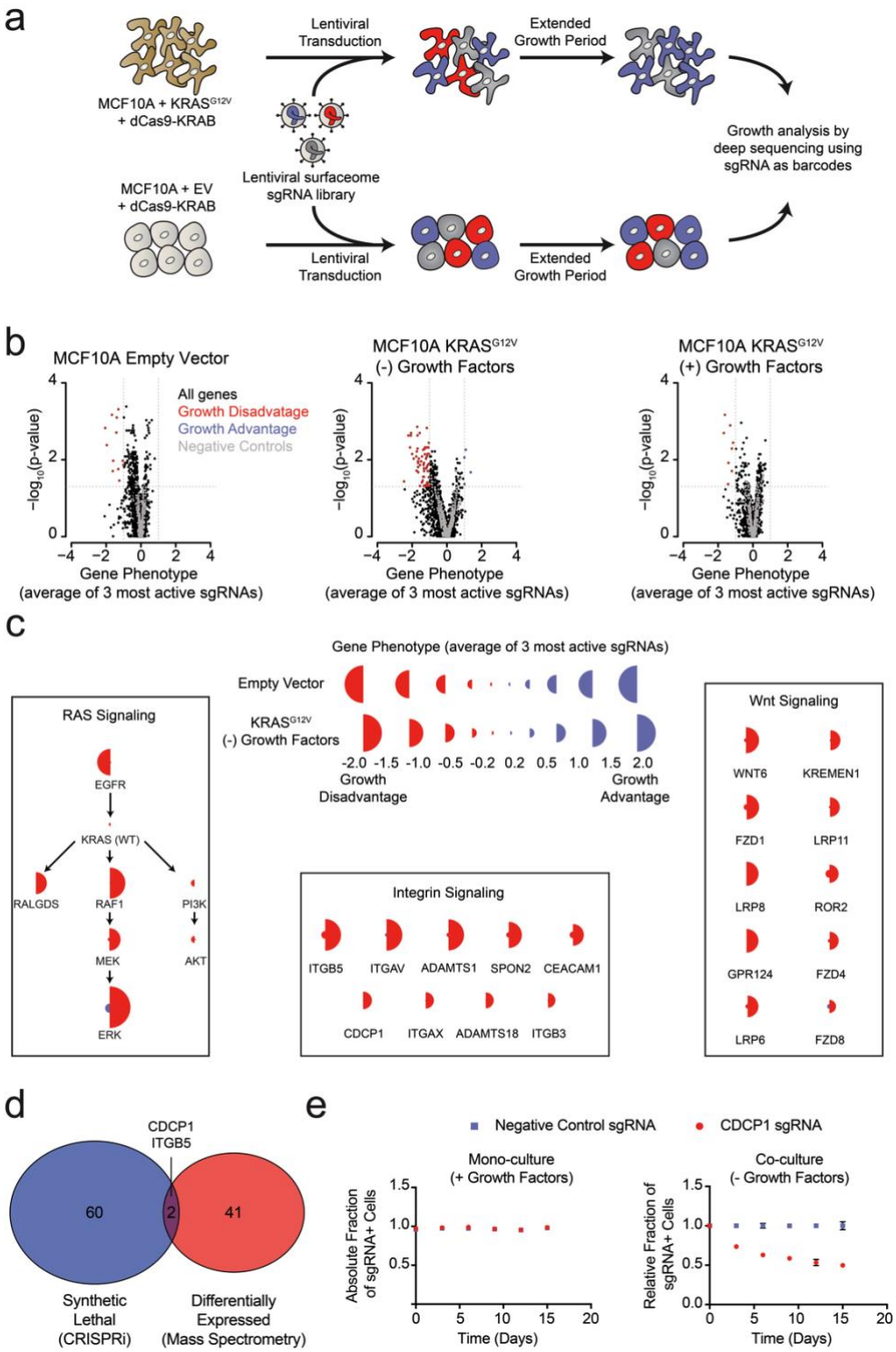

Figure 1-6. Systematic characterization of the functional importance of the KRAS surfaceome. (a) Experimental strategy for the CRISPRi surfaceome screen. MCF10A

Empty Vector or MCF10A $KRAS^{G12V}$ cells were transduced with a lentiviral surfaceome sgRNA library containing 5 guides each for 1605 transmembrane targets. After being cultured for an extended growth period, the abundance of each sgRNA barcode was quantified by deep sequencing. **(b)** Volcano plots of the CRISPRi experiment showing gene phenotype (X-axis) versus $-\log_{10}$(p-value)s (Y-axis). Proteins with a p-value less than 0.05 and a gene phenotype >1 (blue) or <-1 (red) were considered significant. **(c)** Shown is a representation of CRISPRi phenotypes for RAS pathway control genes (Left), functionally categorized $KRAS^{G12V}$ synthetic lethal genes including integrin signaling genes (Middle), and Wnt Signaling genes (Right). $KRAS^{G12V}$ synthetic lethal genes were defined as having a p-value < 0.025 and a phenotype > 0.8 for $KRAS^{G12V}$ cells and < 0.8 for Empty Vector cells. **(d)** A Venn diagram comparing $KRAS^{G12V}$ synthetic lethal genes and differentially expressed genes. **(e)** Competitive growth assays performed with $KRAS^{G12V}$ cells transduced with the indicated CDCP1 and negative control sgRNAs. Cells were grown in monoculture with growth factors to ensure they maintained sgRNA expression (Left), and in co-culture with cells lacking sgRNA expression without growth factor to determine relative growth rates (Right). (n = 3, error bars represent s.d.)

factor that showed a growth disadvantage, and none that were increased. We individually tested sgRNAs derived from the screening library for several genes in both cell lines and the results robustly confirmed the screening results. (**Figure 1-7**).

In addition to the membrane protein genes targeted in our sgRNA library, we also included a set of known RAS pathway genes (**Figure 1-6C**). Not surprisingly, EGFR was critical for growth of wild type MCF10A grown in the presence of EGF. However, it was not critical to the $KRAS^{G12V}$ cells grown either in the presence or absence of growth factors, which reflects the fact that constitutively active $KRAS^{G12V}$ can drive the growth of these cells independently of EGFR signaling. Furthermore, the $KRAS^{G12V}$ cells showed a strong dependence on proteins within the MAPK signaling pathway (RAF/MEK/ERK) and little to no dependence on the PI3K/AKT pathway, consistent with previous reports highlighting the importance of RAS driven MAPK signaling [4]. Interestingly, RALGDS, a lesser-studied RAS effector protein, was of intermediate importance relative to MAPK and PI3K. Taken together, these results provide mechanistic insight as to how oncogenic KRAS drives signaling in MCF10A transformed cells. These self-consistent data in MCF10A cells recapitulate many known features of oncogenic RAS signaling, and rationalize the CRISPRi screening results. The set of genes that are critical for the growth factor independent proliferation of $KRAS^{G12V}$ cells but unimportant for the growth of wild type cells notably fell into two main categories (**Figure 1-6C**). One group constitutes core components of integrin-mediated cell adhesion, while the other included major proteins involved in Wnt signaling. Recently, others have observed an essential role for Wnt

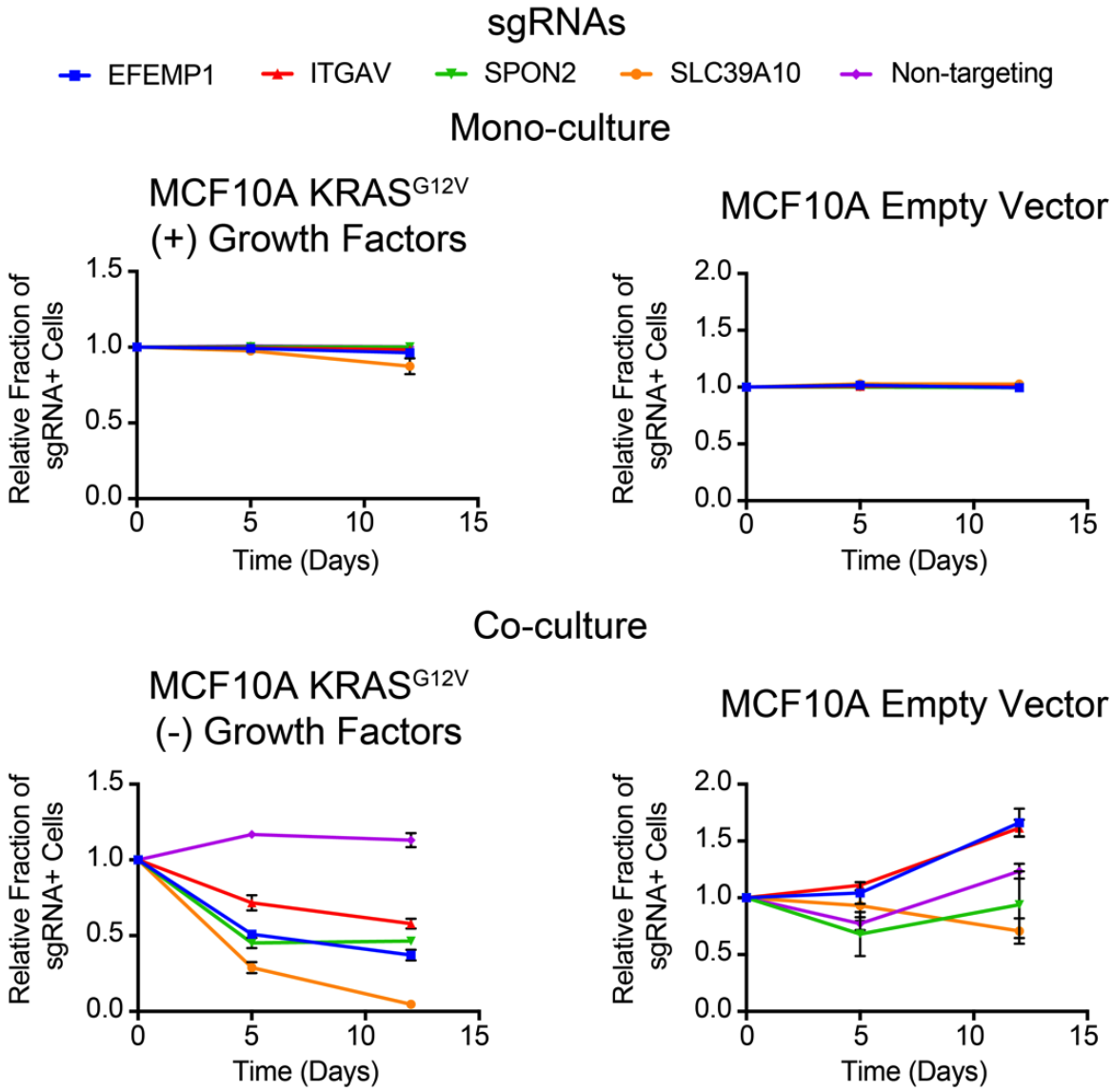

Figure 1-7. Competitive growth assays performed with KRAS^{G12V} (Left) and Empty Vector (Right) MCF10A cells transduced with the indicated sgRNAs. Cells were grown in monoculture (Top) with growth factors to ensure they maintained sgRNA expression and in co-culture (Bottom) with cells lacking sgRNA expression to determine relative growth rates. (*n* = 3, error bars represent s.d.)

signaling in KRAS malignancies, a finding which our data recapitulates[40]. Additionally, the CRISPRi results suggest a previously underappreciated dependency on integrin signaling proteins at the cell surface for growth factor independent proliferation driven by oncogenic KRAS.

Remarkably, there was very little overlap for proteins upregulated by KRAS as measured by mass spectrometry, and those showing synthetic growth reduction with KRAS in the CRISPRi screen (**Figure 1-6D**). This is not surprising since differential expression and acquired essentiality are different properties. However, two genes were identified as hits in both experiments, ITGB5 and CDCP1. CDCP1 has been previously implicated as an elevated marker in solid cancers and a driver of cancer cell growth, metastasis, and tumor progression [41,42]. CDCP1 was also observed in our earlier discovery proteomics screen using several membrane enrichment methods [14]. Interestingly, several groups have demonstrated that CDCP1 signaling can be mediated by interactions with integrins [9,43]. Using an individual sgRNA to CDCP1, we observed a ~40% reduction in growth over 15 days of $KRAS^{G12V}$ cells with CDCP1 knocked down (**Figure 1-6E**). We confirmed that CDCP1 was indeed >98% reduced in expression by antibody staining.

While our results provide a large number of interesting proteins for follow-up, we decided to focus on targeting CDCP1 with our validated recombinant antibodies. Our antibodies did not appear to functionally inhibit CDCP1 (data not shown), however we were motivated by the fact that we find it over-expressed in many RAS-driven cell lines.

Moreover, its essentiality makes it unlikely to be down-regulated as a resistance mechanism. These qualities suggest that CDCP1 could be a particularly attractive target for an antibody drug conjugate (ADC).

Antibodies can selectively deliver toxic and immunotherapy payloads to mutant KRAS pancreatic cancer cells

Oncogenic KRAS is nearly ubiquitously expressed in pancreatic cancers and these cancers are particularly dependent on MAPK pathway signaling [44]. Thus, we profiled CDCP1 expression levels on a panel of human Pancreatic Ductal Adenocarcinoma Cancer (PDAC) cell lines, and observed a high level of expression of CDCP1 relative to no observable expression on non-tumorigenic pancreatic duct cells, HPNE (**Figure 1-8A**). Indeed, quantification of the protein copy number of CDCP1 on the HPAC PDAC cells revealed that these cells were expressing ~2.9 million copies per cell (**Figure 1-9A**). Such high level of expression is rare, and is an important consideration for therapeutic targeting by ADCs [45]. Moreover, cells containing oncogenic RAS are known to be very active in protein uptake by macropinocytosis and lysosomal degradation [46], making an ADC strategy even more attractive.

We tested the ability of one of our recombinant CDCP1 antibodies to selectively deliver a cytotoxic payload to mutant KRAS tumor cells. Having the recombinant form facilitated simple conversion of the Fab to an IgG1 for the experiment. The HPAC or non-tumorigenic HPNE cells were treated with CDCP1 IgG1 that can bind a commercially

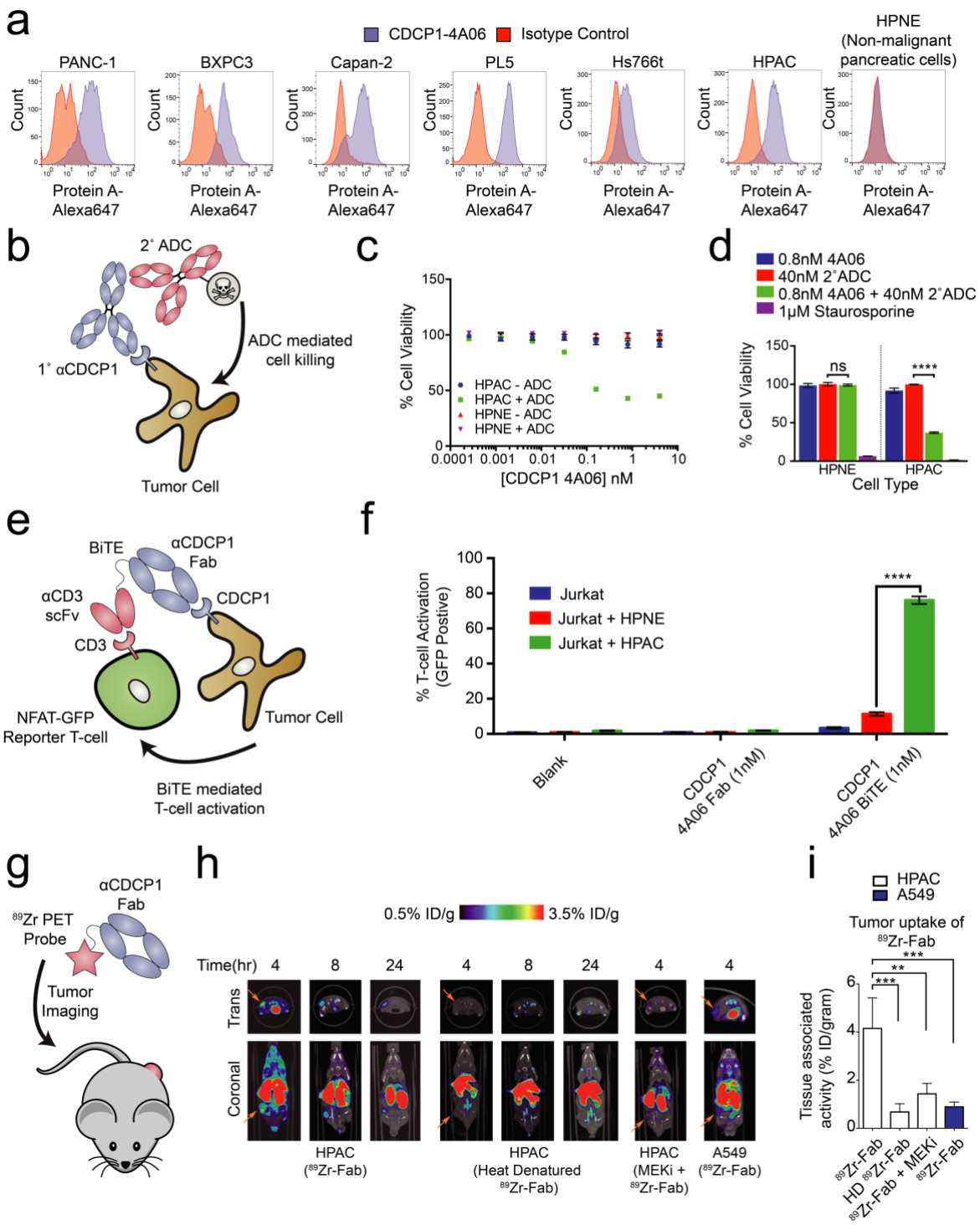

Figure 1-8. Systematic approaches to demonstrate the utility of the recombinant antibodies to target and detect RAS signaling in pancreatic ductal adenocarcinoma (PDAC). (a) Profiling of a panel of pancreatic ductal adenocarcinoma cells by flow cytometry demonstrates that CDCP1 is highly expressed on PDAC cells. Remarkably, CDCP1 was not detectably expressed on non-tumorogenic cells derived from the same tissue origin. **(b)** A schematic representation of the antibody drug conjugate cell-killing

assay. Cells were treated with a primary IgG that targets CDCP1 and a secondary anti-human IgG conjugated to the cytotoxic drug monomethyl auristatin F (MMAF). Cellular viability was quantified by CellTiter-glo® after 72 hours incubation with antibody treatment. **(c)** Dose dependent antibody drug conjugate mediated cell killing was only observed in the HPAC tumorigenic cells and not in the non-tumorogenic HPNE cells (*n* = 3, error bars represent s.d.). **(d)** Sub-nanomolar treatment with a CDCP1 IgG was sufficient to selectively kill greater than 50% of HPAC cells, but only when in combination with a stoichiometric excess of the secondary antibody drug conjugate (*n* = 3, error bars represent s.d.). **(e)** Schematic of the experimental setup for the flow cytometry-based T-cell activation assay used to profile BiTE activity. Cells were incubated with HPAC or HPNE target cells in the presence or absence of antibody treatment. After overnight incubation, T-cell activation was quantified via the expression of NFAT-dependent GFP reporter gene. **(f)** Jurkat cells were significantly activated when treated with 1nM BiTE in the presence of HPAC target cells as compared to HPNE control cells. Importantly treatment with the CDCP1 BiTE alone or with Fab lacking the CD3 targeting component resulted in no significant T-cell activation. **(g)** Expression levels of CDCP1 on two KRAS mutant cancer cell lines was profiled by intact cell flow cytometry (top) and western blotting (bottom). Consistent with proteomics observations in the MCF10A $KRAS^{G12V}$ cells, expression and cell-surface localization of CDCP1 was depleted by MEK inhibition but refractory to EGFR inhibition. **(h)** Representative microPET images of four immunocompromised nu/nu mice bearing cancer xenografts targeted with a ^{89}Zr-labeled CDCP1 Fab. Images over time show the tumor specific expression of CDCP1, as well as the persistent binding of the Fab to the tumor over 24 hours (Left). Importantly, when the same Fab was heat denatured prior to injection or when a negative control xenograft was used, there was no observable uptake of the ^{89}Zr-Fab (Middle and Right). Remarkably, no uptake was observed in the mouse treated with a sub-toxic dose of MEKi prior to imaging, demonstrating the coupling of CDCP1 expression MAPK pathway signaling *in-vivo*. **(i)** Quantification of tumor specific bio-distribution of the CDCP1 ^{89}Zr-Fab in tumor bearing nu/nu mice (n=5 per treatment arm) confirms the trends observed by microPET imaging. Tumor localization of ^{89}Zr-Fab was antigen dependent and ablated by specific inhibition of MAPK signaling.

available secondary antibody coupled to a non-cell permeable cytotoxic microtubule inhibitor Monomethyl Auorstatin F (MMAF) (**Figure 1-8B**). We found that while the normal HPNE cells were unaffected by treatment of up to 20nM of antibody complex, oncogenic KRAS containing HPAC cells were sensitive to ADC treatment at concentrations as low as 10pM. (**Figure 1-8C**). More than 60% reduction of viability was observed at 0.8 nM (**Figure 1-8D**), suggesting that the CDCP1-selective antibody can selectively internalize and deliver the cytotoxic payload. Similar levels of toxicity were observed in two additional mutant RAS cancer cell lines (**Figure 1-10**). It is not surprising that all cells were not killed since these are rapidly dividing cells in culture that create a steady state of apoptosis and proliferation. It is also possible that directly coupling MMAF to the recombinant antibody could further improve its potency as an ADC.

Recently, the FDA approved the first example of a bispecific T-cell engager (BiTE) antibody immunotherapy that binds both a tumor selective antigen, and CD3 on the surface of cytotoxic T-cells [47]. The BiTE recruits the T-cell to the tumor cell, induces T-cell activation, and tumor cell killing. Many similar BiTEs are currently being tested in the clinic [48]. We hypothesized that the CDCP1 recombinant Fab could be engineered in a BiTE modality to selectively target oncogenic KRAS PDAC cells. We genetically fused the CDCP1 Fab to the clinically utilized OKT3 anti-CD3 scFv, and tested whether it could be used to mediate T-cell activation with an NFAT-GFP reporter Jurkat T-cell in co-culture (**Figure 1-8E)**. Remarkably, 1nM of the CDCP1 BiTE was sufficient to activate 75% of T-cells when co-cultured with mutant KRAS HPAC cells, while co-culture with HPNE cells,

or treatment with BiTE lacking the anti-CD3 scFv, resulted in minimal activation (**Figure 1-8F**).

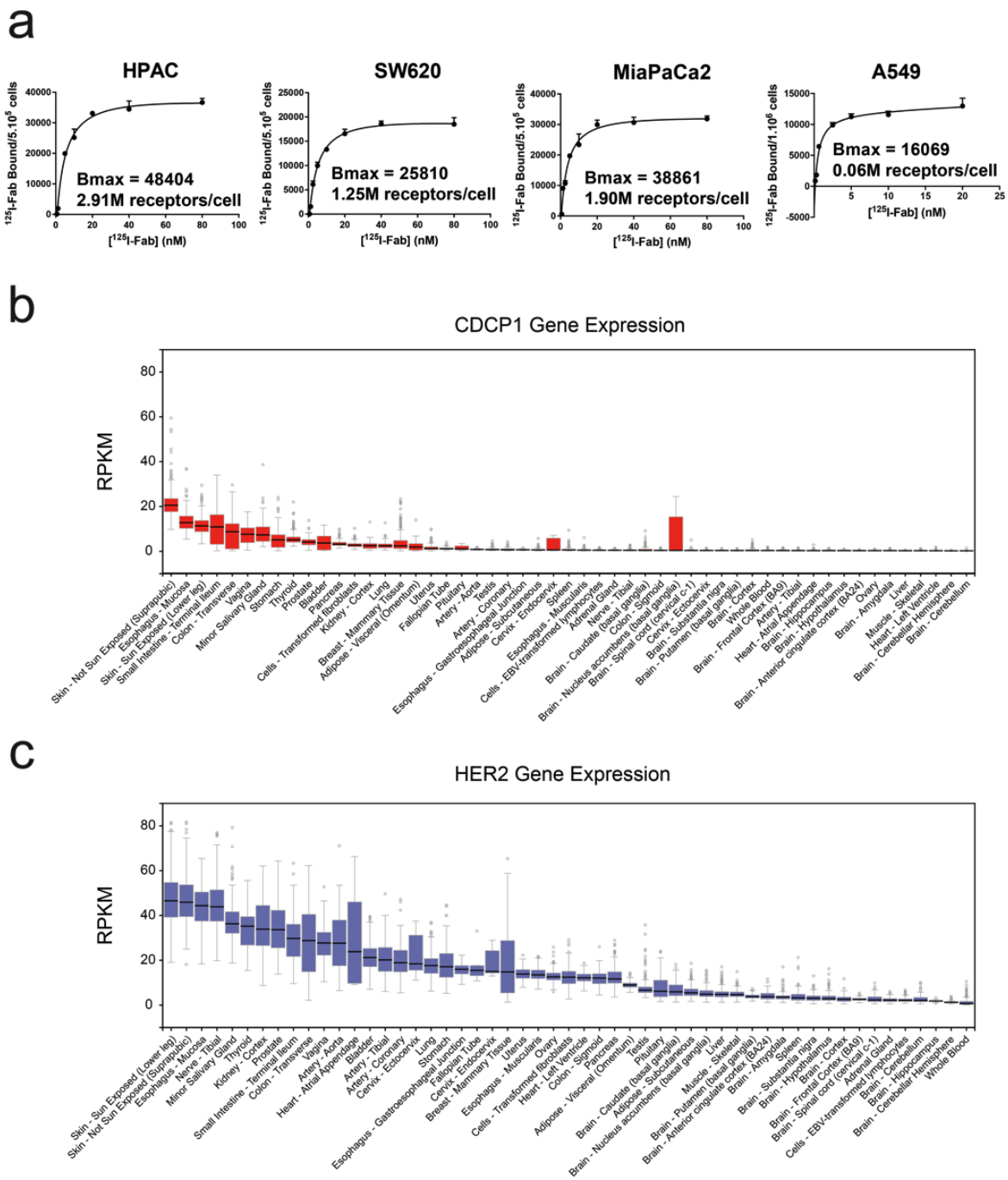

Figure 1-9. Characterization of CDCP1 expression levels in cancer cell lines and normal human tissues. (a) Bmax determination for CDCP1 expression on HPAC, SW620, MiaPaCa2, and A549 cells using a titration of ^{125}I labeled CDCP1-4A06 Fab. **(b)**

GTEx database analysis of the tissue specific gene-expression of CDCP1 shows limited expression in normal tissues. **(c)** GTEx database analysis of the tissue specific gene-expression of HER2, a classically targeted cell-surface protein overexpressed in sub-types of breast cancer.

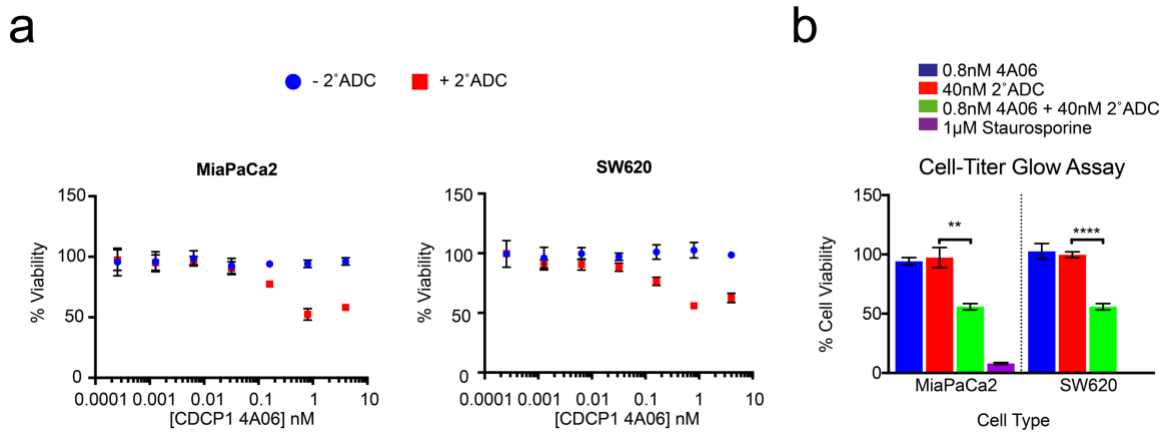

Figure 1-10. Application of recombinant antibody drug conjugates to target RAS signaling in cancer. (a) Dose dependent antibody drug conjugate mediated cell killing was for MiaPaCa2 and SW620 tumorigenic cells (*n* = 3, error bars represent s.d.). **(b)** Sub-nanomolar treatment with a CDCP1 IgG was sufficient to selectively kill nearly 50% of MiaPaCa2 and SW620 cells, but only when in combination with a stoichiometric excess of the secondary antibody drug conjugate (*n* = 3, error bars represent s.d.).

Application of antibodies for *in-vivo* detection of oncogenic RAS-dependent MAPK signaling

As a final proof of concept application of our antibodies, we tested to see whether CDCP1 expression level could be used as an *in vivo* imaging marker for RAS signaling in a mouse xenograft model for pancreatic cancer (**Figure 1-8G**). The CDCP1-4A06 Fab was labeled with a positron-emitting radioisotope ^{89}Zr and used for positron-emission-tomography (PET) imaging in mice with mutant RAS HPAC xenographs. We deliberately chose a Fab as it has a relatively short half-life so would be cleared rapidly to reveal possible tumor staining. As a negative control, ^{89}Zr-Fab was heat denatured prior to administration. As an additional control, we used xenograft mouse models with A549 cells that express only 60,000 copies of CDCP1 per cell (**Figure 1-9A**). Although A549 cells also harbor an oncogenic RAS mutation, previous work has shown that growth and MAPK signaling in these cells are not significantly diminished by knockdown of KRAS [49]. Within four hours of administration of the ^{89}Zr-Fab, tumor localization was observed, and by eight hours staining was highly pronounced (**Figure 1-8H**). Significantly reduced tumor staining was observed using the heat denatured ^{89}Zr-Fab. Strikingly, in the HPAC xenograft mice treated with subtoxic MEKi, ^{89}Zr-Fab tumor localization was also highly diminished. These animal data provide further evidence to the hypothesis that CDCP1 expression is a direct consequence of RAS dependent MAPK signaling even in the complex milieu of a tumor. Excised tumors were used to quantify PET signal, confirming the trends seen in the qualitative images (**Figure 1-8I and Figure 1-11**).

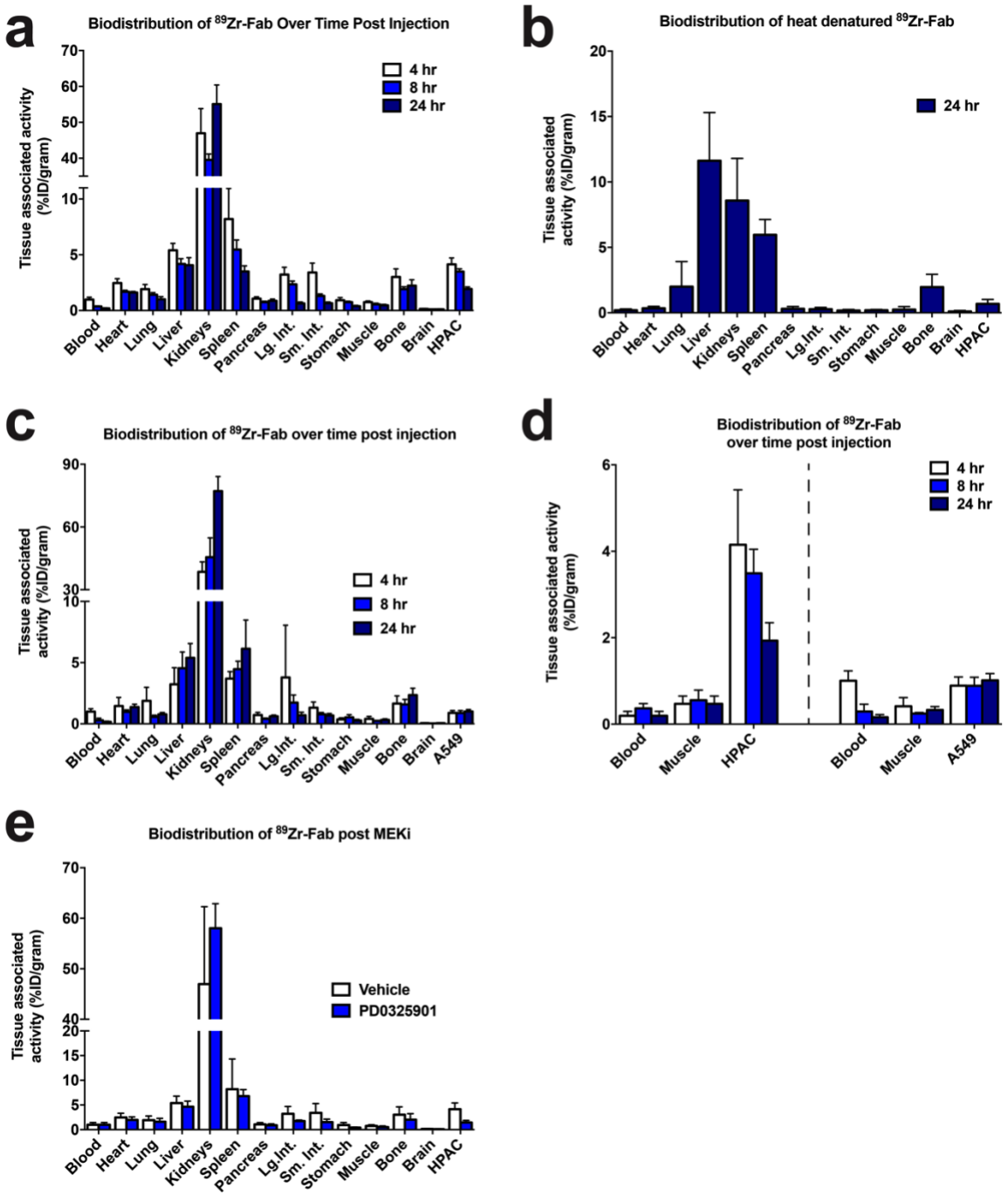

Figure 1-11. CDCP1 expression is coupled to MAPK signaling in mice. (a) Quantification of the bio-distribution of the CDCP1 ^{89}Zr-Fab in HPAC tumor bearing nu/nu mice (n=5 per treatment arm) 4 hours (White), 8 hours (Light Blue), and 24 hours (Dark Blue) post injection. **(b)** Quantification of the bio-distribution of heat denatured CDCP1 ^{89}Zr-Fab in HPAC tumor bearing nu/nu mice (n=5 per treatment arm) 24 hours post injection. **(c)** Quantification of the bio-distribution of the CDCP1 ^{89}Zr-Fab in A549 tumor

bearing nu/nu mice (n=5 per treatment arm) 4 hours (White), 8 hours (Light Blue), and 24 hours (Dark Blue) post injection. **(d)** Quantification of tumor specific bio-distribution of the CDCP1 ^{89}Zr-Fab in HPAC (Left) and A549 (Right) tumor bearing nu/nu mice (n=5 per treatment arm) 4 hours (White), 8 hours (Light Blue), and 24 hours (Dark Blue) post injection. Only HPAC xenograft mice showed tumor localization of the ^{89}Zr-Fab, consistent with the difference in CDCP1 expression level between HPAC (~2.9M copies/cell) and A549 (~0.06M copies/cell) cells. **(e)** Quantification of the bio-distribution of the CDCP1 ^{89}Zr-Fab 4 hours post injection in HPAC tumor bearing nu/nu mice (n=5 per treatment arm) treated with vehicle (White) or MEKi (Dark Blue).

Discussion:

Exploiting an unbiased approach of globally and quantitatively profiling the oncogenic RAS surfaceome that relies on MS-based proteomics and CRISPRi targeted screening, we begin to demonstrate the logic of how constitutive RAS activation influences the expression and function of membrane proteins to exert oncogenic phenotypes. Our results suggest that RAS signaling can coordinately regulate a network of surface proteins in order to drive malignant hallmarks such as loss of adhesion, cell migration, and cell growth. Specifically, our work reveals that proteins involved in integrin signaling are enriched both in terms of function and expression level at the RAS cell surface. For example, we observed that cells with oncogenic KRAS display high expression levels of several integrins (ITGB5/ITGB1/ITGA5/ITGA3) in combination with CDCP1. Previous work has identified a signaling axis through which CDCP1/integrin complexes can drive AKT dependent loss of adhesion, cell growth, and anti-anoikis signaling [9]. Importantly, we found that knockdown of CDCP1 or ITGB5 slows the growth of cells addicted to RAS signaling, supporting the idea that oncogenic RAS promotes the expression of these proteins to enable tumor cell growth. This also suggests that the invasive potential and propensity for metastasis of RAS driven cancers may partially be a consequence of these differentially expressed proteins working in concert. Furthermore, the evidence for this signaling axis is found in the TCGA for pancreatic cancer, where CDCP1 and all four identified integrins show significantly elevated mRNA levels in cancers with RAS mutations.

Activation of RAS can lead to signaling through more than half a dozen effector pathways; however, our work suggests that the MAPK pathway is most important for regulating the surface proteome. Nearly half of the proteins we observed to be enriched on the surface of KRAS transformed MCF10As were decreased in expression level when cells were treated with a MEK inhibitor. Conversely, treatment with EGF and AKT inhibition had little consequence on this set of RAS enriched membrane proteins. Consistent with this observation, we found the same cells were sensitive to knockdown of proteins in the MAPK pathway, but insensitive to CRISPRi knockdown of proteins involved in PI3K signaling. We used CDCP1 as an example to validate that these observations extend beyond MCF10As to patient derived cancer cell lines and even to xenograft mouse models for PDAC. These data provide mechanistic insight from the perspective of cell surface proteins to support previous reports that the MAPK pathway is the most potent of the RAS effector pathways in mediating transcriptional reprogramming and oncogenesis. Furthermore, our data suggest that a subset of these proteins could serve as new biomarkers for both RAS dependent MAPK signaling and drug efficacy of MAPK pathway inhibitors.

Our follow up investigation of CDCP1 exemplifies the utility of our technological pipeline, validates our approach of studying RAS signaling in a simple isogenic MCF10A model, and most importantly, provides a validated example of a cell surface marker for oncogenic RAS signaling in multiple cancer types. Our initial observation that CDCP1 expression was driven by RAS dependent MAPK signaling in MCF10As was recapitulated in more than a dozen mutant RAS cancer cell lines as well as an *in vivo* model for

pancreatic cancer. While previous work has suggested a connection between RAS signaling and CDCP1 in lung cancers [37], our work now demonstrates MAPK signaling dependent expression of this protein in multiple epithelial-derived RAS driven malignancies as well as *in vivo*. Additionally, we show that CDCP1 is important for proliferation in RAS addicted cells, suggesting a significant link between its function and its upregulated surface expression. Here we applied our novel antibodies to CDCP1 to begin to validate its potential as a therapeutic target and as a biomarker in RAS driven cancers dependent on MAPK signaling.

More preclinical studies beyond the scope of this work are necessary to fully validate CDCP1 as a therapeutic target. Nonetheless, we saw tumor localization of our CDCP1 antibodies in *in vivo* xenograft models for PDAC, and MEK-dependent expression providing mechanistic validation *in vivo*. This mouse experiment does not provide a fair assessment of tumor selective expression of CDCP1, as our antibody did not show cross reactivity with the mouse homolog of CDCP1 (data not shown). However, analysis of the GTEX tissue expression database reveals that CDCP1 normal tissue expression is quite restricted (**Figure 1-9B**). In comparison to the classical antibody targeted cell-surface protein, HER2, normal tissue expression for CDCP1 is far lower (**Figure 1-9C**). Additionally, we showed that mutant RAS PDAC cells express nearly 3 million copies per cell, a number comparable to the estimated 2 million copies per cell that can be observed in HER positive breast cancers. More extensive expression profiling of human tissues is needed to truly estimate the therapeutic potential of this protein. However, we believe that

the observations described herein provide motivation for the further exploration of CDCP1 an antibody target for RAS mutant cancers.

In summary, the results described herein validate and provide a mechanistic basis for the hypothesis that RAS signaling can meaningfully remodel the surface proteome to support malignant phenotypes. The strength of our linked target discovery and antibody generation pipeline was exemplified in the engineering of recombinant antibodies to CDCP1, and in demonstrating that these antibodies can be used to selectively deliver therapeutic payloads to RAS transformed cells and report *in vivo* on RAS signaling status. Overall, this work presents a novel technological pipeline for the systematic discovery and generation of antibodies to surface markers coordinately regulated by oncogene signaling pathways. Ultimately, we hope this pipeline can be applied towards the discovery of therapeutic antibodies to target previously "undruggable" oncogenes, including RAS, from the outside.

Acknowledgments

We thank E. Scott Seeley, Martin McMahon, Charles Craik, Frank McCormick, Brian Lee, Tet Matsuguchi, Jia Liu, Karolina Wypisniak, Michael Hornsby, Jacqueline Villalta, Yun Mou, James Koerber, and Victoria Assimon for helpful discussions and technical advice. We thank Sachdev Sidhu (University of Toronto) for providing the phage-displayed Fab library. We thank Sourav Bandyopadhyay (UCSF) and Maggie Martins (UCSF) for generating and providing the MCF10A empty vector and $KRAS^{G12V}$ cell lines. We thank

Frank McCormick and Jacqeline Galeas for providing the SW620, SW403, SW1116, and CAPAN-1 cell lines. We thank E. Scott Seeley (Salvo LLC) for providing the Panc1, 3XPC3, CAPAN-2, PL5, H5667, HPAC, and HPNE cell lines. We thank Kevan Shokat for providing the H1792, H358, and H1299 cell lines. We thank Arthur Weiss (UCSF) and Theresa Kadlecek (UCSF) for providing the NFAT-dependent GFP reporter Jurkat cell line. Funding was provided by R01 grants from the NIH (CA191018 and GM097316). A.J.M. was supported by a predoctoral fellowship from the NSF GRFP.

Materials and Methods

Cell surface protein enrichment

For all stable isotope labeling with amino acids in cell culture (SILAC) experiments, cells were cultured in DMEM SILAC media (Thermo) containing L-[$^{13}C_6$,$^{15}N_2$]lysine and L-[$^{13}C_6$,$^{15}N_4$] arginine (heavy label) (CIL) or L-[$^{12}C_6$,$^{14}N_2$]lysine and L-[$^{12}C_6$,$^{14}N_4$]arginine (light label) for 7 doublings to ensure full incorporation of the isotopic labels. In the KRAS isogenic study, MCF10A cells expressing KRAS^{G12V} were heavy labeled while the MCF10A cells harboring empty vector were light labeled. In all drug treatment experiments, light labeled cells were treated with DMSO while the heavy labeled cells were treated with 100 nM PD0325901, 2μM MK-2206 (Selleck), or 500nM Gefitinib (LC Laboratories). After 72 hours of drug treatment, cells were lifted with Versene (0.04% EDTA, PBS pH 7.4 Mg/Ca free) and 7-12M cells from both the heavy and light labeled cultures were mixed at a 1:1 cell count ratio for cell surface capture and enrichment (Wollscheid). Briefly, live cells were treated with sodium periodate buffer (2 mM $NaPO_4$,

PBS pH 6.5) at 4 °C for 20 minutes to oxidize vicinal diols on the glycans of surface glycoproteins. Aldehydes generated by oxidation were then covalently labeled with biocytin hydrazide in a labeling buffer (PBS pH 6.5 + 1 mM biocytin hydrazide (Biotium) + 10 mM aniline (Sigma)) for 90 minutes at 4 ˚C. Cells were then washed four times with PBS pH 6.5 to remove excess biocytin-hydrazide and stored overnight at -80 ˚C.

Frozen cell pellets were thawed and lysed in RIPA buffer (VWR) containing 1X Protease Inhibitor Cocktail (Sigma) at 4 °C for 30 minutes. Cell lysates were sonicated, clarified, and subsequently incubated with 500 µl of NeutrAvidin Agarose (Thermo) slurry at 4 °C for 30 minutes. The NeutrAvidin beads were then extensively washed with RIPA buffer, high salt buffer (1M NaCl, PBS pH 7.5), and urea buffer (2M urea, 50mM ammonium bicarbonate). Samples were reduced on-bead with 5 mM TCEP at 55°C for 30 minutes and alkylated with 10 mM iodoacetamide at room temperature for 30 minutes. To release bound proteins, proteins were subjected to on-bead digestion using 20 µg sequencing grade trypsin (Promega) at room temperature overnight. After overnight digestion, the beads were extensively washed with RIPA buffer, high salt buffer (1M NaCl, PBS pH 7.5), and urea buffer (2M urea, 50mM ammonium bicarbonate). To release the remaining trypsin digested N-glycosylated peptides from the neutravidin beads, a second on-bead digestion was performed using 2500U of PNGase F (NEB) at 37 °C overnight. The eluted fraction was collected using a spin column and then desalted using ZipTips with 0.6 µL C_{18} resin (Millipore Sigma) following standard protocol. Desalted peptides were dried and dissolved in mass spectrometry buffer (0.1% formic acid + 2% acetonitrile) prior to LC-MS/MS analysis.

Mass spectrometry analysis

1 µg of peptide was injected into a pre-packed 0.075mm x 150mm Acclaim Pepmap C18 LC column (2 µm pore size, Thermo Fisher) attached to a Q Exactive Plus (Thermo Fisher) mass spectrometer. Peptides were separated using a linear gradient of 3-35% solvent B (Solvent A: 0.1% formic acid, Solvent B: 80% acetonitrile, 0.1% formic acid) over 120 minutes at 300 µl/min. Data was collected in data-dependent acquisition mode using a top 20 method with a dynamic exclusion of 35 s and a charge exclusion restricted to charges of 2, 3, or 4. Full (MS1) scan spectrums were collected as profile data with a resolution of 140,000 (at 200 *m*/*z*), AGC target of 3E6, maximum injection time of 120 ms, and scan range of 400-1800 *m*/*z*. Fragment ion (MS2) scans were collected as centroid data with a resolution of 17,500 (at 200 *m*/*z*), AGC target of 5E4, maximum injection time of 60 ms with a normalized collision energy at 27, and an isolation window of 1.5 *m*/*z* with an isolation offset of 0.5 *m*/*z*.

Proteomics data analysis

Peptide search and MS1 peak area quantification was performed using ProteinProspector (v.5.13.2) against 20203 human proteins (Swiss-prot database, obtained March 5, 2015) with a false discovery rate of 1%.

Quantitative data analysis was performed using a customized pipeline developed using R (programming language) in RStudio. To ensure stringent quantification of the surface

proteome, several filters were applied to eliminate peptide identifications that we believe are due to contamination in the enrichment protocol. Only those peptides containing a PNGase F generated Asn to Asp post-translational modification were considered in the analysis, and proteins with only one quantified peptide were triaged. Proteins not included in a manually curated list of surfaceome proteins (5973 proteins) were also excluded. SILAC ratios were manually calculated from MS1 peak areas and then converted to $\log_2$ ratios normalized to a mean $\log_2$ SILAC ratio = 0 for each dataset. Median log2 SILAC ratios were calculate for each protein and p-values were calculated by a Mann-Whitney test assuming a null hypothesis of $\log_2$(SILAC Ratio) = 0.

GO Analysis

Gene sets enriched among proteomic hit genes (p-value < 0.01 and absolute $\log_2$ FC > 1.75) were determined using David (Huang and Lempicki) using the Homo sapiens gene list as background.

RNAseq

Total RNA was extracted using the Quiagen RNAeasy kit and RNA amplified using the TruSeq Stranded RNA library creation kit (Illumina) and sequenced to a depth of >20M reads per sample in duplicate. FPKM and fold changes were determined using cufflinks and tophat using hg19 gene annotations.

Vector design and construction

The vector used to express cell-surface protein ECDs **(Figure 2A)** was generated by Gibson cloning and adapted from the commercially available pFUSE-hIgG1-Fc (InvivoGen) vector. Each ECD was subcloned between an N-terminal IL2 Signal Sequence and a C-terminal TEV cleavage site. BirA was subcloned into a pLX302 lentiviral vector with a C-terminal KDEL ER localization tag.

We used a previously described vector for expression of Fabs [32]. The pFUSE-hIgG1-Fc (InvivoGen) vector was used for expression of IgGs wherein the heavy chain was genetically fused to the hIgG1-Fc and the light chain was expressed on a separate copy of the vector with a C-terminal FLAG tag. The pFUSE-hIgG1-Fc (InvivoGen) vector was also used for expression of the αCD19- αCDCP1. The αCD19 was C-terminally fused to the light chain of the αCDCP1 Fab and the heavy chain was expressed on a separate copy of the vector.

Previously described vectors were used for CRISPRi experiments. Individual sgRNAs were cloned into a pU6 lentiviral vector (Adgene: 46914), dCas9-BFP-KRAB was expressed from a pHR-SFFV lentiviral vector (Adgene: 46911), and the sgRNA library was cloned into a pSICO lentiviral vector (Adgene: 84832).

Expression of Fc-fusion antigens

HEK293T cells stably expressing ER-localized BirA were grown to ~80% confluency and transiently transfected with 60µg of ECD-Fc plasmid using 200µg Linear Poly(ethyleneimine) 25,000 Da (Polysciences). After 6 hours, media was replaced with

DMEM supplemented with 10% Ultra Low IgG FBS (Thermo Fisher), 50 µM biotin, and 1X Pen/Strep. Media was harvested every 3 days for 6 days and protein was purified by Protein A affinity chromatography and assessed for quality, biotinylation, and integrity by SDS-PAGE.

Phage display selections

All phage selections were done according to previously established protocols. Briefly, selections with antibody phage Library F [33] were performed using biotinylated Fc-fusion antigens captured with streptavidin-coated magnetic beads (Promega). Prior to each selection, the phage pool was incubated with 1 µM of biotinylated Fc-domain immobilized on streptavidin beads in order to deplete the library of any binders to the beads or Fc-tag. In total, four rounds of selection were performed with decreasing amounts of ECD-Fc-fusion antigens (100 nM, 50 nM, 10 nM and 10 nM). To reduce the deleterious effects of nonspecific binding phage, we employed a “catch and release” strategy, where ECD-Fc-fusion binding Fab-phage were selectively eluted from the magnetic beads by the addition of 2 µg/mL TEV protease. Individual phage clones from the fourth round of selection were analyzed for binding by ELISA.

Phage ELISAs

ELISAs were performed according to standard protocols. Briefly, 96-well Maxisorp plates were coated with NeutrAvidin (10 µg/ml) overnight at 4 °C and subsequently blocked with BSA (2% w/v) for 1 h at 20 ˚C. 20 nM of biotinylated ECD-Fc-fusion or Fc-domain was captured on the NeutrAvidin-coated wells for 30 minutes followed by the addition phage

supernatents diluted 1:5 in ELISA buffer (PBS, pH 7.4, 0.05% Tween-20, 0.2% BSA) for 30 minutes. The bound phage were then detected using a horseradish peroxidase (HRP)-conjugated anti-phage monoclonal antibody (GE Lifesciences 27-9421-01).

Expression of Fabs

Fabs were expressed according to a previously described protocol. Briefly, C43 (DE3) Pro+ *E. coli* containing expression plasmids were grown in TB at 37 ˚C to an OD_{600} of 0.6–0.8 and then Fab expression was induced by the addition of 1 mM IPTG. Incubation temperature was subsequently reduced to 30 ˚C and the cultures were allowed to shake for 16-18 h. Cells were harvested by centrifugation and Fabs were purified by Protein A affinity chromatography. Fab purity and integrity was assessed by SDS-PAGE and intact protein mass spectrometry using a Xevo G2-XS Mass Spectrometer (Waters).

Flow Cytometry

Cells were lifted with Versene (0.04% EDTA, PBS pH 7.4 Mg/Ca free), washed once with PBS pH 7.4, and subsequently blocked with flow cytometry buffer (PBS, pH 7.4, 3% BSA). Fabs (10 µg/mL) or commercial antibodies were added to cells for 30 minutes at room temperature. Antibodies were detected with addition of Protein A – Alexafluor-647 conjugate (Life Technologies ; 1:1000). Cells were extensively washed and fluorescence was quantified using a FACSCanto II (BD Biosciences). All flow cytometry data analysis was performed using FlowJo software and plots were generated using Prism software (GraphPad).

Immunofluorescence

MCF10A KRAS and empty vector cells were plated on glass bottom imaging plates (MatTek) and allowed to incubate for 24 hours at 37 ˚C under 5% CO_2. Cells were fixed with 1% paraformaldehyde for 10 minutes, followed by addition of Fabs (10µg/mL) in imaging buffer (PBS, pH 7.4, 3% BSA) for 30 minutes. Fab binding was detected by the addition of a Protein A – Alexafluor-546 conjugate (Life Technologies ; 1:1000) in imaging buffer containing Hoescht blue (2µg/mL). Cells were imaged on a Zeiss Observer Z1 microscope using oil immersion. All immunofluorescence figures were generated using unbiased post-processing in Photoshop (Adobe).

Surfaceome sgRNA library specifications

Surfaceome genes were selected as a subset of the UniProt Human Proteome (19,942 genes). Genes were filtered based on UniProt subcellular location annotation to remove those proteins not annotated as localized to the “Cell Membrane” (2,015 genes), “Membrane” (2,162 genes), or “Extracellular Space” (280 genes). The gene list was further filtered to remove those genes not predicted by UniProt to contain a signal sequence (1605 genes). Finally, a set of RAS pathway genes (21 genes) was added (1626 genes). sgRNAs were designed using a previously described algorithm (Horlbeck and Weissman) and were synthesized in batch by Agilent. 150 non-targeting sgRNAs were included as negative controls.

CRISPRi library cloning

CRISPRi library sgRNA sequences were designed using previously described methods [38 50].Oligonucleotide pools were synthesized by Agilent. Each library was amplified by PCR, digested with BstXI and BlpI, and cloned into an sgRNA expression vector.

Preperation of CRISPRi lentiviral library

To produce virus, HEK293T cells were transfected with a mixture of library plasmid DNA and second-generation lentiviral packaging plasmids at ~80% confluence. Transfection of the plasmids was performed using TransIT-LTI Transfection Reagent (Mirus, MIR 2306). Media was changed to complete DMEM after 6 hours of incubation with transfection mixture. The supernatant was harvested and cleared by passing through a 0.45 µm PVDF filter 72 hours post transfection and immediately used for infection.

CRISPRi screen

CRISPRi MCF10A cell lines were infected with the surfaceome sgRNA library as previously described [38 39]. The infection was scaled to achieve a multiplicity of infection of less than one sgRNA per cell. Two days after infection, cells were treated with 2 µg/ml puromycin (Sigma Aldrich) for 72 hours to select for sgRNA expression, and then grown in fresh medium without puromycin for 48 hours recovery. MCF10A empty vector cells were grown in standard MCF10A medium whereas the MCF10A $KRAS^{G12V}$ cells were either grown in standard MCF10A medium or MCF10A medium lacking Insulin and Epidermal Growth Factor (EGF). Cells were grown for 12 days, and at least 10 population doublings. Cells were maintained at a confluency between 20-80%, and at numbers continually maintaining a library coverage of at least 1,000 cells per sgRNA. Populations

of cells expressing this library of sgRNAs were harvested at the outset of the experiment (T0) and after 12 days (T12). Genomic DNA was harvested from all samples; the sgRNA-encoding regions were then amplified by PCR and sequenced on an Illumina HiSeq-2500 using custom primers with previously described protocols at high coverage [35]. Two biological replicates of each screening condition were performed. From this data, we quantified the frequencies of cells expressing different sgRNAs in each sample and quantified the phenotype of each sgRNA as the average phenotype of the 3 strongest sgRNAs.

Assessment of CRISPRi phenotypes for individual sgRNAs

Individual phenotype validation experiments for sgRNAs from the CRISPRi screens, were performed as competitive growth experiments with a mixed culture of sgRNA-GFP infected and non-infected cell populations of MCF10A empty vector and $KRAS^{G12V}$. Following infection, cells were selected in puromycin (2 µg/mL) for 3 days and then allowed to recover for 2 days. Infected and non-infected cells were counted and seeded at a 1:1 ratio in 96 well plates. In parallel, infected cells were grown in mono-culture so that sgRNA expression could be monitored. Triplicate samples for each sgRNA were grown under standard conditions for the MCF10A empty vector, or with media lacking insulin and EGF for the MCF10A $KRAS^{G12V}$. All cells grown in mono-culture were grown under standard conditions. The percentage of cells expressing GFP (indicating sgRNA expression) was measured at several time points (0 days, 5 days, 12 days). The relative fraction of sgRNA positive cells was determined by the percentage of cells that

maintained expression of GFP (indicating sgRNA expression) normalized to the percentage of GFP positive cells on the day of doxycycline addition (day 0).

Expression of BiTE and IgG

Expi293 (Life Technologies) cells were transiently co-transfected with two pFUSE (InvivoGen) vectors harboring either the Fab heavy chain and the Fab light chain genetically fused to the αCD19 scFv, or the Fab heavy chain fused to a human Fc and the Fab light chain, at a ratio of 1:1 for BiTE and IgG respectfully. The ExpiFectamine 293 transfection kit (Life Technologies) was used for transfections as per manufacturer's instructions. Cells were incubated for 7 days at 37 ˚C in a 5% CO_2 environment before the supernatants were harvested by centrifugation. Protein was purified by Protein A affinity chromatography and assessed for quality and integrity by SDS-PAGE.

Antibody drug conjugate cell killing assay

Antibody drug conjugate cell killing assays were performed using a Fab Anti-Human IgG Fc-MMAF Antibody with Cleavable Linker (Moradec) following manufacture's protocol. Briefly, 5000 HPAC or HPNE cells were plated in each well of a 96-well plate, and IgG (4 nM initial, 5-fold serial-dilutions, 6 times) or Staurosporine (2μM) was added. After 10-minute incubation, 40 nM of the Fab Anti-Human IgG Fc-MMAF Antibody with Cleavable Linker was added to a final volume of 100μL. Cells were then allowed to incubate for 72 hours at 37 ˚C under 5% CO_2. After the incubation period, 70 μL of CellTiter-Glo Reagent (Promega) was added to each well followed by shaking incubation at room temperature

for 10 minutes. Luminescence was then quantified using an Infinite M200 PRO plate reader (Tecan).

BiTE Assay

Jurkat NFAT-reporter cells were mixed with HPAC or HPNE target cells at a ratio of 1:1. Bispecic T-cell engaging antibody (BiTEs) (anti-CDCP1-antiCD19) or Fab (anti-CDCP1) was diluted in media and added to cell mixtures at a final concentration of 1nM. After 20 hour incubation at 37 ˚C, cells were pelleted by centrifugation. NFAT-dependent GFP reporter expression was quantified by flow cytometry using a FACSCanto II (BD Biosciences).

Immunoblotting

Cells were plated at approximately 0.5×10^6 cells/well in a 6-well plate and cultured overnight before drug treatment. Media was replaced with media supplemented with Gefitinib (2 µM), SB590885 (2 µM), PD0325901 (2 µM), XL147 (2 µM), MK2206 (2 µM), or Vehicle (0.2% DMSO). The cells were further incubated at 37 ˚C for 48 h, after which the cells were washed with PBS and lysed with RIPA Lysis and Extraction Buffer (Thermo Scientific) supplemented 1X Protease Inhibitor Cocktail (Sigma) at 4 ˚C for 30 minutes. Immunoblotting was performed using AKT(pan) (Cell Signaling mouse mAB, #2920), Phospho-AKT (Thr308) (Cell Signaling rabbit mAB, #2965), p44/42 MAPK (Erk1/2) (Cell Signaling rabbit mAB, #4695), Phospho-p44/42 MAPK (Erk1/2) (Thr202/Tyr204) (Cell Signaling rabbit mAB, #4370), CDCP1 (Cell Signaling rabbit mAB, #13794), Tubulin

(Sigma mouse mAB #T6199), IRDye® 680RD Goat anti-Mouse (Licor # 925-68070), and IRDye® 800CW Donkey anti-Rabbit (Licor # 925-32213) antibodies.

Coupling of the desferrioxamine chelate on the antibody (Fab)

110 µL of Fab (anti-CDCP1) at a concentration of 4.2 mg/mL was dispersed in 100 µL of 0.1 M sodium bicarbonate buffer (pH 9.0). The pH was adjusted to 9.0 and the final reaction mixture was adjusted to a total volume of 0.5 mL by adding a sufficient amount of 0.1 M sodium bicarbonate buffer. Df-Bz-NCS (p-isothiocyanatobenzyl-desferrioxamine) was dissolved in DMSO at a concentration of 10 mM. Df-Bz-NCS solution was added to the antibody solution to give a 3 molar excess of the chelator over the molar amount of Fab. The Df-Bz-NCS was added in steps of 2 µL and mix rigorously during the addition. The concentration of DMSO was kept below 2% of the total reaction mixture in order to avoid any precipitation. After 30 min at 37 ^{o}C, the reaction mixture was purified via a PD-10 column pre equilibrated by 20 mL of gentisic acid solution (5 mg/mL of gentisic acid in 0.25 M sodium acetate (pH 5.4-5.6)). The Fab-DFO solution was eluated in gentisic acid solution, and the pH was adjusted to 7 by addition of NaOH (1 M). Then the solution was aliquoted and stored at -20 ^{o}C until the day of radiolabeling.

^{89}Zr Radiochemistry

[^{89}Zr]Zr-oxalic acid solution (5mCi; 10 µl) was neutralized with 2 M Na_2CO_3 (5 µL). After 3 min, 0.30 mL of 0.5 M HEPES (pH 7.1–7.3) and 0.5 mg of DFO-Fab (pH 7) were added into the reaction vial. After incubation (120 minutes) at 37 ^{o}C, the radiolabeling efficiency

was determined by ITLC using chromatography strips and 20 mM citric acid (pH 4.9–5.1). The radiolabeling efficiency was consistently >98.5%.

^{125}I Radiochemistry

Iodination with iodine-125 was done in pre-coated iodination tubes (Pierce). 100 µg of anti-CDCP1 Fab was dispersed in 100 µL of PBS solution and added to the pre-coated iodination tubes. Separately in a 1.5 mL eppendorf tube, 1 µL of HCl (0.2 M), 2.5 µL of phosphate buffer (0.5 M, pH = 8), 10 µL of potassium iodide solution (1 mg/ml) was prepared. 1 mCi of iodine-125 was added into the tubes and the previous solution was then mixed in the iodination tubes. After 15 min of reaction the solution was purified via PD10 column pre equilibrated with 20 mL of PBS solution. The purity was assessed via iTLC, and ^{125}I-FAB was consistently >98% pure.

Cell Culture

The MCF10A cells were maintained in DMEM medium, supplemented with 5% Horse Serum (Invitrogen), 20 ng/mL EGF (Invitrogen), 500 ng/mL Hydrocortisone (Sigma), 100 ng/mL Cholera Toxin (Sigma), 10 µg/mL Insulin (Sigma), and 1X Pen/Strep. The SW620, SW403, SW1116, and CAPAN-1 cell lines were a gift form the laboratory of Frank McCormick and were maintained in McCoy's 5A medium, supplemented with 10% FBS and 1X Pen/Strep. The Panc1, BXPC3, CAPAN-2, PL5, H5667, HPAC, MiaPaCa-2, and HPNE cells were a gift from the laboratory of E. Scott Seeley and were maintained in IMDM supplemented with 10% FBS and 1X Pen/Strep. The H1792, H358, and H1299 cells were a gift from the laboratory of Kevan Shokat and were maintained in RPMI

supplemented with 10% FBS and 1X Pen/Strep. The HEK293T cell lines were cultured in DMEM supplemented with 10% FBS and 1X Pen/Strep. Jurkat NFAT reporter cells lines were cultured in RPMI supplemented with 10% FBS, 2 mg/mL G418 (Thermo) and 1X Pen/Strep. Cell line identities were authenticated by morphological inspection. Symptoms for mycoplasma contamination were not observed and thus no test for mycoplasma contamination was performed. To the best of our knowledge, all cell lines that were received as gifts were previously authenticated and tested for mycoplasma.

To construct the CRISPRi cell lines, MCF10A empty vector and $KRAS^{G12V}$ cells were lentivirally transduced with constructs encoding dCas9-BFP-KRAB. Three rounds of sorting for stable BFP expression by flow cytometry using a BD FACS Aria2 were used to generate homogeneous polyclonal populations of each CRISPRi cell line. A second round of lentiviral transduction was used to introduce expression of sgRNAs. Cells expressing sgRNAs were selected for in puromycin (2 µg/mL) and validated by confirming either GFP (single sgRNA) or BFP (sgRNA library) expression using fluorescence microscopy or flow cytometry.

To construct the ECD displaying HEK293 cell lines, Flp-In T-REx (ThermoFisher) cells were co-transfected with the pOG44 vector (ThermoFisher) and a construct encoding each ECD fused to the transmembrane anchoring domain of Platlet Derived Growth Factor with a YPET tag in the pcDNA5/FRT Mammalian Expression vector (ThermoFisher). Cells displaying each ECD were selected for in DMEM supplemented

with 10% FBS and 50 µg/mL Hygromycin (ThermoFisher). Surface display was confirmed by fluorescence microscopy detection of the YPET tag.

Saturation binding assay

The number of receptors per cell was determined by a saturation binding experiment performed in A549, SW62D, MiaPAca2, and HPAC cells using ^{125}I-CDCP1 Fab. 60,000 cells were plated into wells of 12 well plates. The saturation binding assays were done in a range of 9 different concentrations between 0.65 to 80 nM of ^{125}I-CDCP1 Fab in each well. The non-specific binding was determined at 3 different concentrations (0.65, 20 and 80 nM) by co-incubation of cells with 1000 fold excess over the Kd of the unlabeled anti-CDCP1 Fab. Following incubation for 1 hour, the cells were washed twice with ice cold PBS and retained for analysis (unbound fraction). The cells were lysed with 1 mL of 1M NaOH and collected (cell associated fraction). The unbound and cell associated fractions were counted in a gamma counter and expressed as a percentage of the total activity added per number of cells. Experiments were performed in triplicate. The specific binding was obtained by subtracting the non-specific binding from the total binding. A Rosenthal plot was used to determine the Bmax.

Immunoreactivity fraction

The immunoreactive fraction was determined by measuring the percentage of radiolabeled Fab bound to antigen under conditions of antigen excess. Using a concentrated cell suspension of HPAC cell lines, 5 different dilutions of cells ranging from 0.5 to 10 million cells/mL were prepared in PBS solution containing BSA. For each cell

concentration, ^{89}Zr-DFO-CDCP1 (10 µCi) was incubated for 1 hour at room temperature. Following the incubation, the cell suspensions were washed twice with ice-cold PBS and centrifuged. The unbound radioactivity was removed and counted along with the cell-bound activity. The inverse of cell-bound radioactivity (total over bound) was plotted against the inverse of cell concentration. The data was fitted with a least squares linear regression method (PRISM). The Y-intercept of the regression line represents the inverse of the immunoreactive fraction.

In vivo imaging

Three to five week old male nu/nu immunocompromised mice were purchased from Charles River. Nu/Nu mice were inoculated with $1x10^6$ HPAC or A549 cells subcutaneously into one flank in a 1:1 mixture (v/v) of PBS and Matrigel (Corning). Tumors were palpable within 21-30 days with HPAC and 14-21 days with A549 after injection. Tumor bearing mice (n=5 per treatment arm) received between 50 to 300 µCi of ^{89}Zr-CDCP1 or ^{89}Zr-heat denatured Fab solution in 100 µL saline solution volume intravenously using a custom mouse tail vein catheter with a 28-gauge needle and a 100-150 mm long polyethylene microtubing. ~300 µCi was injected for the mice for imaging and ~ 50 µCi for the mice for biodistribution. The mice were imaged at different time points (4h, 8h, 24h) on a dedicated small animal PET/CT scanner (Inveon, Siemens Healthcare, Malvern, PA). Animals were scanned for 20 minutes for PET, and the CT acquisition was 10 minutes. The coregistration between PET and CT images was obtained using the rigid transformation matrix from the manufacturer-provided scanner calibration procedure since the geometry between PET and CT remained constant for each of PET/CT scans

using the combined PET/CT scanner. Animals were anesthetized with gas isoflurane at 2% concentration mixed with medical grade oxygen. The photon attenuation correction was performed for PET reconstruction using the coregistered CT-based attenuation map to ensure the quantitative accuracy of the reconstructed PET data.

Drug treatment for *in vivo* experiments

Tumor bearing mice were treated with MEK inhibitor (PD0325901). PD0325901 (Sigma) was suspended in HPMT solution (0.5% w/v hydroxypropyl-methylcellulose dissolved in water plus 0.2% v/v Tween 80). Tumor bearing mice were treated once daily via oral gavage with PD0325901 (25 mg/kg/d) for 6 days (4 days before the injection and 2 days following the radiotracer injection).

Biodistribution studies

Biodistribution studies were conducted to evaluate the uptake of ^{89}Zr-CDCP1 in mice bearing subcutaneous tumors. At a dedicated time after radiotracer injection, animals were euthanized by CO_2(g) asphyxiation, and 14 tissues (including the tumor) were removed, weighed and counted on a gamma-counter for accumulation of ^{89}Zr-radioactivity. The mass of ^{89}Zr-CDCP1 formulation injected into each animal was measured and used to determine the total number of counts (counts per minute, [c.p.m.]) by comparison to a standard syringe of known activity and mass. Count data was background- and decay-corrected and the tissue uptake measured in units of percentage-injected dose per gram (%ID/g) was calculated by normalization to the total amount of activity injected.

References

1. Downward, J. Targeting RAS signalling pathways in cancer therapy. *Nat. Rev. Cancer* **3,** 11–22 (2003).
2. Pylayeva-Gupta, Y., Grabocka, E. & Bar-Sagi, D. RAS oncogenes: weaving a tumorigenic web. *Nat. Rev. Cancer* **11,** 761–774 (2011).
3. Hanahan, D. & Weinberg, R. A. Hallmarks of cancer: the next generation. *Cell* **144,** 646–674 (2011).
4. Roberts, P. J. & Der, C. J. Targeting the Raf-MEK-ERK mitogen-activated protein kinase cascade for the treatment of cancer. *Oncogene* **26,** 3291–3310 (2007).
5. Stephen, A. G., Esposito, D., Bagni, R. K. & McCormick, F. Dragging Ras Back in the Ring. *Cancer Cell* **25,** 272–281 (2014).
6. Ledford, H. Cancer: The Ras renaissance. *Nature News* **520,** 278–280 (2015).
7. Papke, B. & Der, C. J. Drugging RAS: Know the enemy. *Science* **355,** 1158–1163 (2017).
8. Soule, H. D. *et al.* Isolation and characterization of a spontaneously immortalized human breast epithelial cell line, MCF-10. *Cancer Res.* **50,** 6075–6086 (1990).
9. Casar, B. *et al.* In vivo cleaved CDCP1 promotes early tumor dissemination via complexing with activated β1 integrin and induction of FAK/PI3K/Akt motility signaling. - PubMed - NCBI. *Oncogene* **33,** 255–268 (2012).
10. Bhatt, A. S., Erdjument-Bromage, H., Tempst, P., Craik, C. S. & Moasser, M. M. Adhesion signaling by a novel mitotic substrate of src kinases. *Oncogene* **24,** 5333–5343 (2005).
11. Martins, M. M. *et al.* Linking Tumor Mutations to Drug Responses via a Quantitative Chemical–Genetic Interaction Map. *Cancer Discovery* **5,** 154–167 (2015).
12. Debnath, J., Muthuswamy, S. K. & Brugge, J. S. Morphogenesis and oncogenesis of MCF-10A mammary epithelial acini grown in three-dimensional basement membrane cultures. *Methods* **30,** 256–268 (2003).
13. Stolze, B., Reinhart, S., Bulllinger, L., Fröhling, S. & Scholl, C. Comparative analysis of KRAS codon 12, 13, 18, 61, and 117 mutations using human MCF10A isogenic cell lines. *Sci Rep* **5,** 8535 (2015).
14. Ye, X. *et al.* Comparative proteomics of a model MCF10A-KRasG12V cell line reveals a distinct molecular signature of the KRasG12V cell surface. *Oncotarget* **7,** 86948–86971 (2016).
15. Wollscheid, B. *et al.* Mass-spectrometric identification and relative quantification of N-linked cell surface glycoproteins. *Nat. Biotechnol.* **27,** 378–386 (2009).
16. Schiess, R. *et al.* Analysis of Cell Surface Proteome Changes via Label-free, Quantitative Mass Spectrometry. *Molecular & Cellular Proteomics* **8,** 624–638 (2009).
17. Ong, S.-E. & Mann, M. A practical recipe for stable isotope labeling by amino acids in cell culture (SILAC). *Nat Protoc* **1,** 2650–2660 (2006).
18. Barrett, S. D. *et al.* The discovery of the benzhydroxamate MEK inhibitors CI-1040 and PD 0325901. *Bioorg. Med. Chem. Lett.* **18,** 6501–6504 (2008).
19. Hirai, H. *et al.* MK-2206, an allosteric Akt inhibitor, enhances antitumor efficacy by standard chemotherapeutic agents or molecular targeted drugs in vitro and in vivo. *Molecular Cancer Therapeutics* **9,** 1956–1967 (2010).

20. Moasser, M. M., Basso, A., Averbuch, S. D. & Rosen, N. The tyrosine kinase inhibitor ZD1839 ('Iressa') inhibits HER2-driven signaling and suppresses the growth of HER2-overexpressing tumor cells. *Cancer Res.* **61,** 7184–7188 (2001).
21. Schwanhäusser, B. *et al.* Global quantification of mammalian gene expression control. *Nature* **473,** 337–342 (2011).
22. Lundberg, E. *et al.* Defining the transcriptome and proteome in three functionally different human cell lines. *Mol Syst Biol* **6,** (2010).
23. Wiita, A. P. *et al.* Global cellular response to chemotherapy-induced apoptosis. *eLife Sciences* **2,** e01236 (2013).
24. Baker, M. Reproducibility crisis: Blame it on the antibodies. *Nature* **521,** 274–276 (2015).
25. Huttenlocher, A. & Horwitz, A. R. Integrins in cell migration. *Cold Spring Harb Perspect Biol* **3,** a005074 (2011).
26. Kevil, C. G. *et al.* Intercellular adhesion molecule-1 (ICAM-1) regulates endothelial cell motility through a nitric oxide-dependent pathway. *J. Biol. Chem.* **279,** 19230–19238 (2004).
27. Antonioli, L., Yegutkin, G. G., Pacher, P., Blandizzi, C. & Haskó, G. Anti-CD73 in Cancer Immunotherapy: Awakening New Opportunities. *Trends in Cancer* **2,** 95–109 (2016).
28. Lukashev, M. *et al.* Targeting the Lymphotoxin- Receptor with Agonist Antibodies as a Potential Cancer Therapy. *Cancer Res.* **66,** 9617–9624 (2006).
29. Sun, X. *et al.* Role of decay-accelerating factor in regulating complement activation on the erythrocyte surface as revealed by gene targeting. *Proceedings of the National Academy of Sciences* **96,** 628–633 (1999).
30. Sørensen, K. D. *et al.* Prognostic significance of aberrantly silenced ANPEP expression in prostate cancer. *British Journal of Cancer* **108,** 420–428 (2013).
31. Czajkowsky, D. M., Hu, J., Shao, Z. & Pleass, R. J. Fc-fusion proteins: new developments and future perspectives. *EMBO Mol Med* **4,** 1015–1028 (2012).
32. Hornsby, M. *et al.* A High Through-put Platform for Recombinant Antibodies to Folded Proteins. *Mol. Cell Proteomics* **14,** 2833–2847 (2015).
33. Persson, H. *et al.* CDR-H3 diversity is not required for antigen recognition by synthetic antibodies. *J. Mol. Biol.* **425,** 803–811 (2013).
34. Uhlén, M. *et al.* A proposal for validation of antibodies. *Nat Meth* **13,** 823–827 (2016).
35. Gilbert, L. A. *et al.* CRISPR-mediated modular RNA-guided regulation of transcription in eukaryotes. *Cell* **154,** 442–451 (2013).
36. Iida, M. *et al.* Targeting AKT with the allosteric AKT inhibitor MK-2206 in non-small cell lung cancer cells with acquired resistance to cetuximab. *Cancer Biol. Ther.* **14,** 481–491 (2013).
37. Uekita, T. *et al.* Oncogenic Ras/ERK Signaling Activates CDCP1 to Promote Tumor Invasion and Metastasis. *Mol. Cancer Res.* **12,** 1449–1459 (2014).
38. Gilbert, L. A. *et al.* Genome-Scale CRISPR-Mediated Control of Gene Repression and Activation. *Cell* **159,** 647–661 (2014).
39. Kampmann, M., Bassik, M. C. & Weissman, J. S. Integrated platform for genome-wide screening and construction of high-density genetic interaction maps in mammalian cells. *Proceedings of the National Academy of Sciences* **110,** E2317–26 (2013).
40. Wang, M.-T. *et al.* K-Ras Promotes Tumorigenicity through Suppression of Non-canonical Wnt Signaling. *Cell* **163,** 1237–1251 (2015).

41. Leroy, C. *et al.* CUB-domain-containing protein 1 overexpression in solid cancers promotes cancer cell growth by activating Src family kinases. *Oncogene* **34,** 5593–5598 (2015).
42. Ikeda, J.-I. *et al.* Expression of CUB domain containing protein (CDCP1) is correlated with prognosis and survival of patients with adenocarcinoma of lung. *Cancer Sci.* **100,** 429–433 (2009).
43. Wright, H. J. *et al.* CDCP1 cleavage is necessary for homodimerization-induced migration of triple-negative breast cancer. *Oncogene* **35,** 4762–4772 (2016).
44. Eser, S., Schnieke, A., Schneider, G. & Saur, D. Oncogenic KRAS signalling in pancreatic cancer. *British Journal of Cancer* **111,** 817–822 (2014).
45. Bornstein, G. G. Antibody Drug Conjugates: Preclinical Considerations. *AAPS J* **17,** 525–534 (2015).
46. Commisso, C. *et al.* Macropinocytosis of protein is an amino acid supply route in Ras-transformed cells. *Nature* **497,** 633–637 (2013).
47. Wu, J., Fu, J., Zhang, M. & Liu, D. Blinatumomab: a bispecific T cell engager (BiTE) antibody against CD19/CD3 for refractory acute lymphoid leukemia. *J Hematol Oncol* **8,** 104 (2015).
48. Yuraszeck, T., Kasichayanula, S. & Benjamin, J. E. Translation and Clinical Development of Bispecific T-cell Engaging Antibodies for Cancer Treatment. *Clin. Pharmacol. Ther.* **101,** 634–645 (2017).
49. Singh, A. *et al.* A Gene Expression Signature Associated with 'K-Ras Addiction' Reveals Regulators of EMT and Tumor Cell Survival. *Cancer Cell* **15,** 489–500 (2009).
50. Horlbeck, M. A. *et al.* Compact and highly active next-generation libraries for CRISPR-mediated gene repression and activation. *eLife Sciences* **5,** (2016).

Chapter 2

Human Antibody-Based Chemically Induced Dimerizers for Cell Therapeutic Applications

*Zachary B Hill, *Alexander J Martinko, Duy P Nguyen & James A Wells

**Denotes equal contribution*

Abstract

Chemically induced dimerizers (CIDs) have emerged as one of the most powerful tools to artificially regulate signaling pathways in cells; however, currently available CID systems lack the properties desired for use in regulating cellular therapies. Here, we report the development of human antibody-based chemically induced dimerizers (AbCIDs) from known small-molecule-protein complexes by selecting for synthetic antibodies that recognize the chemical epitope created by the bound small molecule. We demonstrate this concept by generating three antibodies that are highly selective for the BCL-xL/ABT-737 complex over BCL-xL alone. We show the potential of AbCIDs to be applied to regulating human cell therapies by using them to induce CRISPRa-mediated gene expression and to regulate CAR T-cell activation. We believe that the AbCIDs generated in this study will find application in regulating cell therapies, and that the general method of AbCID development may lead to the creation of many new and orthogonal CIDs.

Introduction

Chemically induced dimerizers (CIDs) are powerful tools for dose and temporal control over protein-protein interactions.[1-3] CIDs have been utilized in a myriad of applications, including the development of artificial cellular circuits[4], activating split-enzyme activity[5, 6], and controlling protein localization. Recently, there has been a growing interest in utilizing CIDs to regulate the activity of cell therapies after they have been administered to a patient.[7, 8] Of particular interest has been the utilization of CIDs as safety switches for chimeric antigen receptor T-cell (CAR T-cell) therapies, where several patient deaths have occurred in clinical trials.[9] While a number of homo- and hetero-CIDs have been developed, they generally lack the properties required for use in human cell therapies.[1, 3, 10-16] For example, the classical FKBP/FRB CID system utilizes the small molecule rapamycin, which is both toxic and immunosuppressant. Orthogonal "rapalogs" show reduced toxicity, but have undesirable pharmacokinetic (PK) properties. Several plant-based CID systems have been developed, but the non-human nature of these proteins makes them prone to immunogenicity issues if incorporated into a cell therapy.[17] For the application of CIDs in cell therapies to reach its full potential, it is critical that new human-protein-based CIDs be developed that utilize small molecules with drug-like properties. Ideally, the small molecules should have favorable PK properties and be bioorthogonal or well-tolerated. Additionally, new CIDs should exhibit dose dependence and be easily incorporated into different cellular signaling pathways. To date, the vast majority of CID systems have been based on naturally occurring CIDs, and the ability to engineer in customized properties has been limited. While chemically linking two

pharmacophores together has been employed to rationally design heteromeric CIDs not found in nature, the resulting small molecules almost universally lack drug-like properties. For these reasons, a general method to design novel CIDs with desirable properties for use in regulating human cell therapies would be of great utility.

Here, we demonstrate a strategy to generate chemical-epitope-selective antibodies that has the potential to turn many known small-molecule-protein complexes into antibody-based chemically induced dimerizers (AbCIDs) (**Figure 2-1A**). We demonstrate this approach by engineering AbCIDs using the BCL-xL/ABT-737 complex. Furthermore, we show that AbCIDs can be used to regulate cellular processes; including CRISPRa mediated gene expression and CAR T-cell activation. We believe the broad applicability of this approach is the ability to rapidly generate CIDs from human protein-small-molecule complexes, with proteins and small molecules that meet the criteria for application in regulating human cell therapies.

Results

Identification of a complex for generation of an AbCID

We reasoned that the ideal complexes to generate selective antibodies against would be those in which a large portion of the small molecule remains solvent exposed when bound. Nature has employed a similar principle in the rapamycin-FKBP12-FRB CID system, where rapamycin first binds FKBP12, generating a new binding surface that is then recognized by FRB. Several other natural products use a similar approach for

artificial protein recruitment.[2] Additional design principles included that the target protein be a small monomeric domain and that the small molecule inducer be commercially available with desirable pharmacokinetic properties and low toxicity, making it potentially useful for animal model applications.

After a survey of small-molecule-bound structures in the Protein Data Bank (http://www.rcsb.org/pdb/home/home.do) we turned our attention to the human BCL-xL/ABT-737 complex (PDB: 2YXJ).[18] BCL-xL is a member of the anti-apoptotic BCL-2 family of proteins.[19] This small monomeric protein (~26 kDa) is located on the outer membrane of the mitochondria where it sequesters pro-apoptotic members of the BCL-2 family. Because of its anti-apoptotic role, a number of animal and clinically active small-molecule inhibitors have been developed against BCL-xL for the treatment of cancers.[20] The crystal structure of our candidate ligand, ABT-737 (**1**)[21], bound to BCL-xL shows that a large portion of ABT-737 is exposed to solvent (308 $Å^2$) providing a potential chemical epitope for antibody binding. In comparison, an analysis of 866 small-molecule-bound structures in the PDB (**Figure 2-2**) revealed a mean solvent exposed surface area of 125 $Å^2$, with rapamycin bound to FKBP12 being an outlier at 528 $Å^2$ (PDB:1FKB).[22] Thus, we felt that the BCL-xL/ABT-737 complex would be an ideal first target for the development of an AbCID.

Selection of chemical-epitope-selective antibodies

To identify unique chemical-epitope-selective antibodies, we utilized a *C*-terminally truncated form of BCL-xL (residues 2–215) that lacks the mitochondrial-transmembrane

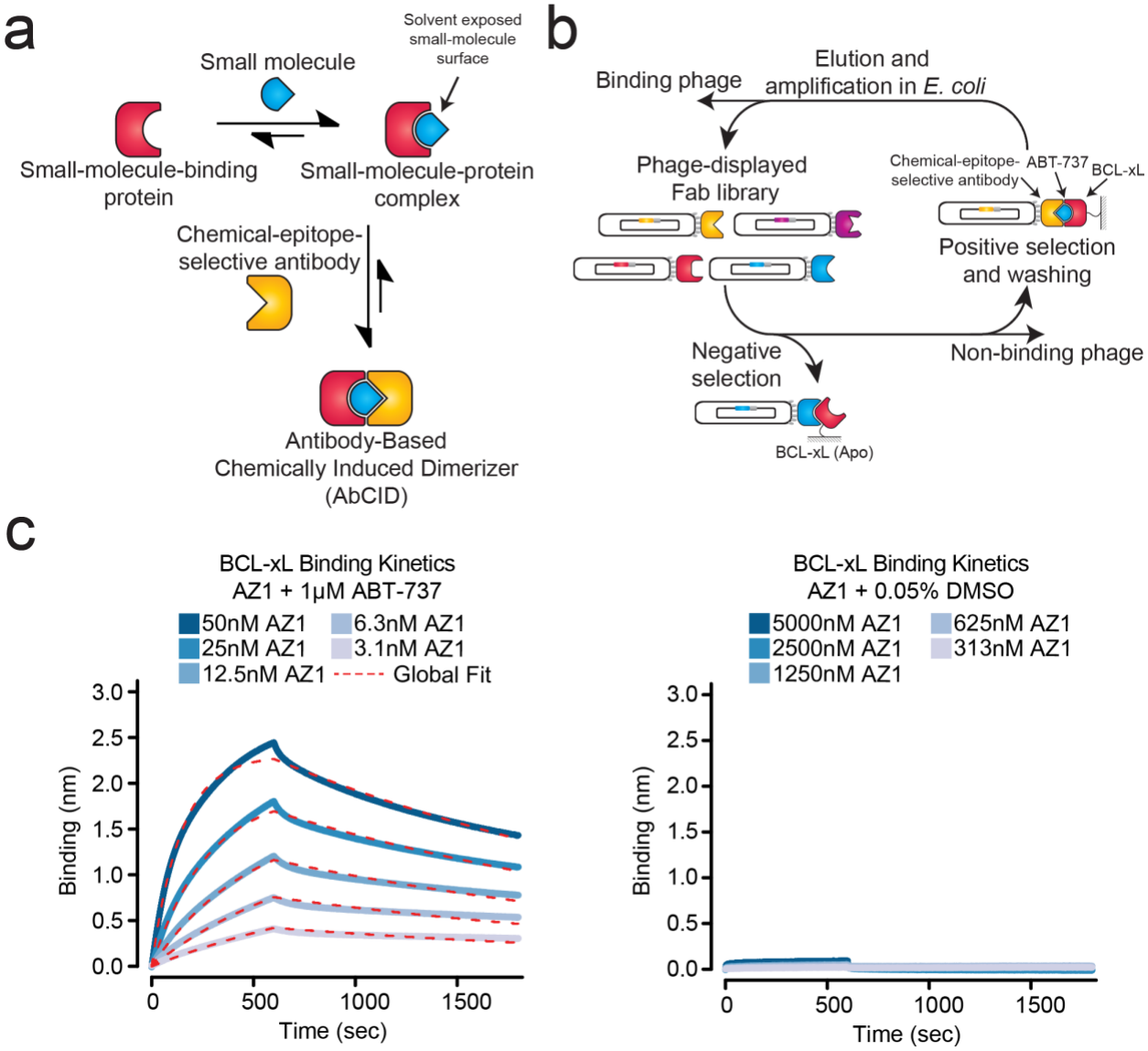

Figure 2-1. Design and characterization of antibody-based chemically induced dimerizers (AbCIDs). (a) Schematic of AbCIDs. (b) Diagram of the phage selection strategy used to select ABT-737-inducible Fab binders of BCL-xL. (c) Biolayer interferometry shows potent and reversible binding of Fab AZ1 to BCL-xL in the presence of ABT-737 (left), but no substantial binding was observed in the absence of ABT-737 (right). Blue curves represent measured data points and dashed red lines represent the global-fit lines used for analysis.

domain. Biotinylated BCL-xL was immobilized on streptavidin resin and used for phage selections with a previously developed synthetic antibody-fragment library and selection stategy.[23] During each round of selection, the phage library was first subjected to stringent counter selection against BCL-xL in the absence of small molecule, thereby removing any Fab-phage that was not selective for the ABT-737-bound form. Positive selections were then performed in the presence of saturating amounts of ABT-737 (1 µM), ensuring that the majority of BCL-xL was bound to ABT-737 (**Figure 2-1B**). A total of four rounds of selection were performed. Encouragingly, we observed significant enrichment of phage titers for selections against BCL-xL in the presence of ABT-737 (**Fig. 2-3**). After round

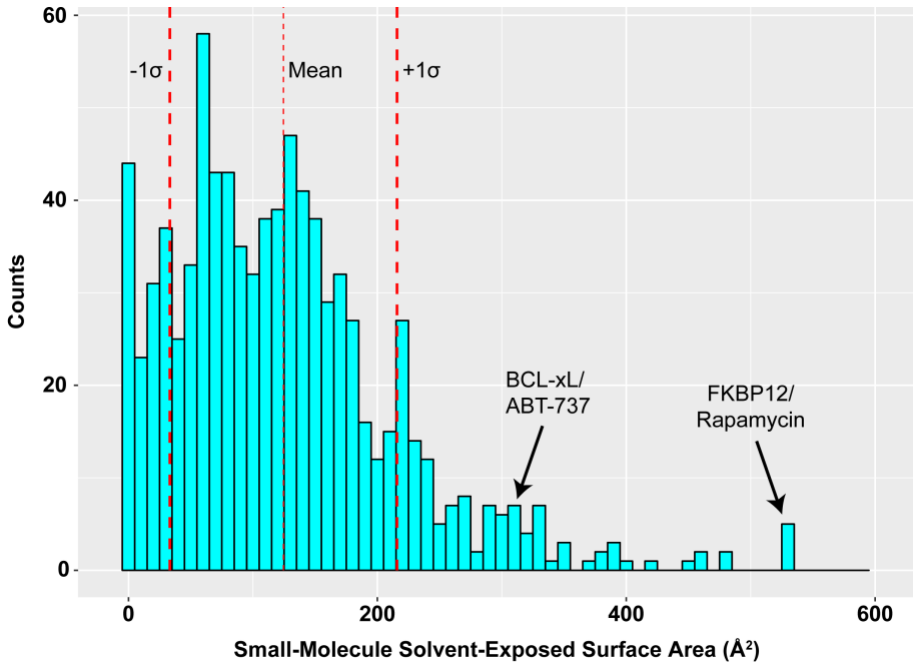

Figure 2-2. Analysis of the solvent accessibility of the small molecule in 866 small-molecule-protein complex crystal structures from the Protein Data Bank. We hypothesized that the large amount of solvent-exposed surface area of ABT-737 when in complex with BCL-xL (308 Å^2) would provide a chemical epitope for direct recognition by an antibody. The FKBP12/rapamycin complex (528 Å^2), which is part of a naturally occurring CID, is a stark outlier in this analysis, supporting our hypothesis.

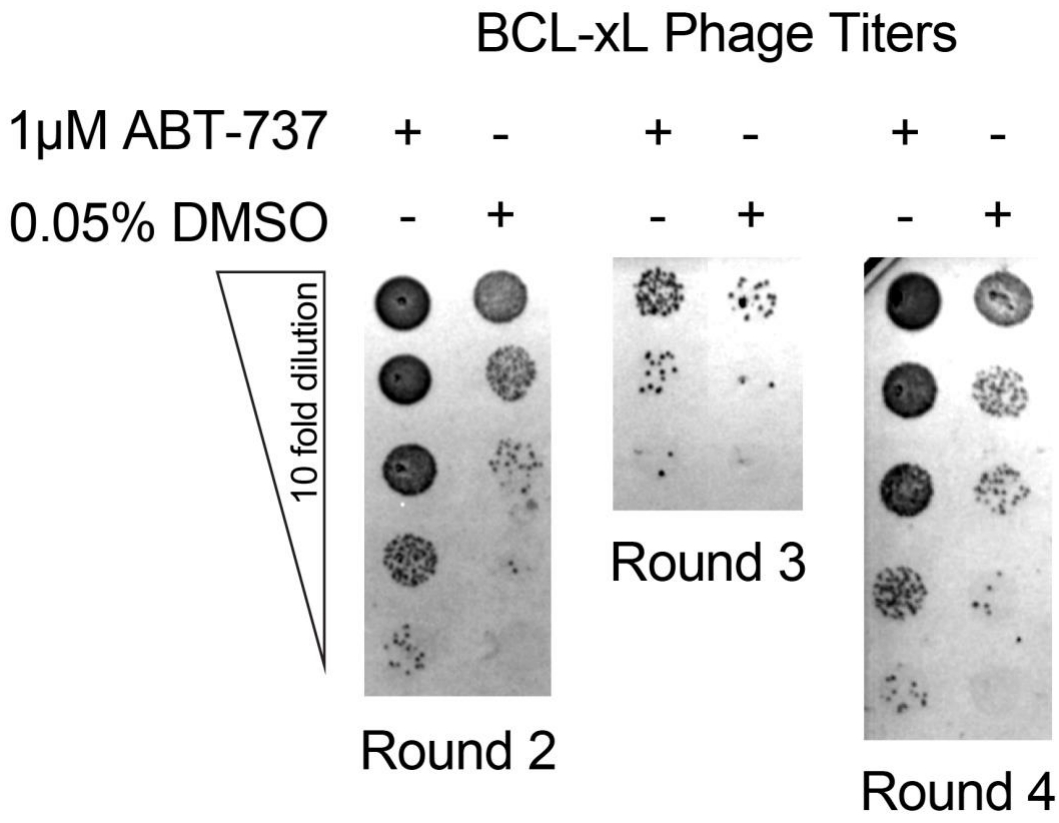

Figure 2-3. Representative titers of phage libraries from Rounds 2 through 4 of Fab-phage selections against BCL-xL bound to ABT-737. Greater than ten-fold enrichment of phage was observed for binding of BCL-xL in the presence of 1 μM ABT-737 compared to DMSO as determined by quantification of recovered colony forming units.

Fab ID	CDR L3	CDR H1	CDR H2	CDR H3
AZ1	YYWGFPSLF	LSYSSM	SISPYSSYTS	GWVGM
AZ2	VSWAYPYLI	IYSYYM	YISPYYSYTS	GYPWYGM
AZ3	GWSGPWLI	IYYSYM	SISPYSSYTS	YGYSYYYYGAL
AZ4	VPAFPI	IYSSSI	SIYPYYGYTY	SWWPYGM
AZ5	WPGWYPI	LYYYYI	SIYPSYGSTY	ASVWFGWYVPSAM
AZ6	SSYSLI	LSYSYI	SIYSSSGSTY	GSHAHGWAWFWYGM
AZ7	SSYSLI	LSSYSM	SIYSYYGSTS	YSPWVYYPYYGWYSGM
AZ8	SGWFFPF	ISYSSI	SISSYYGSTS	TVRGSKKPYFSGWAM
AZ9	SYYYYSGPI	LYYSSI	SISSSYGYTY	TVRGSKKPYFSGWAM
AZ10	SYYFYSGPI	LYSYSM	SISSYYSSTY	TVRGSKKPYFSGWAM

Figure 2-4. Sequences of chemically inducible BCL-xL binding Fab clones. Shown are the amino acid sequences of the complementarity determining regions (CDRs) of all unique Fab clones presented in this study.

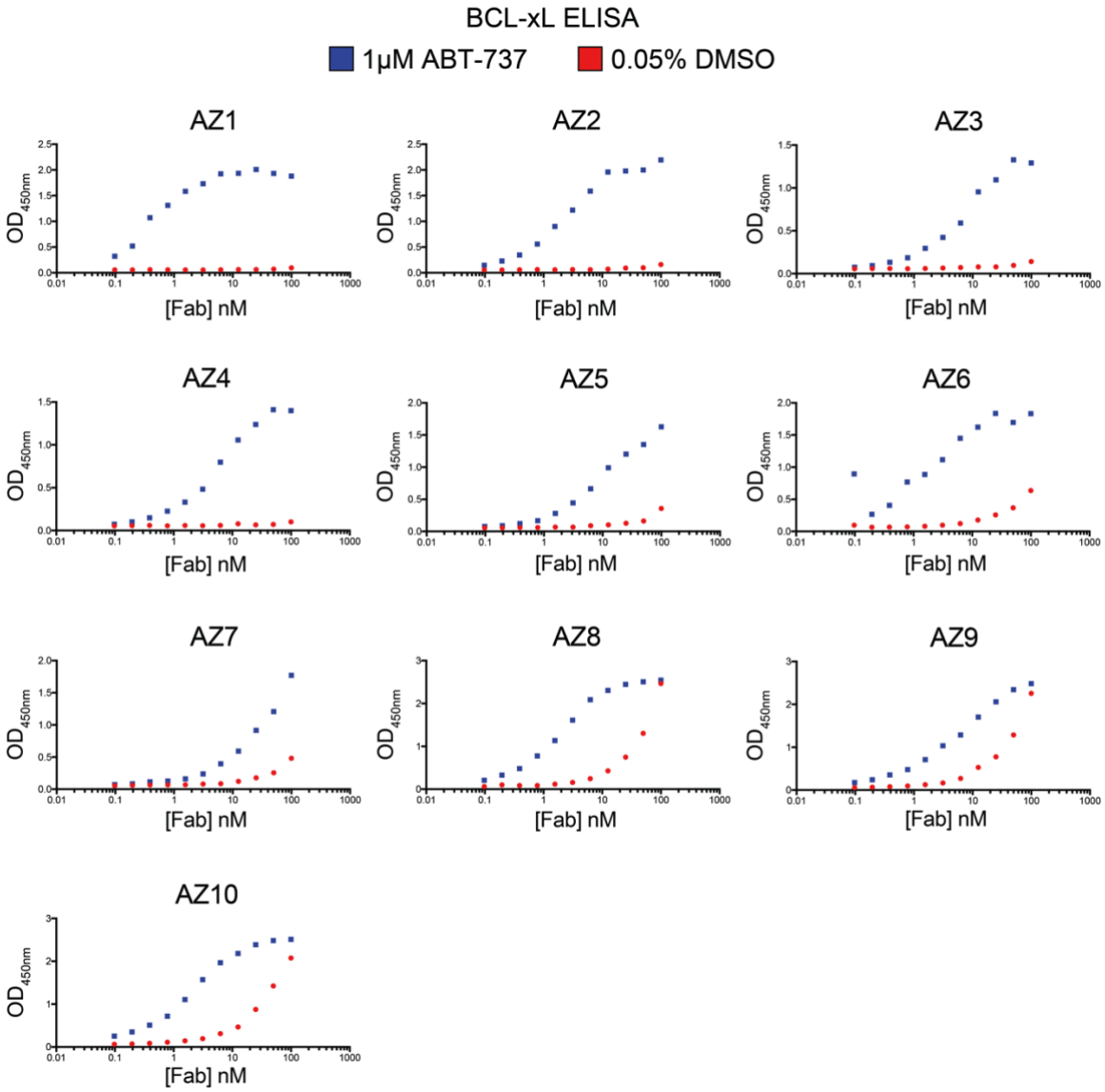

Figure 2-5. ELISA of purified sequence-unique Fabs derived from ABT-737-bound BCL-xL selections. All Fabs showed enhanced binding in the presence of ABT-737. Four out of the ten Fabs tested (AZ 1–4) exhibited high potency and dose-dependent binding to BCL-xL in the presence of ABT-737 with virtually no appreciable binding in the absence of ABT-737. Each data point represents a single measurement.

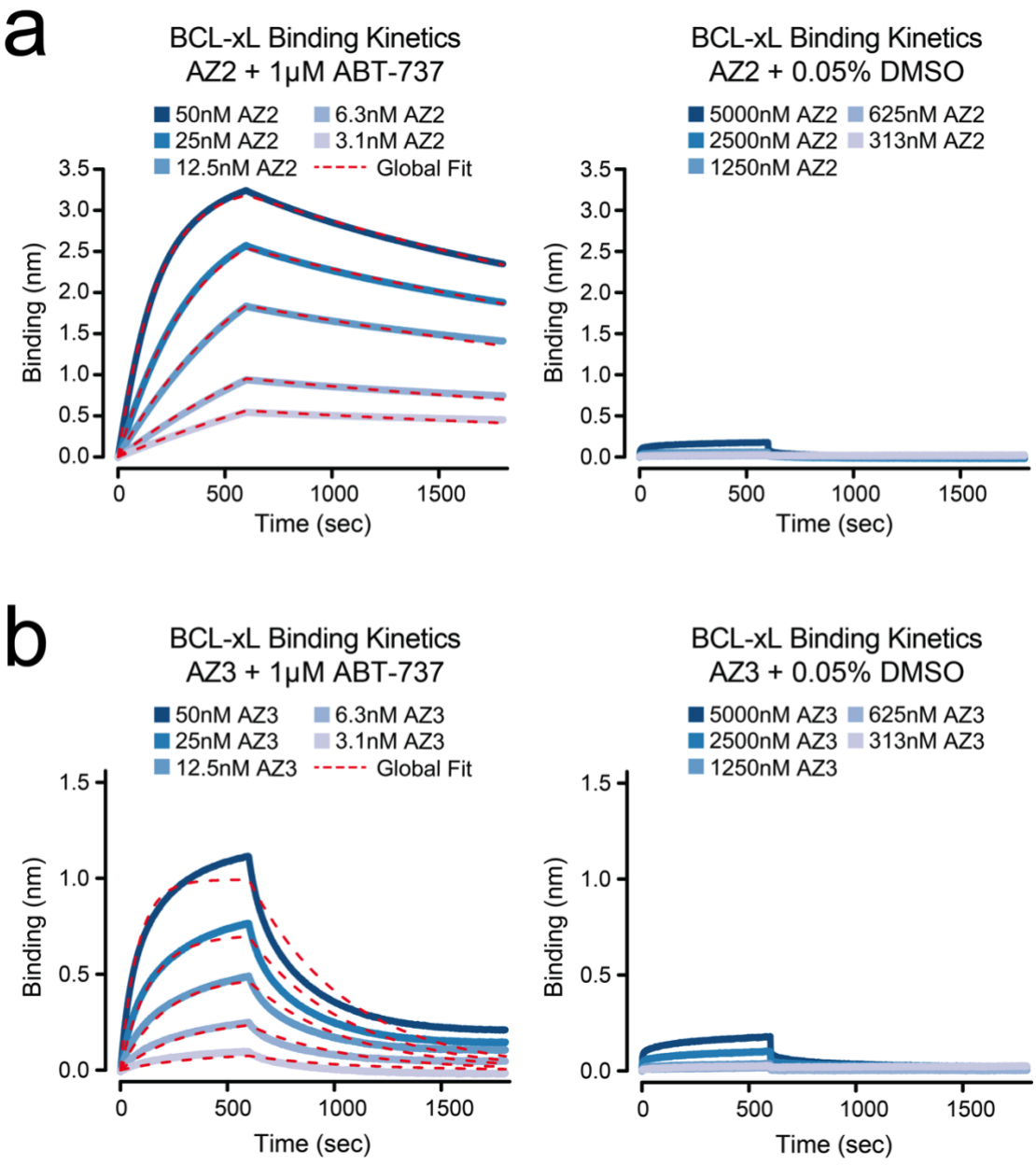

Figure 2-6. Biolayer interferometry of Fabs AZ2 and AZ3. Blue curves represent measured data points and dashed red lines represent the global-fit lines used for analysis **(a)** Fab AZ2 shows potent and reversible binding to BCL-xL in the presence of ABT-737 (left) and no significant binding was observed in the absence of ABT-737 (right). **(b)** Fab AZ3 shows potent binding to BCL-xL in the presence of ABT-737 (left) and negligible binding was observed in the absence of ABT-737 (right).

Fab ID	ABT-737 1μM	K_D (10^{-9}M)	k_{ON} ($10^5 M^{-1}s^{-1}$)	k_{OFF} ($10^{-4}s^{-1}$)
AZ1	+	3.0	1.3	4.0
	-	>5000	N.D.	N.D.
AZ2	+	2.4	1.1	2.6
	-	>5000	N.D.	N.D.
AZ3	+	9.5	2.2	20.9
	-	>5000	N.D.	N.D.

Figure 2-7. Binding and kinetic constants measured for binding of Fabs AZ1–AZ3 to BCL-xL in the presence or absence of ABT-737. N.D. indicates the values could not be determined due to absence of detectable binding.

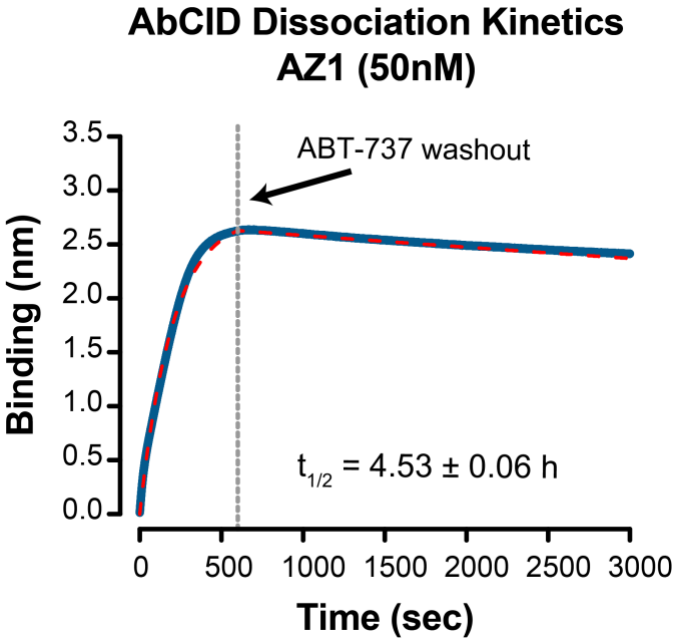

Figure 2-8. Biolayer interferometry of Fab AZ1 with a washout of ABT-737. The blue curve represents measured data points and dashed red lines represents a local-fit line used for analysis. Fab AZ1 shows potent association to BCL-xL in the prescence of 1 μM ABT-737 and dissociation from the BCL-xL/ABT-737 complex upon washout of ABT-737. Data from one replicate is displayed and $t_{1/2}$ was calculated as a mean of 3 independent experiments ± s.d.

four, individual Fab-phage clones were isolated and sequenced. A total of ten Fab-phage with unique sequences in the complementarity-determining regions (CDRs) of the Fab were identified (**Figure 2-4**).

Characterization of AbCIDs selectivity

The unique Fabs were sub-cloned into a bacterial expression vector, expressed, and purified.[23] Gratifyingly, enzyme-linked immunosorbent assays (ELISA) with BCL-xL in the presence or absence of ABT-737 showed that all ten Fabs had enhanced binding in the presence of drug. Several Fabs showed excellent potency and extremely strong selectivity for binding in the presence of ABT-737 (**Figure 2-5**). To further profile the best three Fabs, we characterized the kinetics of BCL-xL binding in the presence or absence of ABT-737 by bio-layer interferometry (**Figure 2-1C** and **Figure 2-6**).[24] All three of the Fabs (AZ1, AZ2 and AZ3) were very potent binders of BCL-xL in the presence of ABT-737 (K_D < 10 nM) and showed no detectable binding in the absence of ABT-737 at concentrations up to 5000 nM of Fab (**Figure 2-7**). Our most selective Fab (AZ2) showed >2000 fold selectivity for the ABT-737-bound form of BCL-xL over the apo form. Formation of the AbCID ternary complex was reversible, either through washout of the Fab (**Figure 2-1C** and **Figure 2-6**) or the small molecule (**Figure 2-8**).

We hypothesized that the exquisite selectivity of our Fabs was the result of direct interactions of the Fab CDRs with parts of ABT-737. We reasoned that if this were the case, the Fab would bind less potently to other BCL-xL-ligand complexes. ABT-263 (**2**) is an analog that binds with similar potency to the same conformation of BCL-xL as ABT-737 (RMSD = 0.8) (**Figure 2-9A, Figure 2-10A**).[25] To test our hypothesis, we measured

the ability of AZ1 to discriminate between ABT-737, ABT-263, and the native-ligand-derived Bak-peptide[26] bound BCL-xL (**Figure 2-9B**). As predicted, we observed dramatically weaker binding of the Fab to the BCL-xL/ABT-263 complex and no detectable binding of Fab to the Bak-peptide complex. Although we do not have a crystal

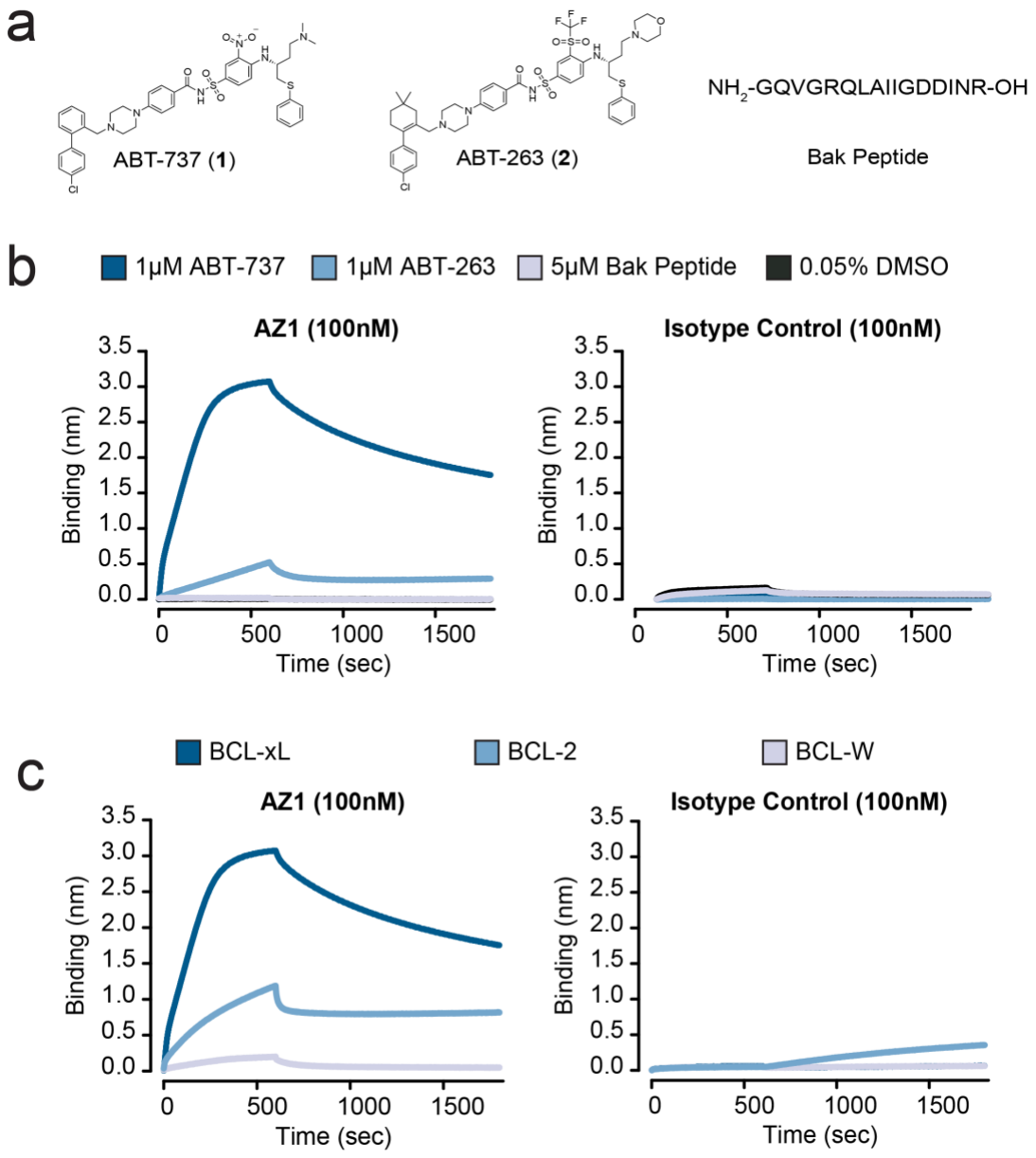

Figure 2-9. Characterization of the Fab AZ1 epitope. (**a**) Chemical structures of ABT-737, ABT-263, and amino acid sequence of Bak peptide. (**b**) Biolayer interferometry shows that Fab AZ1 binds potently to BCL-xL in the presence of ABT-737, with greatly

reduced potency in the presence of ABT-263, and weak or undetectable binding in the presence of Bak peptide. The data show that AZ1 can readily discriminate between subtle structural differences in the small molecules and support that Fab AZ1 is chemical-epitope selective. The isotype control is a Fab selected against CD55, with an identical scaffold to AZ1 but differing complementarity-determining region (CDR) sequences. (**c**) Biolayer interferometry shows that Fab AZ1 binds potently to BCL-xL in the presence of ABT-737, with greatly reduced potency to BCL-W, and undetectably to BCL-2. The data show that AZ1 can readily discriminate between subtle structural differences in the proteins, and support that Fab AZ1 makes important contacts with BCL-xL in addition to its contacts with ABT-737. The isotype control is a Fab selected against CD55, with an identical scaffold to AZ1 but differing CDR sequences.

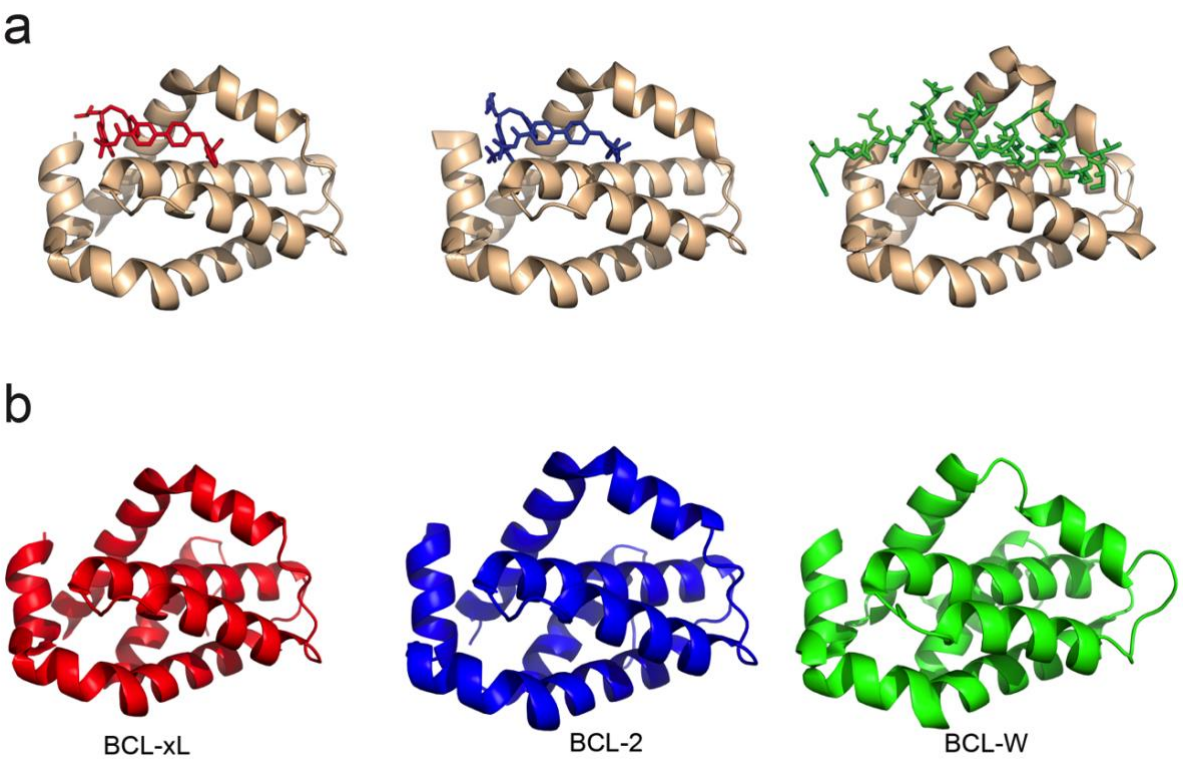

Figure 2-10. Structures of BCL family proteins. (a) The crystal structures of ABT-737, ABT-263, and Bak-peptide bound to BCL-xL (PDB: 2YXJ, 4QNQ, and 5FMK) demonstrate that each ligand binds a nearly identical conformation of BCL-xL. **(b)** The crystal structures of BCL-xL, BCL-2, and BCL-W (PDB: 2YXJ, 4LVT, and 1O0L) show the similar fold and conformation of all three proteins.

structure of the AbCID complex, these data strongly suggest that AZ1 binds near if not over the small-molecule binding site.

While AZ1 is able to discriminate between ABT-737 and its close analog ABT-263, suggesting that ABT-737 comprises a portion of the epitope recognized by AZ1, we hypothesized that AZ1 also makes contacts with BCL-xL. To test this, we measured the ability of AZ1 to bind to ABT-737 bound BCL-W and BCL-2. BCL-W and BCL-2 are both homologs of BCL-xL known to bind ABT-737 with similar potency to BCL-xL.[21] Importantly, BCL-xL, -W, and -2 all have similar folds (**Figure 2-10B**). In the presence of saturating concentrations of ABT-737, AZ1 showed reduced binding to BCL-W and almost no detectable binding to BCL-2, suggesting that the epitope recognized by AZ1 encompasses specific residues on the surface of BCL-xL in addition to specific chemical epitopes on ABT-737 (**Figure 2-9C**). This data supports the hypothesis that AZ1 makes direct contact with both the small molecule and protein portion of the BCL-xL/ABT-737 complex.

In the naturally occurring rapamycin-FKBP12-FRB CID, it is known that rapamycin potently binds FKBP12 (low nM), and has only weak affinity for FRB on its own (μM). However, FRB is able to potently bind the FKBP/rapamycin complex (low nM). As we generated our AZ1 AbCID by selecting for Fabs against the previously known BCL-xL/ABT-737 complex, we hypothesized that our CID assembled using a mechanism similar to rapamycin-FKBP12-FRB. To test this, we utilized differential scanning fluorimetry to look for changes to the T_m of AZ1 in the presence of ABT-737. As

suspected, ABT-737 seemed to have no effect on the T_m of AZ1, suggesting that AZ1 does not bind ABT-737 on its own at the concentrations used in our dimerization assays (**Figure 2-11**). In comparison, BCL-xL, which is known to potently bind ABT-737, showed a ~10 °C increase in T_m in the presence of ABT-737. Together, this data supports a mechanism in which ABT-737 first binds to BCL-xL, creating a new epitope, which is then potently recognized by AZ1.

Protein ID	T_m (˚C) (0.05% DMSO)	T_m (˚C) (20μM ABT-737)	ΔT_m (˚C)
AZ1	78.6	79.0	0.4
AZ2	84.1	84.5	0.4
AZ3	78.4	78.7	0.3
AZ4	80.5	80.5	0.0
AZ5	78.1	78.3	0.2
AZ6	79.6	79.6	0.0
AZ7	75.1	75.3	0.2
AZ8	76.1	76.5	0.4
AZ9	78.2	78.5	0.3
AZ10	76.3	77.0	0.7
Isotype Control	85.0	85.3	0.3
BCL-xL	76.7	86.9	10.2

Figure 2-11. Differential Scanning Fluorimetry of Fabs and BCL-xL in the presence of ABT-737. Fabs AZ1–AZ10 show no significant T_m shift in the presence of ABT-737, supporting that they do not bind ABT-737 in the absence of BCL-xL. In comparison, BCL-xL, which is known to potently bind ABT-737, shows a 10 °C increase in T_m in the

presence of ABT-737. The isotype control is a Fab selected against eGFP, with an identical scaffold to AZ1 but differing CDR sequences. Each data point represents the mean of 3 independent experiments. Instrument measurement co-variation was determined to be ± 0.29 °C.

Application of AbCIDs to regulate gene expression

When developing AbCIDs, we used design principles based on a desire to utilize these tools in regulating cellular therapies. For that reason, when choosing cellular applications to demonstrate AbCIDs, we focused on cellular models of two main cell therapy modalities; regulation of gene expression and activation of immune cells. Furthermore, we attempted to incorporate our AbCIDs into technologies at the cutting edge of these fields (CRISPRa, CAR T-cell), so as to show the great promise of applying AbCIDs to next-generation cell therapies.

Current CID technologies are often used for controlling intracellular signaling pathways.[2, 3] Due to the disulfide bond linking the heavy and light chains of Fabs and the reducing environment inside the cell, it is generally believed that intracellular expression of Fabs in mammalian cells would lead to an inactive species. Recently, we reported a single-chain Fab (scFab) construct in which the light and heavy chains are genetically fused as a single polypeptide.[27] The scFab scaffold has a very high melting temperature (T_m = ~81 °C) so that once formed it is very stable.[27] We hypothesized that conversion of our ABT-737-inducible Fabs into a scFab format may allow for their use in living cells. Indeed, transfection of the AZ1 gene in scFab format (scAZ1) into HEK293T cells resulted in robust expression as measured by immunoblotting (**Figure 2-12**). To test if scAZ1 was active in living cells, we constructed a genetic circuit in which scAZ1 is fused to the VPR transcriptional activation domain[28] and BCL-xL is fused to dCas9[29] (**Figure 2-13A**). Both constructs contain a nuclear localization sequence, which reduces the possibility of interaction with endogenous BCL-xL while simultaneously priming the system for

activation in the nucleus. The dCas9-BCL-xL fusion can be targeted by addition of a specific sgRNA to a promoter that drives a luciferase reporter. If the AbCID functions in cells, addition of ABT-737 should lead to localization of AZ1-VPR to the luciferase reporter, promoting expression of luciferase, which can be readily detected. For comparison, we generated an identical circuit, but utilizing a conventional CID based on the rapamycin-FKBP12-FRB system[10], as recently reported.[30] Indeed, addition of ABT-737 to our engineered cells resulted in robust expression of luciferase, supporting that AZ1 and BCL-xL functioned as an ABT-737-inducible AbCID in living cells (**Figure 1-13B**). The level of activation observed using the AbCID was comparable to that observed by the conventional CID. The induction of luciferase expression was dose dependent, with an EC_{50} of 8.7 ± 1.1 nM (**Figure 2-13C**). This value was consistent with the EC_{50} measured by *in vitro* characterization of the AZ1/ABT-737/BCL-xL complex using biolayer interferometry (**Figure 2-14**). Importantly, addition of ABT-737 to an AbCID-gated system with a negative sgRNA resulted in no increase in luciferase expression (**Figure 2-15**). Together, these results support that our AbCID can be used for tunable control of biological systems in living cells.

Application of AbCIDs to regulate CAR T-cells

The use of engineered T-cells for the treatment of malignancies has recently become an important paradigm in cancer therapeutics.[31] One such approach, known as CAR T-cells, involves the genetic engineering of a T-cell such that it expresses a surface exposed scFv antibody fragment linked to an intracellular T-cell activation domain. The scFv is specific for a tumor antigen, and results in recruitment of the T-cell to the tumor

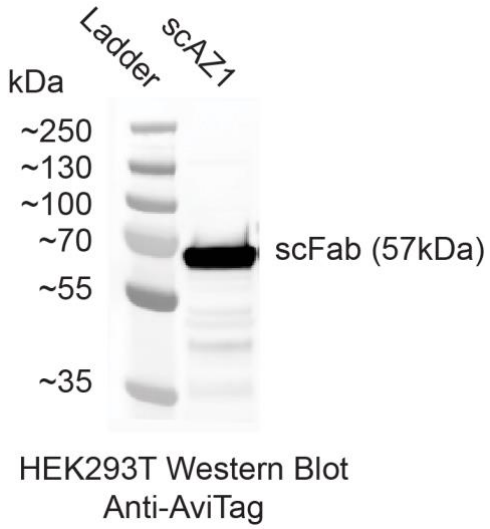

Figure 2-12. Anti-AviTag immunoblotting of HEK293T cell lysate from cells transfected with *C*-terminal Avi-tagged scAZ1.

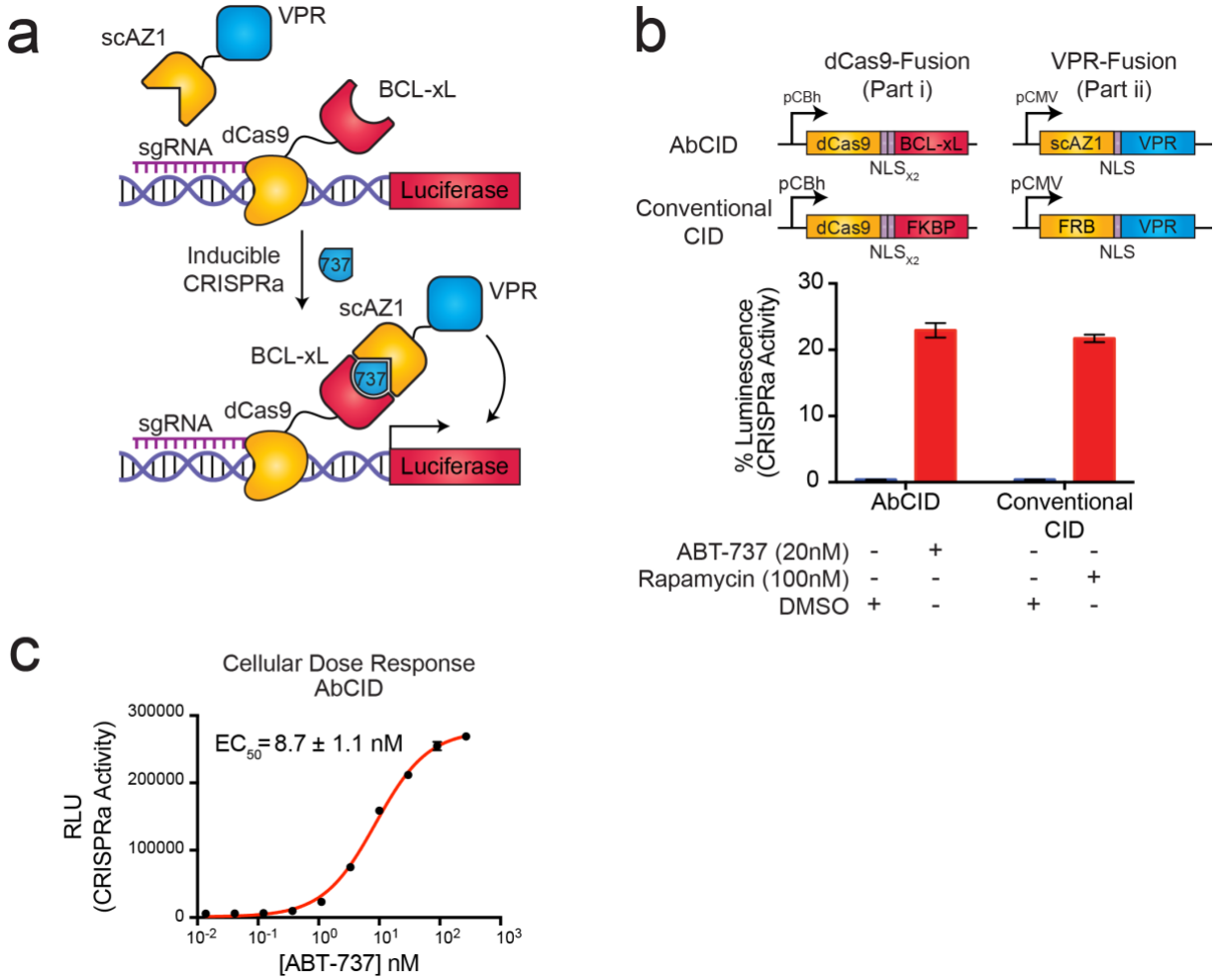

Figure 2-13. A single-chain Fab version of AZ1 can be used as an intracellular AbCID to regulate CRISPRa-mediated gene activation. (**a**) Schematic of the AbCID

regulated gene activation system. Inducible recruitment of the VPR transcriptional activation domain to dCas9 results in the expression of a luciferase reporter. scAZ1 the AZ1 gene in scFab format. (**b**) Quantitation of luciferase activity 48 h after addition of ABT-737 (20 nM) to the AbCID-gated system compared to that seen upon addition of rapamycin (100 nM) to the conventional CID. Values are normalized to a positive control, which is dCas9 genetically fused to VPR, and background subtracted with a negative control, which is dCas9-VPR with a negative sgRNA. Each data point represents the mean of four independent experiments ± s.d. NLS, nuclear localization sequence. (**c**) Dose response after 48 h induction by addition of ABT-737 to the AbCID-gated system. Each data point represents the mean of three independent experiments ± s.d. The EC_{50} reported was calculated from the mean of three independent experiments using three-parameter nonlinear regression ± s.e.m. RLU, relative luminescence units.

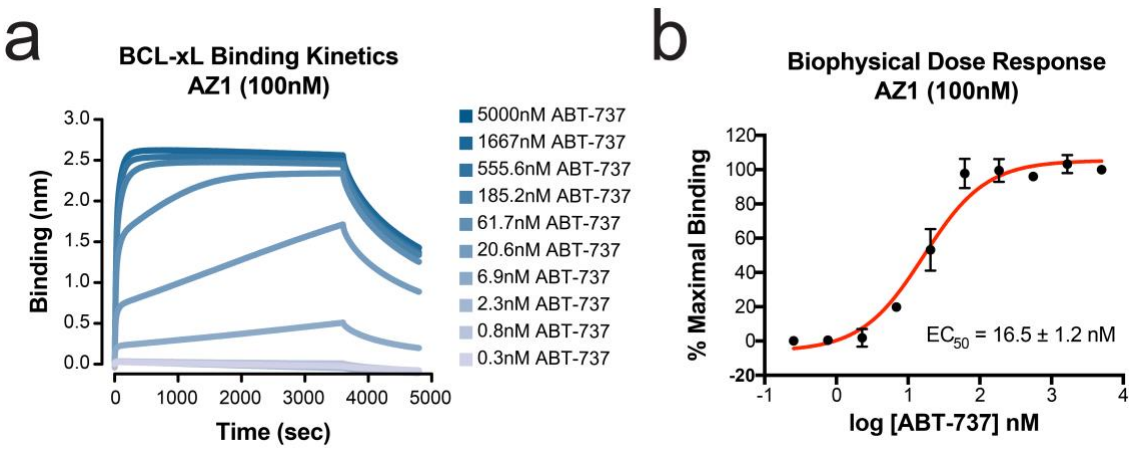

Figure 2-14. Biolayer interferometry of Fab AZ1 with a titration of ABT-737. (a) Fab AZ1 shows ABT-737 dose-dependent binding to BCL-xL. (**b**) Dose-response curve for the induction of AZ1/BCL-xL dimerization by ABT-737. The binding (nm) signal for each ABT-737 concentration at 3600 s was normalized as a percentage of the signal for 5 µM ABT-737 at 3600 s. As saturated binding was not achieved at the lower concentrations of ABT-737 after 3600 s, the EC_{50} reported is likely higher than that which would be observed if the system were at equilibrium. Each data point represents the mean of 3 independent experiments ± s.d. The EC_{50} reported was calculated from the mean of 3 independent experiments using 3-parameter nonlinear regression ± s.e.m.

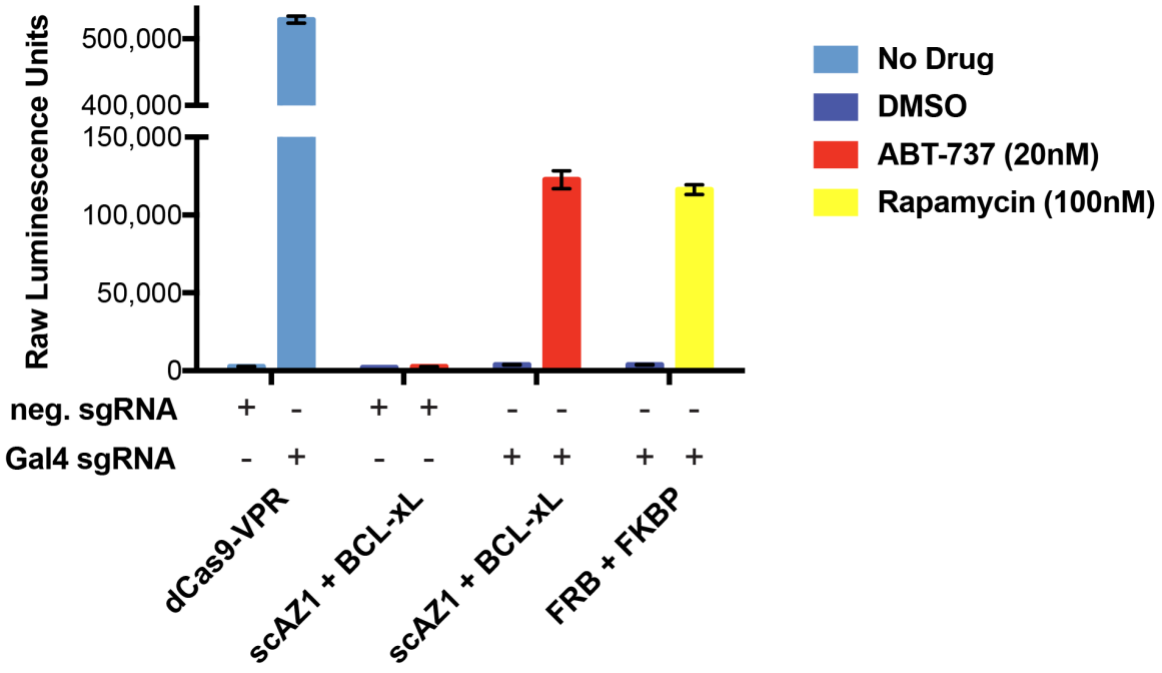

Figure 2-15. Quantitation of luciferase activity 48 hours after addition of ABT-737 (20 nM) to the scAZ1 AbCID gene circuit or rapamycin (100 nM) to the conventional FKBP-FRB CID gene circuit. This raw data was used for normalization and generation of **Figure 2-13B**. Each data point represents the mean of 4 independent experiments ± s.d.

and antigen-dependent activation of the T-cell. This technique has shown great responses in treating leukemia by targeting the CD19 antigen. However, hyperactivation of CAR T-cells has resulted in off-target cytotoxic effects and in some cases death, limiting utility of this promising modality.[31] For this reason, there has been great interest in developing remote control over the activity of these cells, so as to tune the level of activation or end it should untoward toxicity develop.[32-35]

Previous reports of small-molecule-activated CAR T-cells utilize intracellular splitting of the CAR activation domains.[32] An additional approach for control of CAR T-cell activation uses universal protein-based adaptor domains that confer antigen recognition and promote activation of the CAR T-cell when added.[33-35] We hypothesized that by taking advantage of the unique antibody nature of our AbCID system we could generate a hybrid of these two paradigms, with the universal nature of an adaptor strategy but the temporal control of a small-molecule inducible system. To test this, we engineered Jurkat T-cells to express a CAR in which the scFv portion of the CAR is replaced by BCL-xL (**Figure 2-16A–B**). This creates a T-cell that contains the machinery required for activation, but no longer binds to the antigen-presenting cells. In parallel, we generated a bispecific antibody by linking a clinically utilized αCD19 scFv[36] to Fab AZ1. Upon addition of ABT-737 the bispecific antibody will be recruited to the CAR T-cell while simultaneously engaging the $CD19^+$ cells. Such a design allows for both inducible and antigen-dependent CAR T-cell activation. To facilitate rapid quantitation of T-cell activation, we utilized a Jurkat T-cell line that had been engineered to express GFP upon activation of the NFAT pathway.[37] In the presence of $CD19^+$ K562 cells and our bispecific antibody (AZ1-αCD19),

addition of ABT-737 resulted in a dose-dependent activation of the CAR T-cells as measured by expression of GFP (**Figure 2-16C**). Activation of the T-cells was further confirmed by expression of the canonical T-cell activation markers, CD69 and secreted Interleukin-2 (**Figure 2-17**).[38, 39] Importantly, activation of the T-cells was not observed with K562 cells lacking CD19 or if an AbCID was used that did not contain the αCD19 scFv (**Figure 2-16C**). In addition, ABT-737 was not able to induce T-cell activation on its own. While our T-cell system showed ~65% the activation level of the conventional CAR control, the reduced activity may actually be of benefit due to the hyperactivation and toxicity observed with conventional CARs. These data demonstrate that AbCIDs can by used for extracellular regulation of cellular signaling pathways and represent a novel paradigm for small-molecule control of CAR T-cell activation.

AbCIDs activate in a non-toxic concentration regime

ABT-737 is a soluble, cell-permeable, bioavailable, potent, and commercially available compound, making it an excellent molecule for use in a CID, both in cells and potentially in animals. However, it is known that ABT-737 induces apoptosis in some cells types, particularly hematopoietic cells that have high expression levels of BCL-2 family members.[21] We thus tested the concentration of ABT-737 necessary to induce apoptosis in Jurkat, K562, and HEK293T cells. Importantly, the concentration ranges used to induce AbCID CAR (<100 nM) and CRISPRa (<270 nM) activity were below the concentrations at which cell death was observed (Jurkat IC_{50} ~2 μM, K562 IC_{50} >10 μM, and HEK293T IC_{50} ~10 μM) (**Figure 2-18**). ABT-737 has been used extensively in mouse cancer models and is generally well tolerated by mice, except for platelet toxicity.[21] However, the

concentrations used to activate AbCIDs in our cellular assays (<100 nM) are far below the concentration observed to be toxic to platelets (low µM).[40] Additionally, others have also shown that ABT-737 can be applied to activate engineered proteins in live-cell experiments with little observed cytotoxicity.[41] Collectively these data support the feasibility of using ABT-737 activated AbCIDs in cellular and animal applications with minimal effect on the viability of these model organisms. Moreover, while ABT-737's lack of bioorthogonality may be a caveat for research applications, it may actually be of benefit from a therapeutic perspective if the AbCID CAR approach described here were to be applied to the treatment of ABT-737-sensitive B-cell malignancies.

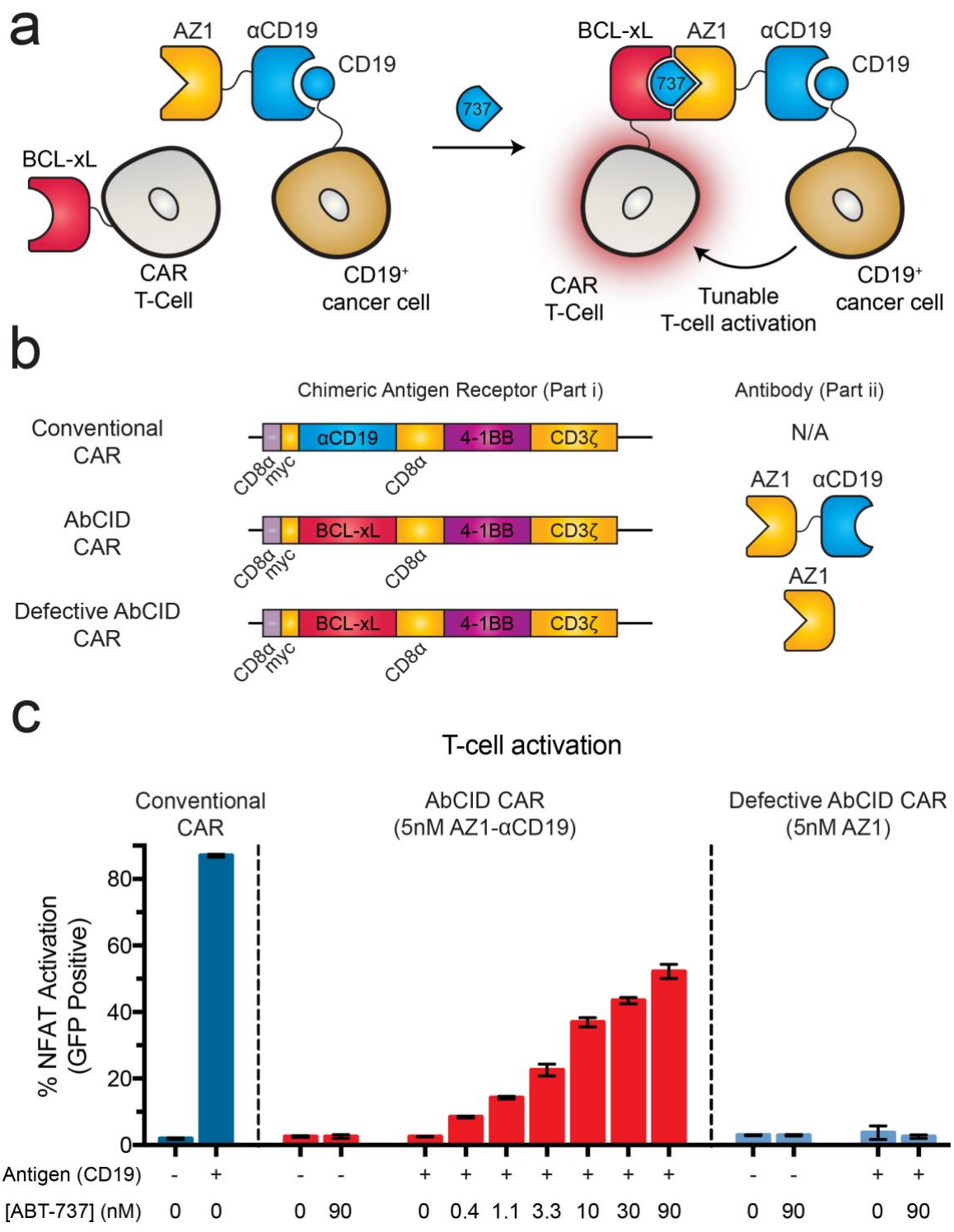

Figure 2-16. AZ1 can be used as an extracellular AbCID to regulate CAR T-cell activation. (**a**) Schematic of AbCID-regulated CAR T-cell activation in which the CAR contains an extracellular BCL-xL domain in place of the typical scFv. Addition of an AZ1-αCD19 bispecific antibody and various concentrations of ABT-737 results in

recruitment to CD19$^+$ cancer cells and tunable activation of the CAR T-cells. (**b**) Linear diagrams of the gene constructs used to produce the CARs and schematics of corresponding antibodies for this study. (**c**) Quantification of NFAT-dependent GFP reporter expression 20 h after initiation of co-culture with either CD19$^+$ or CD19$^-$ K562 target cells and addition of antibody (5 nM) and varying concentrations of small molecule. Addition of ABT-737 in the presence of CD19$^+$ K562 cells and bispecific antibody resulted in dose-dependent activation of the NFAT pathway, but no activation was observed in the absence of ABT-737 or with co-culture of CD19$^-$ K562 cells. Each data point represents the mean of three independent experiments ± s.d.

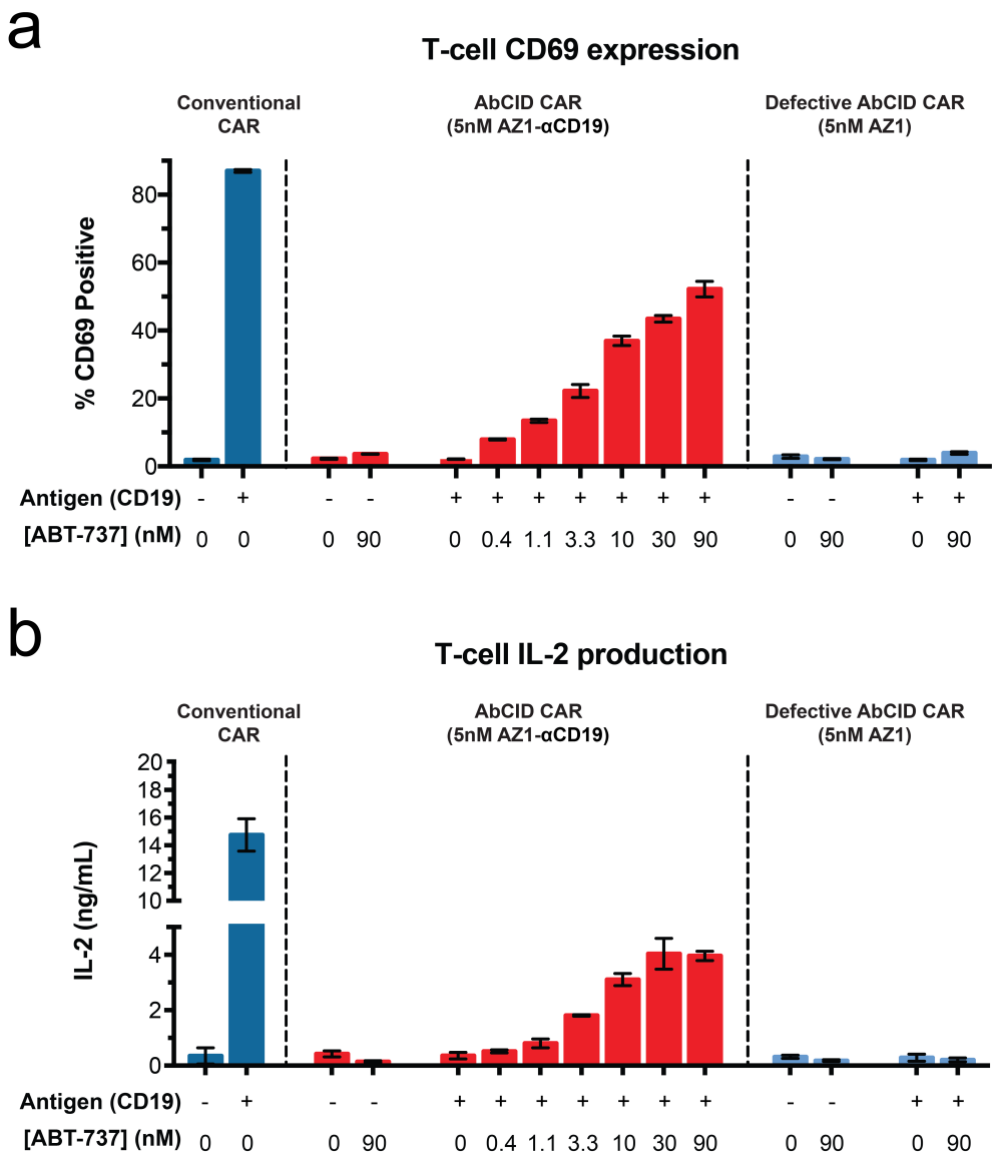

Figure 2-17. Independent confirmation of CAR T-cell activation by the canonical markers CD69 and secreted IL-2 upon dose dependent AbCID activation. (a) Quantification of CD69 expression, as measured by immunofluorescence flow cytometry, 20 hours after initiation of co-culture with either CD19$^+$ or CD19$^-$ K562 target cells and addition of antibody (5 nM) and varying concentrations of small molecule. Addition of

ABT-737 in the presence of CD19$^+$ K562 cells and bispecific antibody resulted in dose-dependent expression of CD69, but no expression was observed in the absence of ABT-737 or when co-cultured with CD19$^-$ K562 cells. The defective AbCID CAR, which lacks the CD19-binding scFv portion of the antibody, elicited no expression of CD69 under all conditions. Each data point represents the mean of 3 independent experiments ± s.d. **(b)** Quantification of IL-2 secretion, as measured by ELISA, 20 hours after initiation of co-culture with either CD19$^+$ or CD19$^-$ K562 target cells and addition of antibody (5 nM) and varying concentrations of small molecule. Addition of ABT-737 in the presence of CD19$^+$ K562 cells and bispecific antibody resulted in dose-dependent secretion of IL-2, but no secretion was observed in the absence of ABT-737 or when co-cultured with CD19$^-$ K562 cells. The defective AbCID CAR, which lacks the CD19-binding scFv portion of the antibody, elicited no secretion of IL-2 under all conditions. Each data point represents the

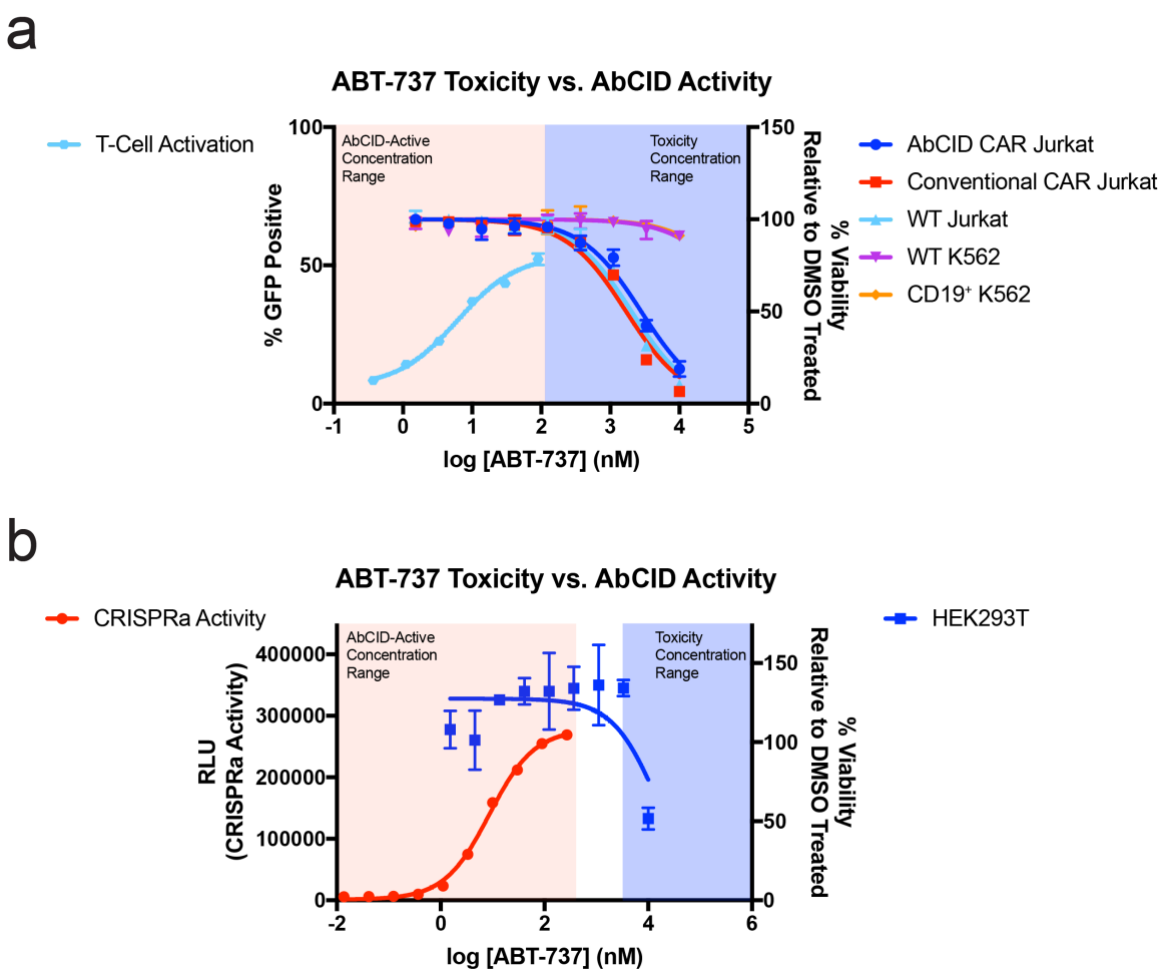

mean of 3 independent experiments ± s.d.

Figure 2-18. The ABT-737 concentration range necessary for AbCID activation falls below that necessary for cell killing. (a) A CellTiter-Glo assay after 24 hours of ABT-737 treatment was used to measure the viability of Jurkat and K562 cells relative to DMSO treatment alone (right axis). Data is juxtaposed with CAR T-cell activation data from **Figure 2-16C** (left axis). The measured AbCID-activation concentration range was lower and exclusive from the toxicity concentration range. **(b)** A CellTiter-Glo assay after 24

hours of ABT-737 treatment was used to measure the viability of HEK293T cells relative to DMSO treatment alone (right axis). Data is juxtaposed with luciferase activity data from **Figure 2-13C** (left axis). The measured AbCID-activation concentration range was lower and exclusive from the toxicity concentration range. Each data point represents the mean of 3 independent experiments ± s.d.

Discussion

Here we described a novel method to rapidly generate chemically induced dimerizers using known small-molecule-protein complexes and synthetic antibody libraries. We demonstrated this method by generating AbCIDs from the BCL-xL/ABT-737 complex. Additionally, we showed that these AbCIDs could be applied to regulate a diverse range of biological processes in living cells, including CRISPRa mediated gene expression and CAR T-cell activation. Finally, we showed that the concentration range of ABT-737 used to activate AbCIDs was far below the concentration at which toxicity was observed in cells.

One of the inspirations for developing AbCIDs came from previous work showing it possible to use phage display to generate antibodies that could specifically bind to protein conformations “trapped” by binding of small molecules.[42-45] In these cases, the antibody shows an increased affinity for the small-molecule-bound form of the protein, similar to a CID. However, the antibody is often able to bind the protein in the trapped conformation, independent of small molecule. For this reason, the selectivity of conformation-selective antibodies for the bound form over the apo form is limited, reducing their utility as CIDs. With the development of AbCIDs, we generated antibodies that target a small-molecule-protein complex but utilize the small-molecule as part of the binding epitope. This provided higher selectivity for the bound form of the protein, and in turn, the desired properties for use as CIDs. This solution is reminiscent of several naturally occurring CID systems, including the rapamycin-FKBP12-FRB system, in which

binding of rapamycin to FKBP12 creates a novel-binding surface necessary for recognition by FRB.

While rapamycin has favorable PK properties in humans, its toxicity and immunosuppressant properties make it incompatible with regulating CAR T-cell therapy. In cellular CID assays, researchers typically use rapamycin in a concentration range of 30–100 nM, despite rapamycin toxicity being observed in cell lines at concentrations of 100–300 nM, a difference of only 3-fold.[12, 46, 47] In comparison, the EC_{50} for activation of our AbCID CAR with ABT-737 is ~6 nM and the IC_{50} for cell killing is ~2 μM, a >330-fold difference. While the commonly used rapamycin analog AP21967 lacks the toxicity and immunosuppressive properties of rapamycin, its short half-life in mouse plasma (<4 hr) greatly reduces its utility in activating cell therapies *in vivo*. In fact, previous studies demonstrating small-molecule activation of CAR T-cells in mice have been limited due to the PK liabilities of AP21967.[32] Fortunately, ABT-737 has been shown to have a half-life in mouse plasma of 14–18 hr, which should greatly facilitate the use of our AbCIDs to activate CAR T-cells in mouse models of cancer.[48]

To our knowledge, AbCIDs represent the first demonstration of a general strategy to engineer CIDs from existing small-molecule-protein interaction pairs. While in this study we have utilized synthetic antibody fragment libraries, we envision that diversity libraries built upon alternative binding scaffolds could be applied to this technique, including but not limited to, DARPins, FNIII, ubiquitin, knottins, and nucleic acid aptamer libraries.[49, 50] We envision that much of the power of our strategy will come from the ability to rapidly

generate new AbCIDs from different small-molecule-protein pairs in which a significant portion of the small-molecule is solvent accessible. We believe that AbCIDs represent a novel and promising approach to develop next-generation CID tools with the properties necessary for application in human cell therapies.

Acknowledgments

We thank Sachdev Sidhu (University of Toronto) for providing the phage-displayed Fab library. We thank Arthur Weiss (UCSF) and Theresa Kadlecek (UCSF) for kindly providing the NFAT-dependent GFP reporter Jurkat cell line. Funding was provided by R01 grants from the NIH (CA191018 and GM097316). Z.B.H. was supported by a postdoctoral fellowship from the Helen Hay Whitney Foundation and HHMI, as well as a Pathway to Independence Award from the NIH-NCI (K99CA203002). A.J.M. was supported by a predoctoral fellowship from the NSF GRFP. D.P.N. is the Connie and Bob Lurie Fellow of the Damon Runyon Cancer Research Foundation (DRG-2204-14).

Author Contributions

Z.B.H. and A.J.M. performed all experiments except those explicitly stated. D.P.N. designed experiments, prepared constructs, prepared cell lines, and performed experiments related to small-molecule control of CRISPRa-mediated gene expression. Z.B.H., A.J.M., and J.A.W. designed the research and analyzed the data. Z.B.H., A.J.M., and J.A.W. wrote the paper. All authors edited the paper.

References

1. Spencer, D.M., Wandless, T.J., Schreiber, S.L. & Crabtree, G.R. Controlling signal transduction with synthetic ligands. *Science* **262**, 1019-1024 (1993).
2. Fegan, A., White, B., Carlson, J.C. & Wagner, C.R. Chemically controlled protein assembly: techniques and applications. *Chem. Rev.* **110**, 3315-3336 (2010).
3. DeRose, R., Miyamoto, T. & Inoue, T. Manipulating signaling at will: chemically-inducible dimerization (CID) techniques resolve problems in cell biology. *Pflugers Arch* **465**, 409-417 (2013).
4. Lienert, F., Lohmueller, J.J., Garg, A. & Silver, P.A. Synthetic biology in mammalian cells: next generation research tools and therapeutics. *Nat. Rev. Mol. Cell Biol.* **15**, 95-107 (2014).
5. Shekhawat, S.S. & Ghosh, I. Split-protein systems: beyond binary protein-protein interactions. *Curr. Opin. Chem. Biol.* **15**, 789-797 (2011).
6. Nguyen, D.P. *et al.* Ligand-binding domains of nuclear receptors facilitate tight control of split CRISPR activity. *Nat. Commun.* **7**, 12009 (2016).
7. Straathof, K.C. *et al.* An inducible caspase 9 safety switch for T-cell therapy. *Blood* **105**, 4247-4254 (2005).
8. Di Stasi, A. *et al.* Inducible apoptosis as a safety switch for adoptive cell therapy. *N.Engl. J. Med.* **365**, 1673-1683 (2011).
9. DeFrancesco, L. CAR-T's forge ahead, despite Juno deaths. *Nat. Biotechnol.* **35**, 6-7 (2017).
10. Rivera, V.M. *et al.* A humanized system for pharmacologic control of gene expression. *Nat. Med.* **2**, 1028-1032 (1996).
11. Farrar, M.A., Alberol-Ila, J. & Perlmutter, R.M. Activation of the Raf-1 kinase cascade by coumermycin-induced dimerization. *Nature* **383**, 178-181 (1996).
12. Miyamoto, T. *et al.* Rapid and orthogonal logic gating with a gibberellin-induced dimerization system. *Nat. Chem. Biol.* **8**, 465-470 (2012).
13. Erhart, D. *et al.* Chemical development of intracellular protein heterodimerizers. *Chem. Biol.* **20**, 549-557 (2013).
14. Kopytek, S.J., Standaert, R.F., Dyer, J.C. & Hu, J.C. Chemically induced dimerization of dihydrofolate reductase by a homobifunctional dimer of methotrexate. *Chem. Biol.* **7**, 313-321 (2000).
15. Liang, F.S., Ho, W.Q. & Crabtree, G.R. Engineering the ABA plant stress pathway for regulation of induced proximity. *Sci. Signal.* **4**, rs2 (2011).
16. Czlapinski, J.L. *et al.* Conditional glycosylation in eukaryotic cells using a biocompatible chemical inducer of dimerization. *J. Am. Chem. Soc.* **130**, 13186-13187 (2008).
17. Schellekens, H. Factors influencing the immunogenicity of therapeutic proteins. *Nephrol. Dial. Transplant* **20 Suppl 6**, vi3-9 (2005).
18. Lee, E.F. *et al.* Crystal structure of ABT-737 complexed with Bcl-xL: implications for selectivity of antagonists of the Bcl-2 family. *Cell Death Differ.* **14**, 1711-1713 (2007).

19. Czabotar, P.E., Lessene, G., Strasser, A. & Adams, J.M. Control of apoptosis by the BCL-2 protein family: implications for physiology and therapy. *Nat. Rev. Mol. Cell Biol.* **15**, 49-63 (2014).
20. Besbes, S., Mirshahi, M., Pocard, M. & Billard, C. New dimension in therapeutic targeting of BCL-2 family proteins. *Oncotarget* **6**, 12862-12871 (2015).
21. Oltersdorf, T. *et al.* An inhibitor of Bcl-2 family proteins induces regression of solid tumours. *Nature* **435**, 677-681 (2005).
22. Van Duyne, G.D., Standaert, R.F., Karplus, P.A., Schreiber, S.L. & Clardy, J. Atomic structures of the human immunophilin FKBP-12 complexes with FK506 and rapamycin. *J. Mol. Biol.* **229**, 105-124 (1993).
23. Hornsby, M. *et al.* A High Through-put Platform for Recombinant Antibodies to Folded Proteins. *Mol. Cell. Proteomics* **14**, 2833-2847 (2015).
24. Shah, N.B. & Duncan, T.M. Bio-layer interferometry for measuring kinetics of protein-protein interactions and allosteric ligand effects. *J. Vis. Exp.*, e51383 (2014).
25. Tse, C. *et al.* ABT-263: a potent and orally bioavailable Bcl-2 family inhibitor. *Cancer Res.* **68**, 3421-3428 (2008).
26. Sattler, M. *et al.* Structure of Bcl-xL-Bak peptide complex: recognition between regulators of apoptosis. *Science* **275**, 983-986 (1997).
27. Koerber, J.T., Hornsby, M.J. & Wells, J.A. An improved single-chain Fab platform for efficient display and recombinant expression. *J. Mol. Biol.* **427**, 576-586 (2015).
28. Chavez, A. *et al.* Highly efficient Cas9-mediated transcriptional programming. *Nat. Methods* **12**, 326-328 (2015).
29. Qi, L.S. *et al.* Repurposing CRISPR as an RNA-guided platform for sequence-specific control of gene expression. *Cell* **152**, 1173-1183 (2013).
30. Gao, Y. *et al.* Complex transcriptional modulation with orthogonal and inducible dCas9 regulators. *Nat. Methods* **13**, 1043-1049 (2016).
31. Fesnak, A.D., June, C.H. & Levine, B.L. Engineered T cells: the promise and challenges of cancer immunotherapy. *Nat. Rev. Cancer* **16**, 566-581 (2016).
32. Wu, C.Y., Roybal, K.T., Puchner, E.M., Onuffer, J. & Lim, W.A. Remote control of therapeutic T cells through a small molecule-gated chimeric receptor. *Science* **350**, aab4077 (2015).
33. Cao, Y. *et al.* Design of Switchable Chimeric Antigen Receptor T Cells Targeting Breast Cancer. *Angew. Chem. Int. Ed.* **55**, 7520-7524 (2016).
34. Rodgers, D.T. *et al.* Switch-mediated activation and retargeting of CAR-T cells for B-cell malignancies. *Proc. Natl. Acad. Sci. USA* **113**, E459-468 (2016).
35. Ma, J.S. *et al.* Versatile strategy for controlling the specificity and activity of engineered T cells. *Proc. Natl. Acad. Sci. USA* **113**, E450-458 (2016).
36. June, C.H., Levine, B.L., Porter, D.L., Kalos, M.D. & Michael, M.C. Compositions and methods for treatment of cancer. US Patent 9,540,445 (2017).
37. Wei, P. *et al.* Bacterial virulence proteins as tools to rewire kinase pathways in yeast and immune cells. *Nature* **488**, 384-388 (2012).
38. Ziegler, S.F., Ramsdell, F. & Alderson, M.R. The activation antigen CD69. *Stem Cells* **12**, 456-465 (1994).

39. Smith-Garvin, J.E., Koretzky, G.A. & Jordan, M.S. T cell activation. *Annu. Rev. Immunol.* **27**, 591-619 (2009).
40. Zhang, H. *et al.* Bcl-2 family proteins are essential for platelet survival. *Cell Death Differ.* **14**, 943-951 (2007).
41. Goreshnik, I. & Maly, D.J. A small molecule-regulated guanine nucleotide exchange factor. *J. Am. Chem. Soc.* **132**, 938-940 (2010).
42. Gao, J., Sidhu, S.S. & Wells, J.A. Two-state selection of conformation-specific antibodies. *Proc. Natl. Acad. Sci. USA* **106**, 3071-3076 (2009).
43. Rizk, S.S. *et al.* Allosteric control of ligand-binding affinity using engineered conformation-specific effector proteins. *Nat. Struct. Mol. Biol.* **18**, 437-442 (2011).
44. Staus, D.P. *et al.* Allosteric nanobodies reveal the dynamic range and diverse mechanisms of G-protein-coupled receptor activation. *Nature* **535**, 448-452 (2016).
45. Thomsen, N.D., Koerber, J.T. & Wells, J.A. Structural snapshots reveal distinct mechanisms of procaspase-3 and -7 activation. *Proc. Natl. Acad. Sci. USA* **110**, 8477-8482 (2013).
46. Barlow, A.D. *et al.* Rapamycin toxicity in MIN6 cells and rat and human islets is mediated by the inhibition of mTOR complex 2 (mTORC2). *Diabetologia* **55**, 1355-1365 (2012).
47. Wang, B. *et al.* Rapamycin inhibiting Jurkat T cells viability through changing mRNA expression of serine/threonine protein phosphatase 2A. *Transpl. Immunol.* **26**, 50-54 (2012).
48. Kelly, P.N., Grabow, S., Delbridge, A.R., Adams, J.M. & Strasser, A. Prophylactic treatment with the BH3 mimetic ABT-737 impedes Myc-driven lymphomagenesis in mice. *Cell Death Differ.* **20**, 57-63 (2013).
49. Fiedler, M. & Skerra, A. in *Handbook of Therapeutic Antibodies*. Vol. 1. (eds. Dubel, S. & Reichert, J.M.) 435-474 (Wiley-VCH Verlag GmbH & Co. KGaA, 2014).
50. Kong, H.Y. & Byun, J. Nucleic Acid aptamers: new methods for selection, stabilization, and application in biomedical science. *Biomol. Ther.* **21**, 423-434 (2013).

Online Methods

Small molecule and peptide reagents. ABT-737 (>99%, ChemieTek CT-A737), ABT-263 (>99%, Selleckchem S1001), and Bak-peptide (>95%, Anaspec AS-61616) were used without further purification. For use, ABT-737, ABT-263, and Bak-peptide were each dissolved in DMSO as 10 mM stocks. Stocks were stored at –80 °C until used.

Analysis of ligand solvent exposure. Small-molecule-protein complexes were identified in the Protein Data Bank (http://www.rcsb.org/pdb/home/home.do) using their in-house advanced search feature. Search parameters used were: Molecular Weight Search: Min Molecular Weight=100.0 Max Molecular Weight=50000.0 and Binding Affinity: Binding affinity min is 0.001 and Binding affinity max is 1000 and Affinity Type is Ki and TAXONOMY is just Homo sapiens (human) and TAXONOMY is only just Homo sapiens (human). The list generated was then curated by hand so as to remove complexes in which the ligand was not an organic small molecule, resulting in a final list of 866 structures. Solvent accessible surface area for bound ligands was calculated using Naccess V2.1.1 with default parameters and hydrogen and heteroatoms considered in the calculation. The plot of solvent exposed surface area was generated using the ggplot2 package in R-studio.

Expression and biotinylation of BCL-xL, BCL-2, and BCL-W. The genes encoding *C*-terminally truncated BCL-xL (residues 2–215), BCL-2 (residues 2–207), and BCL-W (residues, 2–164) with an *N*-terminal AviTag were purchased as gBlocks™ (IDT). The

genes were cloned into the pMCSG7 vector[56] using Gibson cloning. For BCL-xL a Tabaco Etch Virus (TEV) cut site was then introduced between the AviTag and BCL-xL domain using sight directed mutagenesis. The genes for BCL-2 and BCL-W were purchased with a TEV-cut site already incorporated. The sequence of the final constructs were confirmed by sequencing of the entire gene. The plasmids were transformed into BL21(DE3) *E. coli* cells and a single colony was used to inoculate 1.5 L of 2xYT media containing carbenicillin (100 µg/mL). The culture was grown at 37 °C to an OD_{600} of 1-1.2, cooled to 18 °C for 1 h and then induced at 18 °C overnight with 0.5 mM IPTG. Cells were harvested by centrifugation and the pellet were stored at –80 °C.

For each protein purification, the pellet was thawed at 0 °C and then re-suspended in 10 mL of lysis buffer (50 mM Tris, pH 8.0, 200 mM NaCl, 20 mM imidazole) supplemented with PMSF (100 µg/mL). The cells were lysed using a micro-fludizer and the lysate was cleared by centrifugation at 4 °C. The cleared lysate was added to 400 µL of Ni-NTA Superflow resin (Qiagen) and rotated at 4 °C for 1 h. The resin was washed (3x) with lysis buffer and then transferred to a spin column. The purified protein was eluted with elution buffer (50 mM Tris, pH 8.0, 200 mM NaCl, 600 mM imidazole). Fractions were analyzed by SDS-PAGE and those that were found to be >95% pure were pooled, exchanged into storage buffer (25 mM Tris, pH 8.0, 150 mM NaCl, 1 mM DTT) and concentrated.

The purified BCL-xL, BCL-2, and BCL-w proteins were biotinylated on their AviTags using the standard protocol provided by Avidity. Biotinylation was monitored by intact protein mass spectrometry on a Xevo G2-XS Mass Spectrometer (Waters) and found to be quantitative. The biotinylated proteins were then purified on Ni-NTA as

described above, separated into aliquots, analyzed by SDS-PAGE (**Figure 2-19**), snap-frozen, and stored at –80 °C for later use.

Phage display selections and phage titering. All phage selections were done according to previously established protocols.[57] Briefly, selections with antibody phage library F were performed using biotinylated BCL-xL captured with streptavidin-coated magnetic beads (Promega). Prior to each selection, the phage pool was incubated with 1 µM of BCL-xL immobilized on streptavidin beads in the absence of ABT-737 in order to deplete the library of any binders to the apo form of BCL-xL. Subsequently, the beads were removed and ABT-737 was added to the phage pool at a concentration of 1 µM. In total, four rounds of selection were performed with decreasing amounts of BCL-xL antigen (100 nM, 50 nM, 10 nM and 10 nM). To reduce the deleterious effects of nonspecific binding phage, we employed a "catch and release" strategy, where specific BCL-xL binding Fab-phage were selectively eluted from the magnetic beads by the addition of 2 µg/mL TEV protease. Individual phage clones from the fourth round of selection were analyzed for sequencing.

Phage titers were performed according to standard protocols. Briefly, TEV eluted phage were used to infect log-phase XL1-Blue *E. coli* cells (Stratagene). Infected cells were incubated at room temperature for 20 minutes on an orbital shaker. Cells were then serially diluted and spotted on LB agar-plates with carbenicillin (50µg/mL) and incubated overnight at 37 °C. Phage titers were measured for each round of selections against both the BCL-xL/ABT-737 complex and against apo BCL-xL.

Expression of Fabs. Fabs were expressed according to a previously described protocol.[57] Briefly, C43 (DE3) Pro+ *E. coli* containing expression plasmids were grown in 2xYT at 37 °C to an OD_{600} of 0.6–0.8 and then Fab expression was induced by the addition of 1 mM IPTG. Incubation temperature was subsequently reduced to 30 °C and the cultures were allowed to shake for 16–18 h. Cells were harvested by centrifugation and Fabs were purified by Protein A affinity chromatography. Fab purity and integrity was assessed by SDS-PAGE (**Figure 2-20**) and intact protein mass spectrometry using a Xevo G2-XS Mass Spectrometer (Waters).

Fab ELISAs. ELISAs were performed according to standard protocols.[57] Briefly, 96-well Maxisorp plates were coated with NeutrAvidin (10 µg/ml) overnight at 4 °C and subsequently blocked with BSA (2% w/v) for 1 h at 20 °C. 20 nM of biotinylated BCL-xL was captured on the NeutrAvidin-coated wells for 30 minutes followed by the addition of various concentrations of Fab with either 1 µM ABT-737 or 0.05% DMSO for 30 minutes. The bound Fabs were then detected using a horseradish peroxidase (HRP)-conjugated anti-Fab monoclonal antibody (Jackson ImmunoResearch 109-036-097).

Binding kinetics analysis. Biolayer interferometery data were measured using an Octet RED384 instrument (ForteBio). Biotinylated BCL-xL, BCL-2, or BCL-W were immobilized on a Streptavidin (SA) biosensor using a 200 nM solution. Serial dilutions of Fabs in kinetics buffer (PBS, pH 7.4, 0.05% Tween-20, 0.2% BSA, 10 µM biotin) with small molecule (1 µM), peptide (5 µM), or vehicle (0.05% DMSO) were used as analyte. Affinity (K_D) and kinetic parameters (k_{on} and k_{off}) were calculated from a global fit (1:1) of the data

using the Octet RED384 software. For the ABT-737 titration experiment, the concentration of AZ1 was held constant (100 nM) with serially diluted concentrations of ABT-737. For the ABT-737 washout experiment, the disassociation step was performed in the presence of AZ1 (50 nM) but absence of ABT-737.

Differential Scanning Fluorometry. DSF was conducted on a LC480 Lightcycler Instrument II (Roche). Briefly, purified recombinant protein was diluted to 5 µM in DSF buffer (PBS, pH 7.4, Sypro Orange 5X) with small molecule (20 µM ABT-737) or vehicle (0.05% DMSO) and then subjected to a temperature gradient (0.01 °C/s) from 25 to 95 °C. Data were continuously acquired at ~465 nm (excitation) and ~580 nm (emission). Data was processed to generate first derivative curves where the curve maximum was reported as the melting temperature of the protein.

Vector generation for cellular assays. Fab AZ1 was converted into a previously described single-chain Fab construct using Gibson cloning.[58]

A gene encoding the Conventional CAR construct (CD8 Signal Sequence-Myc Tag-αCD19scFv-CD8 Hinge Domain-CD8 Transmembrane Domain-4IBB Co-stimulatory Region-CD3ζ Domain) was purchased as a gBlock™ (IDT). The gene was amplified by PCR and cloned into the pLX302 vector (Addgene plasmid #25896) using Gibson cloning. The sequence of the final construct was confirmed by sequencing of the entire gene. The AbCID CAR construct was generated by replacing the αCD19scFv portion of the Conventional CAR vector with the BCL-xL gene (residues 2–215) by Gibson cloning, followed by conversion of BCL-xL to BCL-xL(M159P) by site directed mutagenesis. The

M159P mutation has previously been shown to prevent BCL-xL from forming a domain-swapped dimer.[59] We feared that the two-dimensional confinement of the AbCID CAR on the cell membrane would promote dimer formation in BCL-xL(WT), and lead to antigen-independent activation of the CAR T-cells. The M159P mutation did not affect ABT-737 or AZ1 binding (data not shown). The sequence of the final construct was confirmed by sequencing of the entire gene.

The gene for CD19 was obtained from the ORFeome[60] and fused to a P2A-mCherry gene by overlap extension PCR. The gene was cloned into the pLX302 vector using Gibson cloning. The sequence of the final construct was confirmed by sequencing of the entire gene.

Culturing of cell lines. The NFAT reporter Jurkat cells utilized were a generous gift from Arthur Weiss. The K562 and HEK293T cells utilized were from frozen stocks maintained by the Wells lab. The cell lines were not authenticated before use. No test for mycoplasma contamination was performed. Unless otherwise noted all Jurkat and K562 cells lines were cultured in RPMI supplemented with 10% FBS and 1X Pen/Strep. All Jurkat NFAT reporter cells were maintained in G418 (2 mg/mL). All CAR containing Jurkat cell lines were maintained in puromycin (2 µg/mL) in addition to G418. $CD19^{+}$ K562 cells were maintained in puromycin (2 µg/mL). HEK293T cells containing the *Gal4-UAS-Fluc* operon were maintained in High Glucose DMEM supplemented with 10% FBS, 1X Pen/Strep, and puromycin (2 µg/mL). All cell lines were cultured at 37 °C under 5% CO_2.

Immunoblotting. HEK293T cells were plated at approximately 0.5×10^6 cells/well in a 6-well plate and cultured overnight at 37 °C under 5% CO_2 before transfection. The cells were transfected with a plasmid encoding scAZ1-avitag using TransIT-293 (Mirus Bio) following the manufacturer's procedure. The cells were further incubated at 37 °C for 48 h. The cells were washed with PBS and lysed with M-PER mammalian protein extraction reagent (Thermo Scientific) supplemented with Complete™ protease inhibitor cocktail (Roche) at 4 °C for 10 minutes. Immunoblotting was performed using an anti-AviTag antibody (GenScript mouse mAb, A01738).

CRISPRa-mediated luciferase assay. For CRISPRa-mediated transcriptional activation, the reporter HEK293T cell line containing the *Gal4-UAS-Fluc* operon[61] was seeded at ~0.5×10^6 cells/well in 6-well plates and cultured under 5% CO_2 at 37 °C overnight. The cells were transfected with a plasmid encoding scAZ1-VPR and another plasmid encoding dCas9-BCL-xL and Gal4 sgRNA at a 1:1 ratio. The transfected cells were trypsinized and resuspended in fresh DMEM supplemented with 10% FBS 24 h after transfection. Cells were then aliquoted into a 96-well poly-D-lysine coated plate (Corning) and allowed to adhere for 24 h before 20 nM ABT-737 was added to induce CRISPRa activity. Cells were then further incubated for 48 h before evaluation of luciferase gene expression. To determine luciferase activity, cells were lysed with Bright-Glo Luciferase Assay substrate (Promega) and analyzed using an Infinite M200 PRO plate reader (Tecan). The luciferase activities were background-subtracted with a negative control (cells expressing full-length dCas9-VPR and PHOX2B negative-sgRNA), and normalized against a positive control (cells expressing full-length dCas9-VPR and Gal4 sgRNA). For

investigation of cellular dose response, different concentrations of ABT-737 (0.014 nM, 0.041 nM, 0.12 nM, 0.37 nM, 1.1 nM, 3.3 nM, 10 nM, 30 nM, 90 nM, 270 nM) were added to the cells after cells were transfected and aliquoted to a 96-well plate.

Amino Acid Sequence of scAZ1.

Light Chain:

MASDIQMTQSPSSLSASVGDRVTITCRASQSVSSAVAWYQQKPGKAPKLLIYSASSLY
SGVPSRFSGSRSGTDFTLTISSLQPEDFATYYCQQYYWGFPSLFTFGQGTKVEIKRTV
AAPSVFIFPPSDSQLKSGTASVVCLLNNFYPREAKVQWKVDNALQSGNSQESVTEQD
SKDSTYSLSSTLTLSKADYEKHKVYACEVTHQGLSSPVTKSFNRGEC

Linker:

GGSSGSGSGSTGTSSSGTGTSAGTTGTSASTSGSGSGGGGGSGGGGSAGGTATAG
ASSGS

Heavy Chain:

EVQLVESGGGLVQPGGSLRLSCAASGFNLSYSSMHWVRQAPGKGLEWVASISPYSS
YTSYADSVKGRFTISADTSKNTAYLQMNSLRAEDTAVYYCARGWVGMDYWGQGTLV
TVSSASTKGPSVFPLAPSSKSTSGGTAALGCLVKDYFPEPVTVSWNSGALTSGVHTFP
AVLQSSGLYSLSSVVTVPSSSLGTQTYICNVNHKPSNTKVDKKVEPKSCDKTHT

Expression of bispecific antibodies. Expi293 (Life Technologies) cells were transiently co-transfected with two pFUSE (InvivoGen) vectors harboring the AZ1 heavy chain and the AZ1 light chain genetically fused to the αCD19 scFv at a ratio of 1:1. The ExpiFectamine 293 transfection kit (Life Technologies) was used for transfections as per manufacturer's instructions. Cells were incubated for 7 days at 37 °C in a 5% CO_2

environment before the supernatants were harvested by centrifugation. Protein was purified by Protein A affinity chromatography and assessed for quality and integrity by SDS-PAGE (**Figure 2-21**).

Generation of cell lines. All CAR containing Jurkat cells and $CD19^+$ K562 cells used for the T-cell activation experiments were generated by lentiviral transduction. To produce virus, HEK293T cells were transfected with a mixture of second-generation lentiviral packaging plasmids at ~80% confluence. FuGene HD (Promega) was used for transfection of the plasmids using 3 µg DNA (1.35 µg pCMV delta8.91, 0.15 µg pMD2-G, 1.5 µg pLX302) and 7.5 µL of FuGene HD per well of a six-well plate. Media was changed to complete DMEM after 6 h of incubation with transfection mixture. The supernatant was harvested and cleared by passing through a 0.2 µm filter 72 h post transfection. Cleared supernatant was added to target Jurkat NFAT reporter cells and K562 cells (~1 million cells per mL) with 8 µg/mL polybrene and cells were centrifuged at 1000 g at 33 °C for 2 h. Cells were then incubated with viral supernatant mixture overnight before the media was changed to fresh complete RPMI. Cells were expanded for a minimum of 48 h before they were grown in drug selection media. Drug selection for stable cell lines was started by the addition of 2 µg/mL puromycin. Following at least 72 h of incubation in puromycin containing media, cells were analyzed by flow cytometry for expression of the CAR or CD19. High expressing populations of $CD19^+$ K562 cells were enriched by flow cytometry by gating for expression of an intracellular mCherry marker genetically linked to CD19 by a P2A sequence. Jurkat cells displaying high levels of CARs were enriched by flow cytometry by gating for Myc tag antibody staining using a Myc-Tag Mouse mAb Alexa

Fluor647 conjugate (Cell Signaling 2233S). All flow cytometry cell sorting was performed using an AriaII (BD Biosciences).

Quantification of CAR-T cell activation. Jurkat cells expressing CARs were mixed with antigen positive ($CD19^+$) or antigen negative ($CD19^-$) K562 target cells at a ratio of 1:2. Bispecifc antibody (AZ1-αCD19) or Fab (AZ1) and ABT-737 or DMSO was diluted in media and added to cell mixtures. After overnight incubation at 37 °C, cells were pelleted by centrifugation. NFAT-dependent GFP reporter expression was quantified by flow cytometry using a FACSCanto II (BD Biosciences). CD69 expression was quantified by immunofluorescence flow cytometry using a FACSCanto II (BD Biosciences) using an APC anti-human CD69 Antibody (Biolegend 310910) (**Figure 2-22**). IL-2 secretion was quantified by collection of supernatants and analysis by ELISA using the BD Human IL-2 ELISA set as per manufacturer's protocol. All flow cytometry data analysis was performed using FlowJo software and all plots were generated using Prism software (GraphPad).

Assaying cellular toxicity of ABT-737. WT Jurkat, AbCID CAR Jurkat, Conventional CAR Jurkat, WT K562, $CD19^+$ K562, and HEK293T cells were plated in 96-well plates at ~5000 cells per well. Each cell line was incubated with varying concentrations of ABT-737 (10 µM initial, 3-fold serial-dilutions, 8 times) or DMSO alone (0.1%). After 24 h, cell viability was measured using a CellTiter-Glo® Luminescent Cell Viability Assay (Promega) and the manufacturer's standard protocol. The percent viability relative to DMSO treatment was plotted and analyzed for each cell line using Prism software (GraphPad).

Statistical Analysis. Unless otherwise noted all error bars represent the mean of 3 independent experiments ± s.d. All IC_{50}/EC_{50} values reported were calculated from the mean of 3 independent experiments using 3-parameter nonlinear regression in Prism7 (GraphPad) ± s.e.m.

Data Availability. All data generated and analyzed during the study are included either in this article or the associated supplementary information. All data and research resources, including protocols and plasmids are available upon reasonable request. The data utilized to generate **Figure 2-2** is publicly available in the RCSB Protein Data Bank (http://www.rcsb.org/pdb/home/home.do).

Methods-only References

51. Seiler, C.Y. et al. DNASU plasmid and PSI:Biology-Materials repositories: resources to accelerate biological research. *Nucleic Acids Res.* **42**, D1253-1260 (2014).
52. Hornsby, M. et al. A High Through-put Platform for Recombinant Antibodies to Folded Proteins. *Mol. Cell. Proteomics* **14**, 2833-2847 (2015).
53. Koerber, J.T., Hornsby, M.J. & Wells, J.A. An improved single-chain Fab platform for efficient display and recombinant expression. *J. Mol. Biol.* **427**, 576-586 (2015).
54. Rajan, S. et al. Structural transition in Bcl-xL and its potential association with mitochondrial calcium ion transport. *Sci. Rep.* **5**, 10609 (2015).
55. Collaboration, O.R. The ORFeome Collaboration: a genome-scale human ORF-clone resource. *Nat. Methods* **13**, 191-192 (2016).
56. Gilbert, L.A. *et al.* CRISPR-mediated modular RNA-guided regulation of transcription in eukaryotes. *Cell* **154**, 442-451 (2013).

Competing Financial Interest

Z.B.H., A.J.M., J.A.W., and the University of California San Francisco have filed a patent application related to the technology described in this manuscript. The value of this patent application may be affected by publication of this manuscript.

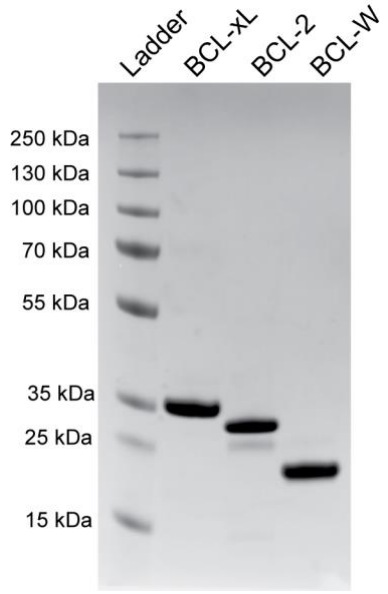

Figure 2-19. SDS-PAGE analysis of the BCL-2 family members expressed and utilized as part of this study. 3 µg of each protein was diluted into loading buffer with reducing agent (BME).

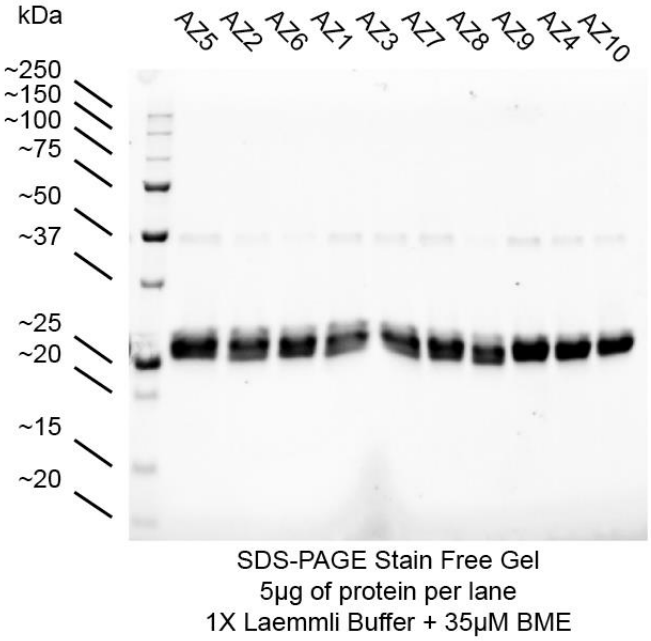

Figure 2-20. SDS-PAGE analysis of the Fabs expressed and utilized in this study. 5 µg each of Fabs AZ1–10 were diluted in loading buffer with reducing agent (BME). Individual bands corresponding to the light and heavy chains can be seen.

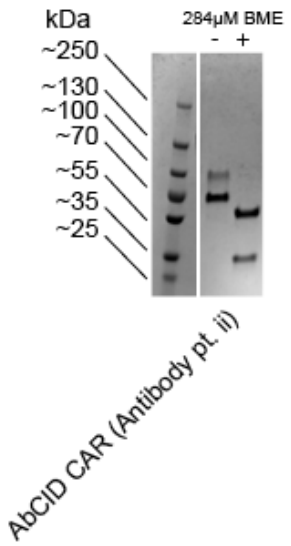

Figure 2-21. SDS-PAGE analysis of the bispecific antibody expressed and utilized in this study. The bispecific antibody AZ1-αCD19 was diluted in loading buffer in the presence or absence of reducing agent (BME). Individual bands corresponding to the light and heavy chain can be seen in the presence of reducing agent.

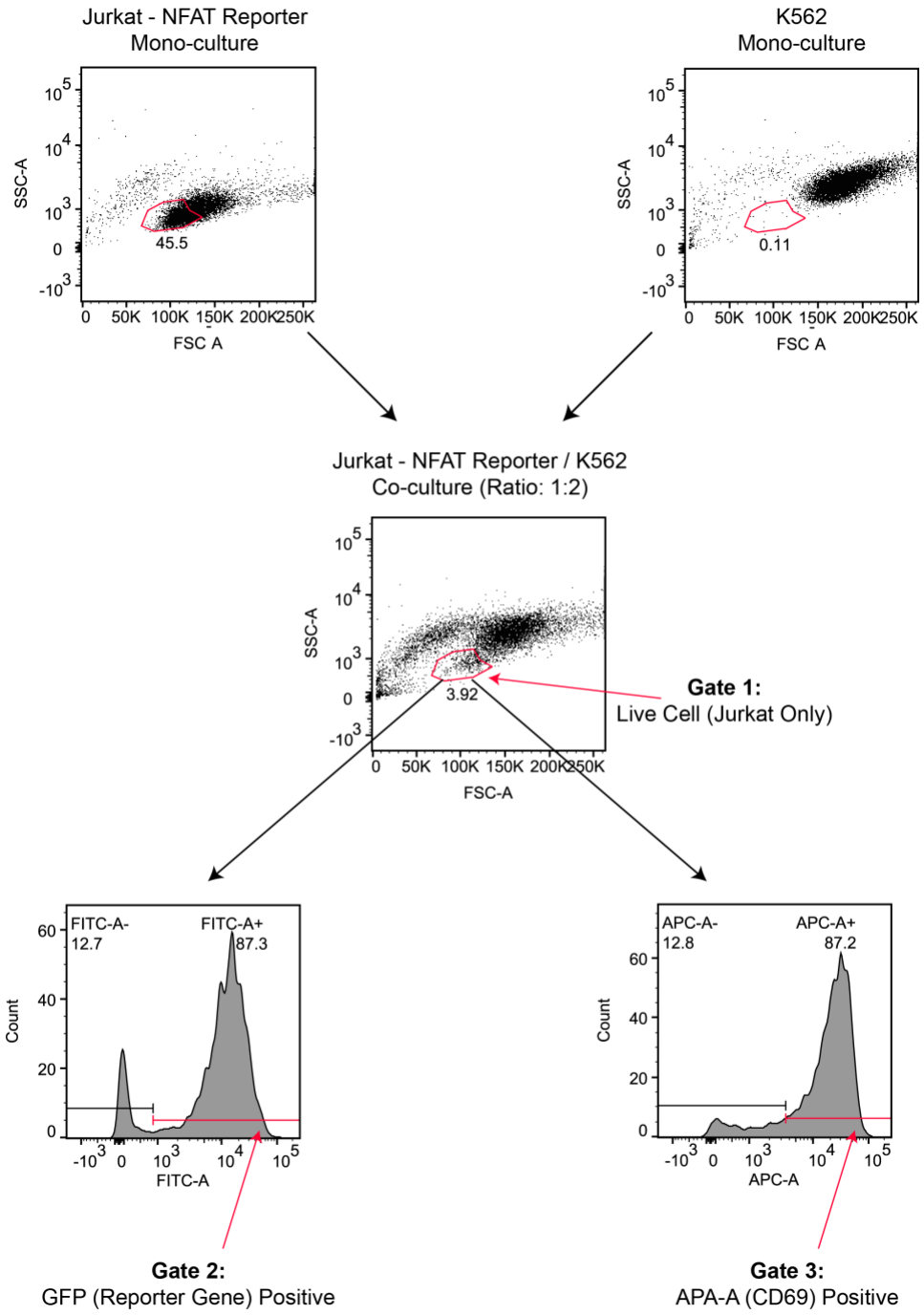

Figure 2-22. CAR T-cell activation assay gating scheme. Jurkat - NFAT Reporter cells and K562s were assessed in isolation (Top) to determine a Live Cell (Jurkat Only) gate. For co-culture experiments, live Jurkat cells were gated (Gate 1), and GFP (Gate 2) and CD69 staining (Gate 3) positive populations were quantified.

Publishing Agreement

It is the policy of the University to encourage the distribution of all theses, dissertations, and manuscripts. Copies of all UCSF theses, dissertations, and manuscripts will be routed to the library via the Graduate Division. The library will make all theses, dissertations, and manuscripts accessible to the public and will preserve these to the best of their abilities, in perpetuity.

Please sign the following statement:

I hereby grant permission to the Graduate Division of the University of California, San Francisco to release copies of my thesis, dissertation, or manuscript to the Campus Library to provide access and preservation, in whole or in part, in perpetuity.

Author Signature

07/30/18
Date